Short-distance correlation functions and non-perturbative renormalization of quark currents in lattice QCD

Masaaki TOMII

Doctor of Philosophy

Department of Particle and Nuclear Physics
School of High Energy Accelerator Science
SOKENDAI (The Graduate University for
Advanced Studies)

SOKENDAI
(The Graduate University for Advanced Studies)

Doctoral Thesis

Short-distance correlation functions and non-perturbative renormalization of quark currents in lattice QCD

Author:
Masaaki Tomii

Supervisor:
Prof. Shoji Hashimoto

A thesis submitted in fulfillment of the requirements
for the degree of Doctor of Philosophy

in the

School of High Energy Accelerator Science
Department or Particle and Nuclear Physics

Abstract

Short-distance correlation functions and non-perturbative renormalization of quark currents in lattice QCD

by Masaaki TOMII

Precise predictions of the Standard Model (SM) are important for the search of new physics. Precision of the SM predictions needs to be improved for comparisons with forthcoming experiments. Uncertainty of the SM predictions mainly arises from the contribution of Quantum Chromodynamics (QCD), which is the theory of strong interaction of quarks, anti-quarks and gluons. This is because QCD cannot be treated by perturbation theory at low energies and the parameters of QCD such as the strong coupling constant have large uncertainty compared to other SM parameters.

Correlation functions of quark currents provide a rich source of information on the QCD vacuum at various scales ranging from perturbative to non-perturbative regions. At short distances, they become mostly perturbative due to the asymptotic freedom of QCD. Using high order perturbation theory, they can be used to determine the strong coupling constant. At long distances, on the other hand, the correlation functions carry the information about hadron spectrum and the low energy constants of QCD, which are the parameters in the chiral perturbation theory.

Correlation functions can be calculated from first principles using lattice QCD. In lattice QCD, the spacetime is discretized and compactified with some boundary conditions. Then, the degrees of freedom of the system in lattice QCD become finite and numerical path integral is feasible using the Monte Carlo method. Taking the infinite volume limit and the continuum limit for the correlation functions on the lattice, one can obtain the correlation functions in the continuum.

Comparison of the correlation functions in the continuum theory and on the lattice may determine fundamental quantities of QCD. In fact, lattice QCD is usually applied to calculate hadron masses and decay constants from the correlation functions at long distances. Similarly, the comparison at short distances can in principle provide a determination of the strong coupling constant. The comparison at short distances needs to be performed after eliminating lattice artifacts. The lattice calculation at short distances suffers from unphysical discretization effect which becomes more significant as the distance becomes small. A careful investigation of the discretization effect is, therefore, necessary for the precise determination of the strong coupling constant.

In this thesis, we analyze short-distance correlation functions both on the lattice and in the continuum, and investigate the region where the lattice results agree with the continuum theory after removing the lattice artifact. The lattice simulation is carried out on 14 gauge field ensembles generated by the JLQCD collaboration. The ensembles contain $2+1$ flavors of sea quarks described by the Möbius domain-wall fermions, which realize precise chiral symmetry on the lattice. The pion masses on these ensembles are in the region 220–500 MeV. The lattice spacings are 0.044 fm, 0.055 fm, and 0.080 fm. We subtract the discretization effects within the mean field approximation. We extrapolate lattice results to the physical pion mass and the continuum limit.

Vector, axial-vector, scalar, pseudoscalar channels of the correlation functions in perturbation theory are available to the four-loop level. Using such well-advanced results, we investigate the convergence property of perturbative expansions. Slight deviation of the correlation functions at short distances from those in perturbation theory is explained by the Operator Product Expansion (OPE), which accommodates some non-perturbative effects in the correlation functions by expanding a product of operators into a series of composite operators.

We utilize the correspondence of continuum and lattice correlation functions for the renormalization of quark currents. It turns out that although the correlation functions on our lattice ensembles suffer from significant discretization effect in the perturbative region, the analysis including OPE allows us to determine the renormalization constants at slightly longer distances, where the discretization effects is well-managed. We obtain the renormalization constants of the vector current and the scalar density with the precision of $O(1\%)$ or less.

Using the result of the renormalization, we test the consistency between the correlation functions on the lattice and experiments. We calculate the vector and axial-vector correlation functions from the experimental results of spectral functions obtained through the hadronic tau decays by the ALEPH collaboration. We verify that the experimental correlation functions are in good agreement with our lattice results.

The result of the renormalization is also applied to an analysis of the chiral condensate, which is an order parameter of the spontaneous breaking of chiral symmetry in QCD and plays an important role in the chiral perturbation theory. We extract the chiral condensate from current correlators in the OPE regime. This result agrees with the world average of lattice calculation of $2+1$ flavors QCD.

Acknowledgements

First of all, I express my deep gratitude to Prof. Shoji Hashimoto, my supervisor, for his great advices, continuous regards, and many important discussions for three years even though he has been very busy with a hectic schedule. With out his supports, I could not have studied so far.

I also thank M. Hayakawa for teaching me a lot of important things as a researcher and showing me his attractive passion. I appreciate H. Matsufuru and T. Kaneko's effort to secure large disk storages `/xwork**` and to create my account on the workstations `scdl360d.kek.jp` and `scbc2fe.kek.jp`. This study is done in the JLQCD collaboration. I thank H. Fukaya, J. Noaki, G. Cossu, B. Fahy, and all other JLQCD members for many discussion, comments, and teachings. I could have discussions with other professional researchers, F. Knechtli, P. Boyle, T. Izubuchi, C. Lehner, and H. Ohki, and many researchers in KEK. I thank all of these people.

My research activity is successful in virtue of several supportive programs and related peole. My trips to JPS meetings, lattice conferences and other workshops are aided by the Student Travel Reimbursement program managed by SOKENDAI and SH's grant, the Grant-in-Aid of the Japanese of Educations No. 26247043. The trip to BNL is aided by The Short-Stay Abroad Program managed by SOKENDAI. I thank M. Oishi, a secretary of the lattice group in KEK Theory Center, and members of Postgraduate Education Unit in KEK for their help with the procedures for these trips. I was employed by KEK as a research assistant (RA). Numerical simulations are carried out on Hitachi SR 16000 and IBM System Blue Gene/Q (BGQ) at KEK under a support of its Large Scale Simulation Program (Nos. 13/14-04,14/15-10). The JLQCD collaboration thanks PB for the optimized code for BGQ.

Finally, I am grateful to my family for continuous encouragement and supports.

Masaaki Tomii

Contents

List of Figures

List of Tables

Chapter 1

Introduction

The Standard Model (SM) of elementary particles forms the basis for the progress in high energy physics. It describes the fundamental particles and their interactions. The formulation of the SM is completed in the 1970s and its validity has been supported by a lot of experiments. At the same time, several experiments have shown small but significant deviations from the SM, which can be understood as signs of new physics beyond the SM. Since these signs must play a key role in the progress in high energy physics, many high energy physicists concentrate their effort on testing the SM.

Recent activities of experimentalists aim at the SM tests by a drastic improvement in the precision in the next decade. For example, Belle II experiment is going to quantify the effects of CP violation focusing on the decay processes of B mesons. The groups at J-PARC and Fermilab are going to measure the muon anomalous magnetic moment, which may show a sign of new physics, with the precision five times better than the previous experiment at BNL. These experiments are expected to produce results in early 2020s.

On the theory side, researchers are trying to provide SM predictions with the precision which competes with that of the forthcoming experiments. As well known, precise calculations of the contribution of Quantum Chromodynamics (QCD) is the most difficult part in such efforts. The crucial origin of this difficulty is the spontaneous breaking of chiral symmetry in the QCD vacuum. At low energies ($\lesssim 1$ GeV), perturbation theory is no longer valid and there are a lot of unpredictable effects such as instanton interactions. At high energies ($\gg 1$ GeV), where perturbation theory is applicable, precise calculation of the QCD contribution is still difficult because the uncertainty of the strong coupling constant ($\sim 0.5\%$) is quite larger than that of other SM parameters such as the fine structure constant ($\sim 2 \times 10^{-8}\%$). Therefore the understanding of the vacuum structure and a precise determination of the strong coupling constant are important to achieve precise predictions of the SM.

Correlation functions of quark currents, or briefly current correlators, are useful tools to study these topics. They are defined as vacuum expectation values of a product of quark currents placed at different positions. Figure 1.1 shows a sketch of current correlators with main particles which are related to them. Bullets correspond to the quark currents, which is connected with the black solid lines standing for valence quarks which are interacting with gluons

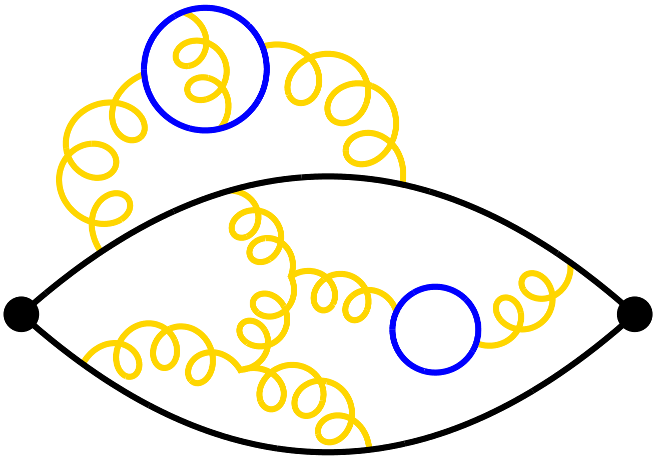

FIGURE 1.1: A sketch of current correlators. Bullets, black solid lines, blue loops and curly lines correspond to quark currents, valence quarks, sea quarks and gluons, respectively.

shown by curly lines. Gluons interact with themselves and with sea quarks as shown by blue loops as well as with valence quarks. In addition to these particles, the photon and leptons are introduced if one takes into account the electromagnetic corrections. There are a number of channels of correlators, which represent the quantum numbers of the corresponding quark currents. Scalar, pseudoscalar, vector and axial-vector channels are widely studied as the simplest cases. An extensive review of correlators was given by Shuryak [1].

Current correlators reflect the property of QCD at any scale region from low-energy to high-energy. At short distances (< 0.1 fm), or equivalently at large external momenta, correlators are mostly perturbative and therefore can be used to determine the strong coupling constant. In this region, the effect of the spontaneous chiral symmetry breaking is negligible and therefore some degeneracies of correlators, such as the vector and axial-vector ones, are realized. On the other hand, correlators at sufficiently long distances (> 1 fm) or small momenta are well described by chiral perturbation theory and carry the information about the low energy constants and the hadron spectroscopy, reflecting the characteristics of the corresponding channels.

Correlators at the middle distances are more complicated. From the viewpoint of perturbation theory, the strong coupling constant blows up and the effect of the spontaneous chiral symmetry breaking contributes significantly as the distance of correlators approaches the typical scale $\Lambda_{\mathrm{QCD}}^{-1}$ of QCD. From the viewpoint of the hadronic picture, on the other hand, correlators at the middle involve the effects of many excited states. Thus, current correlators may allow us to investigate such non-perturbative properties of QCD as well as the fundamental parameters such as the strong coupling constant and the low-energy constants.

An attempt to understand current correlators at longer distances beyond perturbation theory is based on the Operator Product Expansion (OPE), which was firstly introduced by Wilson [2, 3] and well formulated by Shifman-Vainstein-Zakharov [4–6] for QCD. OPE accommodates some non-perturbative effects by expanding a product of operators into a series of composite operators. Wilson coefficients of OPE, which are the coefficients of the composite operators in the series, are usually calculated perturbatively as a series of the strong coupling constant.

Although OPE is widely used to investigate QCD, it was suggested [7] that OPE does not work well in some cases. For example, the correlator of the scalar or pseudoscalar channel considerably deviates from the prediction of OPE. This fact was verified by phenomenological test [1] and lattice calculations [8, 9]. These disagreements are qualitatively understood as the effects of the instanton-induced 't Hooft interactions [10]. Although some models have been proposed for the quantitative understandings of the inconsistencies [11, 12], no definite explanation based on the first principle of QCD has been obtained.

There is another approach to understand current correlators in the non-perturbative regime. The non-perturbative property of current correlators is encoded in the spectral functions, which are obtained from e^+e^- hadronic annihilations or hadronic decays of the τ lepton. The experimental data of the hadronic τ decays by the ALEPH collaboration [13] were used to obtain the correlators [14]. Indeed the sum rule approach is widely used for the determination of the strong coupling constant [13, 15–19], the gluon condensate [19, 20], and so on.

The sum rule approach is limited because the experimental data of spectral functions are measured for a limited region of the invariant mass, which is below the mass of the τ lepton for the experiment of hadronic τ decays. In the region without experimental data, the spectral function used to be calculated by using perturbation theory or OPE until the violation of the quark-hadron duality was suggested [21–24]. The essence of the duality violation is that a spectral function calculated perturbatively (or using OPE) may and actually does disagree with experimentally measured one beyond the uncertainty caused by truncations of perturbative expansion (and OPE) in the Minkowski space. After the suggestion of the duality violation, the treatment of the spectral function in the region where experimental data are not available was shifted from perturbative methods to model-based ones [23–30]. Since such analyses are based on models, more reliable treatment of the spectral function such as lattice QCD is desired.

The seminal work on the investigation of current correlators by lattice simulations was done [31] by using a quenched simulation with Wilson fermions for valence quarks. They showed an agreement between the lattice results and the phenomenological analyses with experimental data. Another group [32] performed a similar analysis and their results are roughly consistent with [31]. Several years later, a quenched simulation with the overlap valence quarks was performed for the calculation of correlators [8, 9]. In virtue of the exact chiral symmetry of overlap fermions, they were able to investigate some combinations of correlators of two channels, *e.g.* the average $V + A$ or the difference $V - A$ of the vector and axial-vector channels. The former channel $V + A$ is free from the effect of the spontaneous chiral symmetry breaking, while the latter $V - A$ reflects the effect of it. Their lattice result of the $V - A$ channel agreed with the sum rule approach [14] from the hadronic τ decays, while the $V + A$ channel did not agree well. Several years later, the strong coupling constant was determined using the vector and axial-vector correlator in the momentum space calculated with dynamical overlap fermions [33, 34]. These previous works are all with one finite lattice spacing and no one has taken the continuum limit.

These comparisons of lattice results and phenomenological ones are achieved by matching the renormalization schemes and scales. In general, renormalization of lattice operators is a necessary step for the lattice QCD calculations of scheme dependent quantities such as the matrix elements of the weak scattering and decay processes. Current correlators themselves are applicable to renormalization of quark currents. This renormalization procedure was proposed by [35] and applied to a quenched simulation [36] and a dynamical simulation [37]. Since the conventional scheme of a quantity is usually the $\overline{\text{MS}}$ scheme, the renormalization need perturbative calculations. The perturbative calculations of the (pseudo)scalar and (axial-)vector correlators are nowadays available up to the four-loop calculation [38] except for the quark mass corrections and therefore renormalization to the $\overline{\text{MS}}$ scheme by this method can minimize the uncertainty of perturbative calculations.

In this thesis, we investigate the possibility that current correlators play an important role in understandings of QCD. For example, lattice calculation of current correlators may provide important quantities of QCD such as the strong coupling constant. The determinations, which are achieved by comparing the lattice result with the continuum calculation, need a region of x in which the correlators on the lattice and in the continuum are both precisely calculated. For the determination of the strong coupling constant, for example, the discretization effects on the correlators in the region where the perturbative calculation or the OPE is sufficiently precise need to be under controlled. Therefore, we investigate the presence of the window where both the lattice and continuum calculations are applicable without large uncertainty. The analyses for the following topics are all aimed at this purposes.

At first, we renormalize the quark currents based on the method using the current correlators [35–37]. In this method, the renormalization window, which is the region of x where both the lattice and perturbative calculations are reliable, is needed for a precise renormalization. With careful investigations and managements of discretization effects on the lattice and the convergence of the perturbative calculations, the window is produced and the renormalization factors are determined with the competing precision ($\lesssim 1\%$) with results from other renormalization methods.

Next, we use the results of the renormalization to compare the lattice result of the current correlators with the phenomenological correlators converted from the latest ALEPH spectral functions [39]. In the calculation of the experimental correlators, we adopt some assumptions to evaluate the spectral function above the mass of the τ lepton, where the experimental data do not exist. We find a good agreement between the lattice calculation and the experiments.

The result of the renormalization is also applied to an analysis of the chiral condensate, which is an order parameter of the spontaneous breaking of chiral symmetry in QCD and plays an important role in chiral perturbation theory. We extract the chiral condensate from the longitudinal component of the axial-vector current correlator. This analysis needs the off-diagonal components of the axial-vector correlator with respect to the Lorentz indices, whose lattice investigation is done for the first time by this work.

The numerical simulation is carried out on the gauge ensembles with $2+1$-flavor dynamical Möbius domain-wall fermions [40, 41] generated by the JLQCD collaboration [42]. Möbius domain-wall fermion, which is an improved implementation of the domain-wall fermion [43, 44], has precise chiral symmetry on the lattice. The chiral symmetry on the lattice is defined by the Ginsparg-Wilson relation [45] and the magnitude of its violation is quantified by the residual mass, which is at the order of 1 MeV or less on our ensembles. The lattice spacings are 0.0439 fm, 0.0547 fm, and 0.0804 fm. The pion masses are in the region 220–500 MeV.

This thesis is organized as follows. In Chapter 2, we give the definitions and summarize the topics of correlation functions in the continuum theory, which are the bases of this study. In Chapter 3, we take account of several lattice artifacts appearing in the correlators. In Chapter 4, we show the results of the renormalization of the vector current and scalar density. In Chapter 5, we discuss the consistency between the lattice calculation and the phenomenological approach and calculate the chiral condensate.

Chapter 2

Correlation functions in QCD vacuum

2.1 Correlation functions in coordinate space

In this work, we investigate the four channels of point-to-point correlation functions, which are defined as the vacuum expectation value of the product of a couple of the corresponding quark currents with finite separation x,

$$\begin{aligned} \Pi_S(x) &= \langle S(x)S(0)^\dagger\rangle, & \Pi_P(x) &= \langle P(x)P(0)^\dagger\rangle, \\ \Pi_{V,\mu\nu}(x) &= \langle V_\mu(x)V_\nu(0)^\dagger\rangle, & \Pi_{A,\mu\nu}(x) &= \langle A_\mu(x)A_\nu(0)^\dagger\rangle, \end{aligned} \tag{2.1}$$

where each operator is defined by

$$\begin{aligned} S(x) &= \bar{u}d(x), & P(x) &= \bar{u}\mathrm{i}\gamma_5 d(x), \\ V_\mu(x) &= \bar{u}\gamma_\mu d(x), & A_\mu(x) &= \bar{u}\gamma_\mu\gamma_5 d(x). \end{aligned} \tag{2.2}$$

Here, the source point is fixed to zero with the assumption of translational invariance. The correlation functions are usually called by a brief name, the correlators.

These correlators are in the four dimensional Euclidean space, *i.e.* points are separated in the space-like direction. The Euclidean correlators are related to the Minkowski ones by the analytic continuation. The Euclidean correlators dump exponentially at long distances unlike those in the Minkowski space, which show the oscillatory behavior. In the Euclidean space, the time-ordered product for two operators at 0 and x is not needed. The connection of the field theory in the Euclidean and Minkowski spaces is reviewed in Appendix A.

The Study of the correlators in the coordinate space rather than in the momentum space is convenient because those in the coordinate space contain the unphysical contact term only at $x = 0$ as $\propto \delta(x)$, while contact terms in the momentum are proportional to $\propto 1, q^2, q^4 \ldots$. Since we do not use the correlator at $x = 0$, we omit this contact term.

For the vector and axial-vector channels, we analyze not only the Lorentz diagonal components but also the off-diagonal ones, which had never been investigated by lattice simulations so far. A combination of the diagonal and off-diagonal parts may provide an important quantity. As an example, we try to extract the chiral condensate through the axial Ward-Takahashi identity (see Sections 2.4, 5.2).

If one focuses on the diagonal components, the trace

$$\Pi_{V/A}(x) = \sum_\mu \Pi_{V/A,\mu\mu}(x) \tag{2.3}$$

is usually employed. This quantity is Lorentz scalar and its treatment is simple. We call the trace the scalar-contracted (axial-)vector correlator or simply the (axial-)vector correlator.

2.2 Massless perturbation theory

In this section, we discuss the convergence of the perturbative expansion of the massless correlators. Since the scalar and pseudoscalar correlators, as well as the vector and axial-vector correlators, degenerate in the massless perturbation theory, *i.e.* $\Pi_S = \Pi_P$ and $\Pi_V = \Pi_A$, we consider only the two channels Π_S and Π_V.

The perturbative expansion of the vector correlator is written as

$$\Pi_V^{\overline{\mathrm{MS}}}(x) = \frac{6}{\pi^4 x^6}\left(1 + \sum_{i=1}^{\infty} C_i^V a_s(\mu_x)^i\right), \tag{2.4}$$

with perturbative coefficients C_i^V. Here, $a_s(\mu_x) = \alpha_s(\mu_x)/\pi$ is the strong coupling constant and its scale μ_x is set as

$$\mu_x = \frac{1}{|x|}. \tag{2.5}$$

One can reorganize the perturbative series using the renormalization group to another scale μ_x^*, *i.e.*

$$\Pi_V^{\overline{\mathrm{MS}}}(x) = \frac{6}{\pi^4 x^6}\left(1 + \sum_{i=1}^{\infty} C_i^V(\mu_x^*) a_s(\mu_x^*)^i\right), \tag{2.6}$$

which is exact when the perturbative series includes all orders, provided that the coefficients $C_i^V(\mu_x^*)$ are converted appropriately. The conversion formula of the coupling constants is available to four-loop level [46].

Chetyrkin and Maier [38] wrote the perturbative coefficients up to $O(a_s^4)$ at the renormalization scale μ_x in the $\widetilde{\mathrm{MS}}$ scheme, which is the same as the $\overline{\mathrm{MS}}$ scheme at a scale $2\mathrm{e}^{-\gamma_E}\mu_x \simeq 1.123/|x|$. Here, $\gamma_E \simeq 0.5772$ is Euler's constant. In our notation, these coefficients correspond to $C_i^V(2\mathrm{e}^{-\gamma_E}\mu_x)$.

Since the perturbative expansion truncated at a finite order may depend on μ_x^*, there is an optimal choice for the scale that leads to the best convergence. One possible recipe to choose the optimal scale μ_x^* is the Brodsky-Lepage-Mackenzie (BLM) approach [47], which is motivated by an idea of absorbing the higher order contributions of gluon vacuum polarization into the coupling constant. The scale is chosen such that the perturbative coefficient at a_s^2 becomes independent of the number of flavors n_f. This BLM scale μ_x^{BLM} of the vector correlator thus determined is[1]

$$\mu_x^{\mathrm{BLM}} = 2\exp\left[\frac{1}{2}(4\zeta_3 - 3 - 2\gamma_E)\right]\mu_x \simeq \frac{2.7733}{|x|}, \tag{2.7}$$

where $\zeta_3 \simeq 1.202$ is the Riemann zeta function at the argument 3.

Using the result of [38] and [46], we obtain the perturbative coefficients $C_i^V(\mu_x)$, $C_i^V(2\mathrm{e}^{-\gamma_E}\mu_x)$, and $C_i^V(\mu_x^{\mathrm{BLM}})$ as

$$\begin{aligned} C_1^V(\mu_x) &= 1, \\ C_2^V(\mu_x) &= -5.5269 + 0.34002 n_f, \\ C_3^V(\mu_x) &= 10.415 - 3.2912 n_f + 0.12602 n_f^2, \\ C_4^V(\mu_x) &= 28.928 + 30.966 n_f - 2.6652 n_f^2 + 0.064007 n_f^3, \end{aligned} \tag{2.8}$$

$$\begin{aligned} C_1^V(2\mathrm{e}^{-\gamma_E}\mu_x) &= 1, \\ C_2^V(2\mathrm{e}^{-\gamma_E}\mu_x) &= -4.8893 + 0.30137 n_f, \\ C_3^V(2\mathrm{e}^{-\gamma_E}\mu_x) &= 5.2517 - 2.6633 n_f + 0.10124 n_f^2, \\ C_4^V(2\mathrm{e}^{-\gamma_E}\mu_x) &= 33.562 + 26.233 n_f - 2.2001 n_f^2 + 0.050863 n_f^3, \end{aligned} \tag{2.9}$$

$$\begin{aligned} C_1^V(\mu_x^{\mathrm{BLM}}) &= 1, \\ C_2^V(\mu_x^{\mathrm{BLM}}) &= 0.083333, \\ C_3^V(\mu_x^{\mathrm{BLM}}) &= -7.1191 - 1.1478 n_f + 0.010414 n_f^2, \\ C_4^V(\mu_x^{\mathrm{BLM}}) &= -56.886 + 12.283 n_f - 0.58326 n_f^2 + 0.014075 n_f^3. \end{aligned} \tag{2.10}$$

For $n_f = 3$, the corresponding perturbative expansion becomes

$$\begin{aligned} \Pi_V^{\overline{\mathrm{MS}}}(x)\Big|_{n_f=3} = \frac{6}{\pi^4 x^6}\Big(&1 + a_s(\mu_x) - 4.5069 a_s(\mu_x)^2 \\ &+ 1.6758 a_s(\mu_x)^3 + 99.567 a_s(\mu_x)^4 + O(a_s^5)\Big), \end{aligned} \tag{2.11}$$

$$\begin{aligned} \Pi_V^{\overline{\mathrm{MS}}}(x)\Big|_{n_f=3} = \frac{6}{\pi^4 x^6}\Big(&1 + a_s(2\mathrm{e}^{-\gamma_E}\mu_x) - 3.9852 a_s(2\mathrm{e}^{-\gamma_E}\mu_x)^2 \\ &-1.8270 a_s(2\mathrm{e}^{-\gamma_E}\mu_x)^3 + 93.835 a_s(2\mathrm{e}^{-\gamma_E}\mu_x)^4 + O(a_s^5)\Big), \end{aligned} \tag{2.12}$$

---

[1] To be more precise, the BLM scale (2.7) eliminates the n_f-dependence on the perturbative coefficient at two-loop. In fact, the coefficients at three- and four-loop levels in (2.10) depend on n_f. Although generalization of the BLM scale setting to any finite order expansions are investigated [48–50], we do not apply it because we vary the scale μ_x^* for the error estimation as discussed below.

$$\Pi_V^{\overline{\mathrm{MS}}}(x)\Big|_{n_f=3} = \frac{6}{\pi^4 x^6}\Big(1+a_s(\mu_x^{\mathrm{BLM}}) + 0.083333a_s(\mu_x^{\mathrm{BLM}})^2 \\ -10.469a_s(\mu_x^{\mathrm{BLM}})^3 - 24.907a_s(\mu_x^{\mathrm{BLM}})^4 + O(a_s^5)\Big). \tag{2.13}$$

Figure 2.1 shows the vector correlator calculated with (2.11). It is normalized by the tree-level correlator $\Pi_V^{\mathrm{free}}(x) = 6/\pi^4 x^6$. A reasonable convergence is observed only below $|x| \sim 0.15$ fm, which is not so large compared to our lattice spacings $a = 0.044$–0.080 fm. It implies that there is no renormalization window satisfying the condition that the perturbative calculation is convergent and the discretization effects are sufficiently small. The result of the perturbative series (2.12) is similar to that of (2.11). On the other hand, the result of (2.13) shows much better convergence as plotted in Fig. 2.2, implying that the convergence of the perturbative series is actually improved by tuning the renormalization scale μ_x^*.

In order to choose the optimal scale and estimate the uncertainty of the higher order corrections, we investigate the μ_x^*-dependence of the perturbative calculation. The μ_x^*-dependence of the vector correlator is shown in Fig. 2.3 for several distances in the range 0.2–0.5 fm. Since the all-order calculation has to be independent of μ_x^*, we determine the optimal scale $\mu_x^{*,\mathrm{opt}}$ as the value which minimizes the μ_x^*-derivative of the four-loop correlator,

$$\mu_x^{*,\mathrm{opt}} = \mathrm{e}^{1.7}\mu_x \simeq \frac{5.5}{|x|}. \tag{2.14}$$

The uncertainty of the higher order corrections to the vector correlator is estimated by varying μ_x^* in the region $[\frac{1}{2}\mu_x^{*,\mathrm{opt}}, 2\mu_x^{*,\mathrm{opt}}]$, which is shown in Fig. 2.3 by the gray band.

The expansion at the scale $\mu_x^{*,\mathrm{opt}}$ reads

$$\Pi_V^{\overline{\mathrm{MS}}}(x)\Big|_{n_f=3} = \frac{6}{\pi^4 x^6}\Big(1 + a_s(\mu_x^{*,\mathrm{opt}}) + 3.1431a_s(\mu_x^{*,\mathrm{opt}})^2 \\ + 4.8432a_s(\mu_x^{*,\mathrm{opt}})^3 - 33.819a_s(\mu_x^{*,\mathrm{opt}})^4 + O(a_s^5)\Big). \tag{2.15}$$

As shown in Fig. 2.4, the choice of $\mu_x^{*,\mathrm{opt}}$ shows better convergence. The gray region in the figure represents the higher order uncertainty, which is estimated by the maximum difference between the correlator at $\mu_x^* = \mu_x^{*,\mathrm{opt}}$ and those at μ_x^* in $[\frac{1}{2}\mu_x^{*,\mathrm{opt}}, 2\mu_x^{*,\mathrm{opt}}]$.

Next, we consider the scalar correlator. The scalar channel is more complicated due to the scale dependence of the scalar operator $S(x)$. We start from the perturbative series

$$\Pi_S^{\overline{\mathrm{MS}}}(\mu_x; x) = \frac{3}{\pi^4 x^6}\left(1 + \sum_{i=1}^{\infty} C_i^S a_s(\mu_x)^i\right). \tag{2.16}$$

Here, both the scales of the operator itself and the coupling constant are set to $\mu_x = 1/|x|$, which eliminates the logarithmic terms from the expression. Using the beta function [46] and

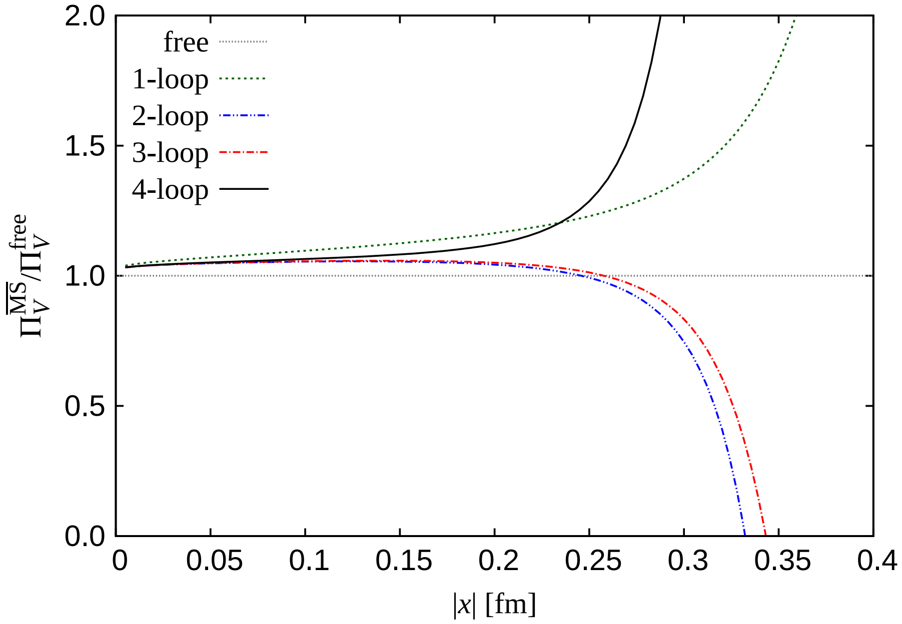

FIGURE 2.1: Perturbative expansion of the vector correlator renormalized in the $\overline{\mathrm{MS}}$ scheme with $n_f = 3$. The results of (2.11) truncated at a_s^0 (fine-dotted), a_s (dotted), a_s^2 (dashed double-dotted), a_s^3 (dashed dotted), and a_s^4 (solid) are plotted as functions of $|x|$.

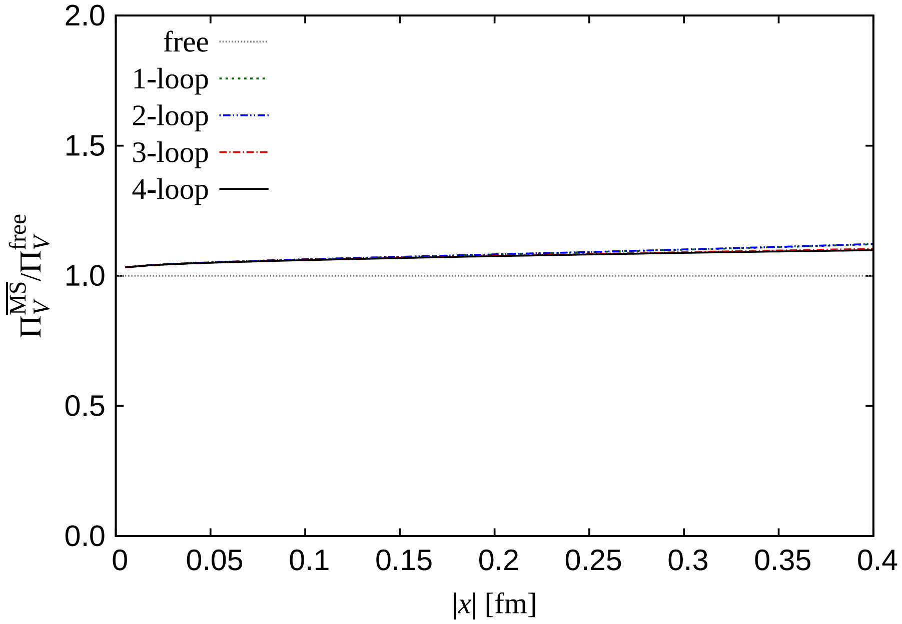

FIGURE 2.2: Perturbative expansion of the vector correlator renormalized in the $\overline{\mathrm{MS}}$ scheme with $n_f = 3$. The results of the perturbative series (2.13) at the BLM scale truncated at a_s^0 (fine-dotted), a_s (dotted), a_s^2 (dashed double-dotted), a_s^3 (dashed dotted), and a_s^4 (solid) are plotted as functions of $|x|$.

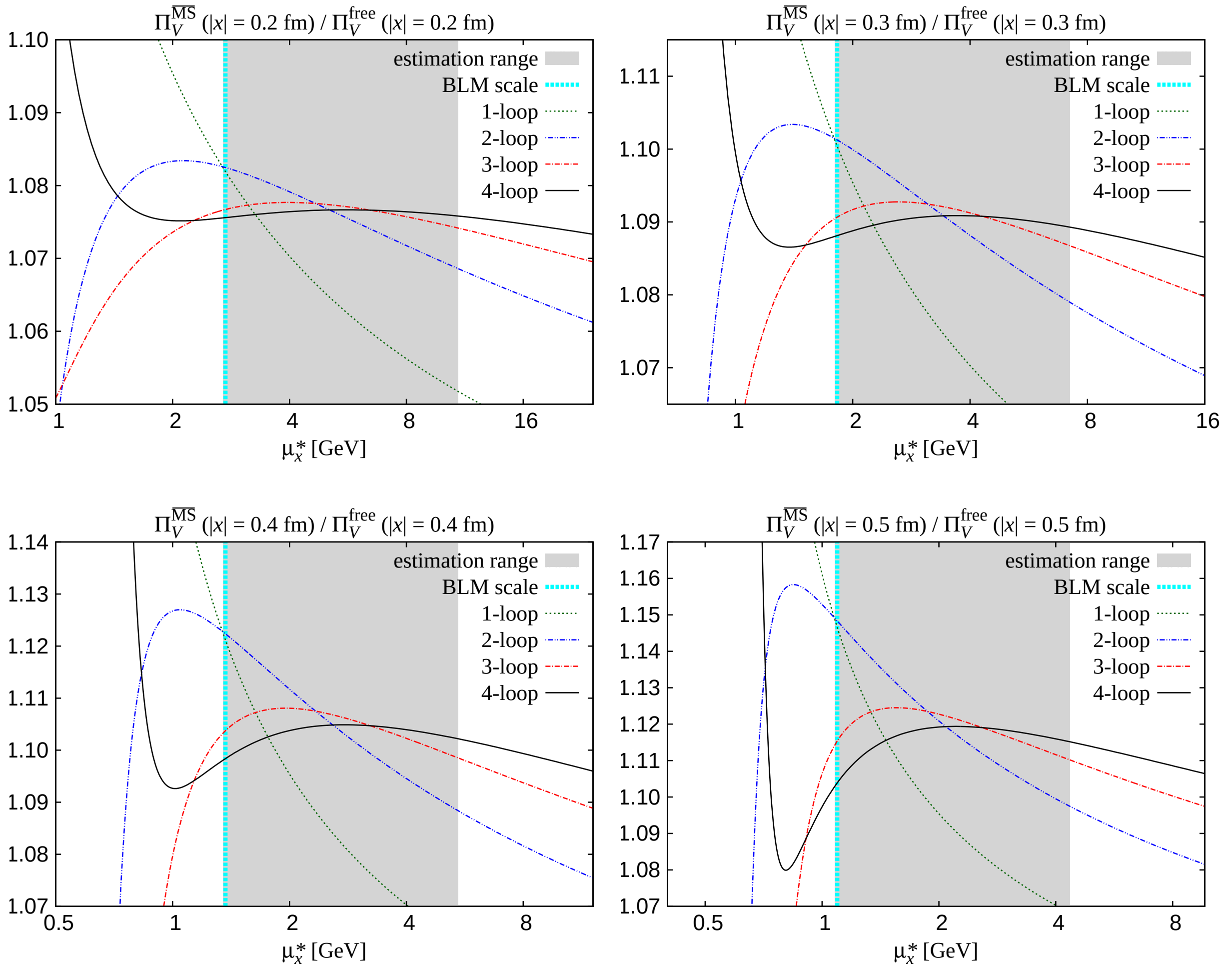

$\Pi_V^{\overline{\mathrm{MS}}}$ (|x| = 0.2 fm) / Π_V^{free} (|x| = 0.2 fm)

$\Pi_V^{\overline{\mathrm{MS}}}$ (|x| = 0.3 fm) / Π_V^{free} (|x| = 0.3 fm)

$\Pi_V^{\overline{\mathrm{MS}}}$ (|x| = 0.4 fm) / Π_V^{free} (|x| = 0.4 fm)

$\Pi_V^{\overline{\mathrm{MS}}}$ (|x| = 0.5 fm) / Π_V^{free} (|x| = 0.5 fm)

FIGURE 2.3: Vector correlator renormalized in the $\overline{\mathrm{MS}}$ scheme at the specific distances 0.2 fm (top/left), 0.3 fm (top/right), 0.4 fm (bottom/left), and 0.5 fm (bottom/right) as functions of μ_x^*. The results truncated at a_s (dotted), a_s^2 (dashed double-dotted), a_s^3 (dashed dotted), and a_s^4 (solid) are plotted. The gray band represents the region in which we estimate the uncertainty of the higher order corrections. The vertical bold line near the lower end of the gray band stands for the BLM scale (2.7).

the anomalous dimension [51, 52], one can also write a more general expression

$$\Pi_S^{\overline{\mathrm{MS}}}(\mu_x'; x) = \frac{3}{\pi^4 x^6}\left(1 + \sum_{i=1}^{\infty} C_i^S(\mu_x^*, \mu_x') a_s(\mu_x^*)^i\right), \tag{2.17}$$

where the first argument μ_x^* of the perturbative coefficients is the renormalization scale of the strong coupling constant in the perturbative series and the second μ_x' is the renormalization scale of the scalar operator.

Chetyrkin and Maier [38] gave the perturbative coefficients of correlators at the renormalization scale $\mu_x^* = \mu_x' = 2\mathrm{e}^{-\gamma_E}\mu_x$, which is $C_i^S(2\mathrm{e}^{-\gamma_E}\mu_x, 2\mathrm{e}^{-\gamma_E}\mu_x)$ in our notation.

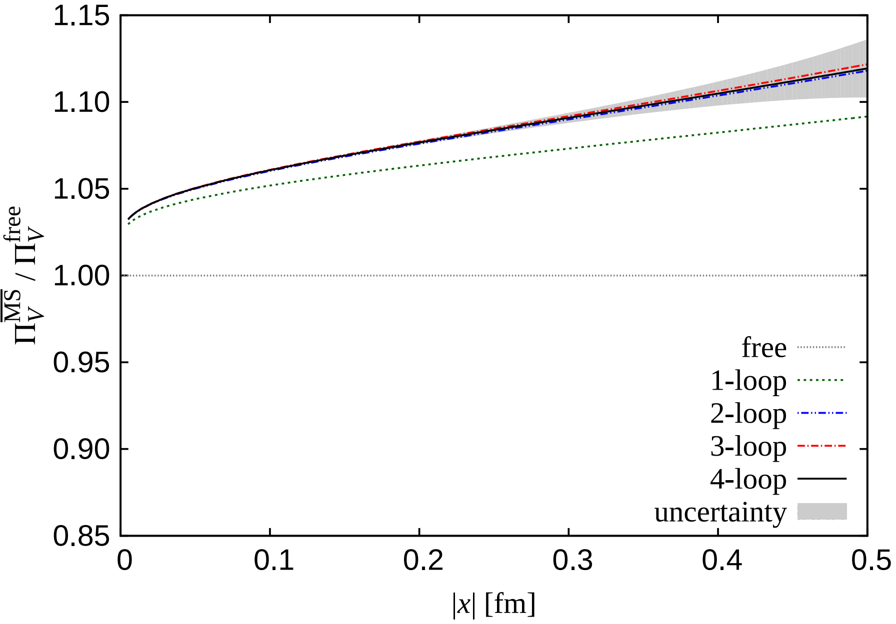

FIGURE 2.4: Perturbative expansion of the vector correlator renormalized in the $\overline{\rm MS}$ scheme with $n_f = 3$. The results of the perturbative series (2.15) at the optimal scale $\mu_x^{*,\rm opt}$ truncated at a_s^0 (fine-dotted), a_s (dotted), a_s^2 (dashed double-dotted), a_s^3 (dashed dotted), and a_s^4 (solid) are plotted as functions of $|x|$.

Numerically, the perturbative coefficients $C_i^S(\mu_x, \mu_x)$ and $C_i^S(2{\rm e}^{-\gamma_E}\mu_x, 2{\rm e}^{-\gamma_E}\mu_x)$ are obtained as

$$\begin{aligned} C_1^S(\mu_x,\mu_x) &= 0.20294, \\ C_2^S(\mu_x,\mu_x) &= -20.197 + 0.56314 n_f, \\ C_3^S(\mu_x,\mu_x) &= 7.8854 - 7.5318 n_f + 0.37635 n_f^2, \\ C_4^S(\mu_x,\mu_x) &= 500.95 + 40.402 n_f - 5.3403 n_f^2 + 0.18479 n_f^3, \end{aligned} \tag{2.18}$$

$$\begin{aligned} C_1^S(2{\rm e}^{-\gamma_E}\mu_x, 2{\rm e}^{-\gamma_E}\mu_x) &= \frac{2}{3}, \\ C_2^S(2{\rm e}^{-\gamma_E}\mu_x, 2{\rm e}^{-\gamma_E}\mu_x) &= -17.766 + 0.48193 n_f, \\ C_3^S(2{\rm e}^{-\gamma_E}\mu_x, 2{\rm e}^{-\gamma_E}\mu_x) &= -14.656 - 6.3172 n_f + 0.32333 n_f^2, \\ C_4^S(2{\rm e}^{-\gamma_E}\mu_x, 2{\rm e}^{-\gamma_E}\mu_x) &= 450.45 + 25.502 n_f - 3.8057 n_f^2 + 0.14697 n_f^3. \end{aligned} \tag{2.19}$$

For $n_f = 3$, they are

$$\begin{aligned} \Pi_S^{\overline{\rm MS}}(\mu_x; x)\Big|_{n_f=3} = \frac{3}{\pi^4 x^6}\Big(&1 + 0.20294 a_s(\mu_x) - 18.507 a_s(\mu_x)^2 \\ &- 11.323 a_s(\mu_x)^3 + 579.08 a_s(\mu_x)^4 + O(a_s^5)\Big), \end{aligned} \tag{2.20}$$

$$\Pi_S^{\overline{\rm MS}}(2{\rm e}^{-\gamma_E}\mu_x;x)\Big|_{n_f=3} = \frac{3}{\pi^4 x^6}\Big(1+0.66667a_s(2{\rm e}^{-\gamma_E}\mu_x)-16.321a_s(2{\rm e}^{-\gamma_E}\mu_x)^2$$
$$-30.698a_s(2{\rm e}^{-\gamma_E}\mu_x)^3+496.67a_s(2{\rm e}^{-\gamma_E}\mu_x)^4+O(a_s^5)\Big). \quad (2.21)$$

Figure 2.5 shows the convergence of (2.20). The correlator in the figure is normalized by the tree-level one, $\Pi_S^{\rm free}(x) = 3/\pi^4 x^6$. The scalar channel also shows poor convergence. The BLM scale is not directly applicable for scale dependent quantities. In fact, the BLM scale of the scalar correlator renormalized at μ_x is unstable, *i.e.* $\mu_x^{\rm BLM} \simeq 8.8\mu_x$ for $\Pi_S^{\overline{\rm MS}}(2{\rm e}^{-\gamma_E}\mu_x;x)$ while $\mu_x^{\rm BLM} \simeq 4\times 10^3\mu_x$ for $\Pi_S^{\overline{\rm MS}}(\mu_x;x)$.

Since the purpose of this work is to determine the renormalization constant at 2 GeV in the $\overline{\rm MS}$ scheme, we perform the scale evolution of the scalar correlator (2.17) from μ_x' to 2 GeV by a numerical integral of the mass anomalous dimension [51,52]. Figure 2.6 shows the scalar correlator calculated from the perturbative series (2.20) and the scale evolution. This calculation is convergent only below $|x| \sim 0.06$ fm. Such a poor convergence comes from large perturbative coefficients and the large coupling constant $a_s(\mu_x)$ in (2.20).

Although the scalar correlator $\Pi_S^{\overline{\rm MS}}(2~{\rm GeV};x)$ after the scale evolution has to be independent of both the scales μ_x^* and μ_x', finite order calculations may depend on them. Figure 2.7 shows the dependences on μ_x^* and μ_x' of the four-loop results at four representative distances renormalized at 2 GeV in the $\overline{\rm MS}$ scheme. To choose optimal values of μ_x^* and μ_x', we focus on the region with mild dependence of the correlator. We choose the optimal values of $\mu_x'(=\mu_x'^{\rm \,opt})$ as indicated by the dashed lines in Fig. 2.7. On these lines, the correlator depends on μ_x^* mildly and the dependence on μ_x' is also relatively small. Numerically, the choice is

$$\mu_x'^{\rm \,opt} = {\rm e}^{0.8}\mu_x \simeq \frac{2.2}{x}. \quad (2.22)$$

The detailed dependence of the scalar correlator on μ_x^* at $\mu_x' = \mu_x'^{\rm \,opt}$ is shown in Fig. 2.8 for several distances in 0.2–0.46 fm, where we determine the renormalization factor of the scalar operator. These figures show results at each loop order up to the four-loop level. We then choose the optimal value $\mu_x^{*,\rm opt}$ of the scale μ_x^* as the value which minimizes the dependence on μ_x^*,

$$\mu_x^{*,\rm opt} = {\rm e}^{1.05}\mu_x \simeq \frac{2.9}{x}. \quad (2.23)$$

We estimate the uncertainty by varying μ_x^* in a region including $\mu_x^{*,\rm opt}$ in the middle as we did for the vector channel. Since the coupling constant blows up as μ_x^* approaches $\Lambda_{\rm QCD}$, we need to avoid too small μ_x^*. Therefore, our choice is $[\frac{1}{1.6}\mu_x^{*,\rm opt}, 1.6\mu_x^{*,\rm opt}]$ in order not to use the coupling constant at the scale smaller than 0.75 GeV. The region is shown by the gray band in Fig. 2.8.

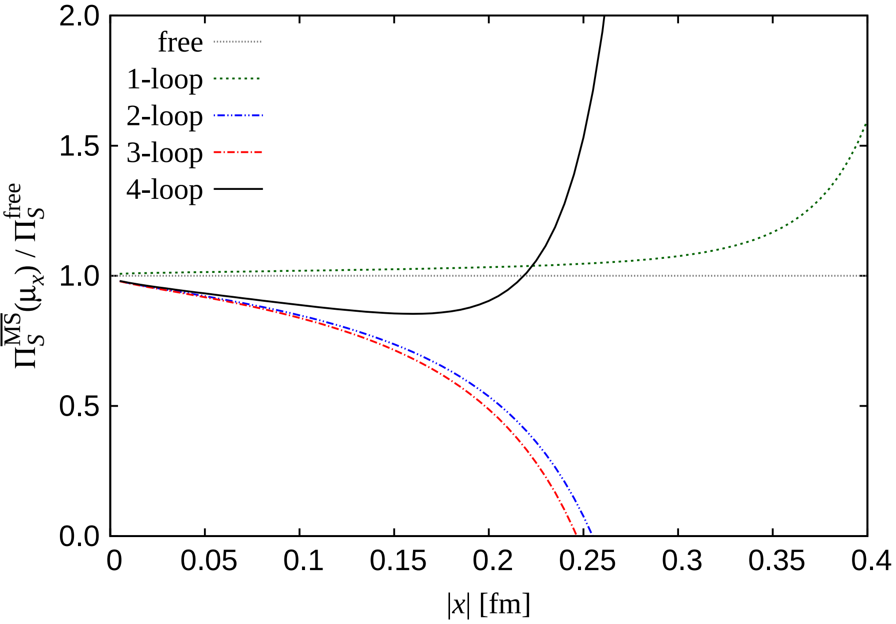

FIGURE 2.5: Scalar correlator renormalized at μ_x in the $\overline{\mathrm{MS}}$ scheme for $n_f = 3$. The results of (2.20) truncated at a_s^0 (fine-dotted), a_s (dotted), a_s^2 (dashed double-dotted), a_s^3 (dashed dotted), and a_s^4 (solid) are plotted.

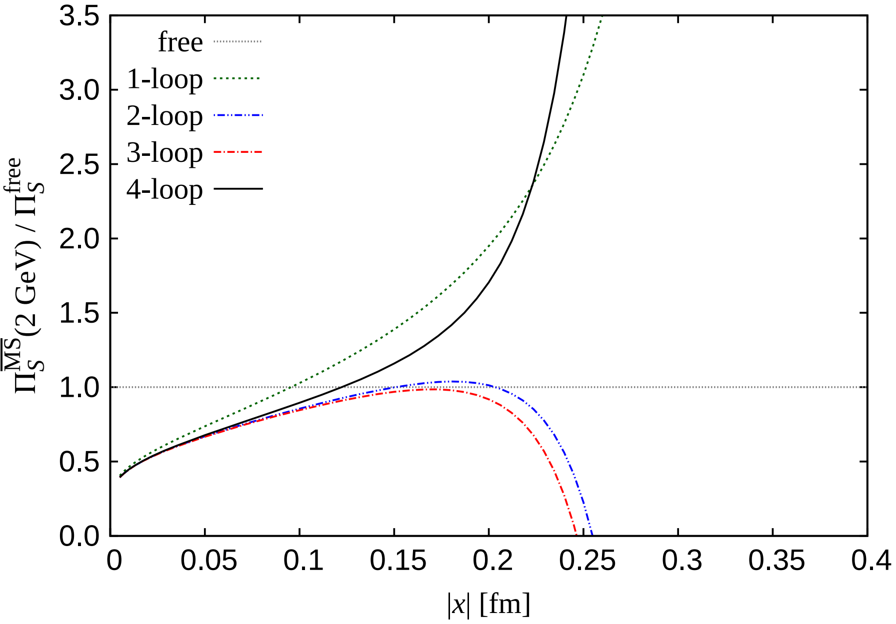

FIGURE 2.6: Scalar correlator renormalized at 2 GeV in $\overline{\mathrm{MS}}$ scheme for $n_f = 3$, which is calculated from the perturbative series (2.20) and the scale evolution. The results truncated at a_s^0 (fine-dotted), a_s (dotted), a_s^2 (dashed double-dotted), a_s^3 (dashed dotted), and a_s^4 (solid) are plotted.

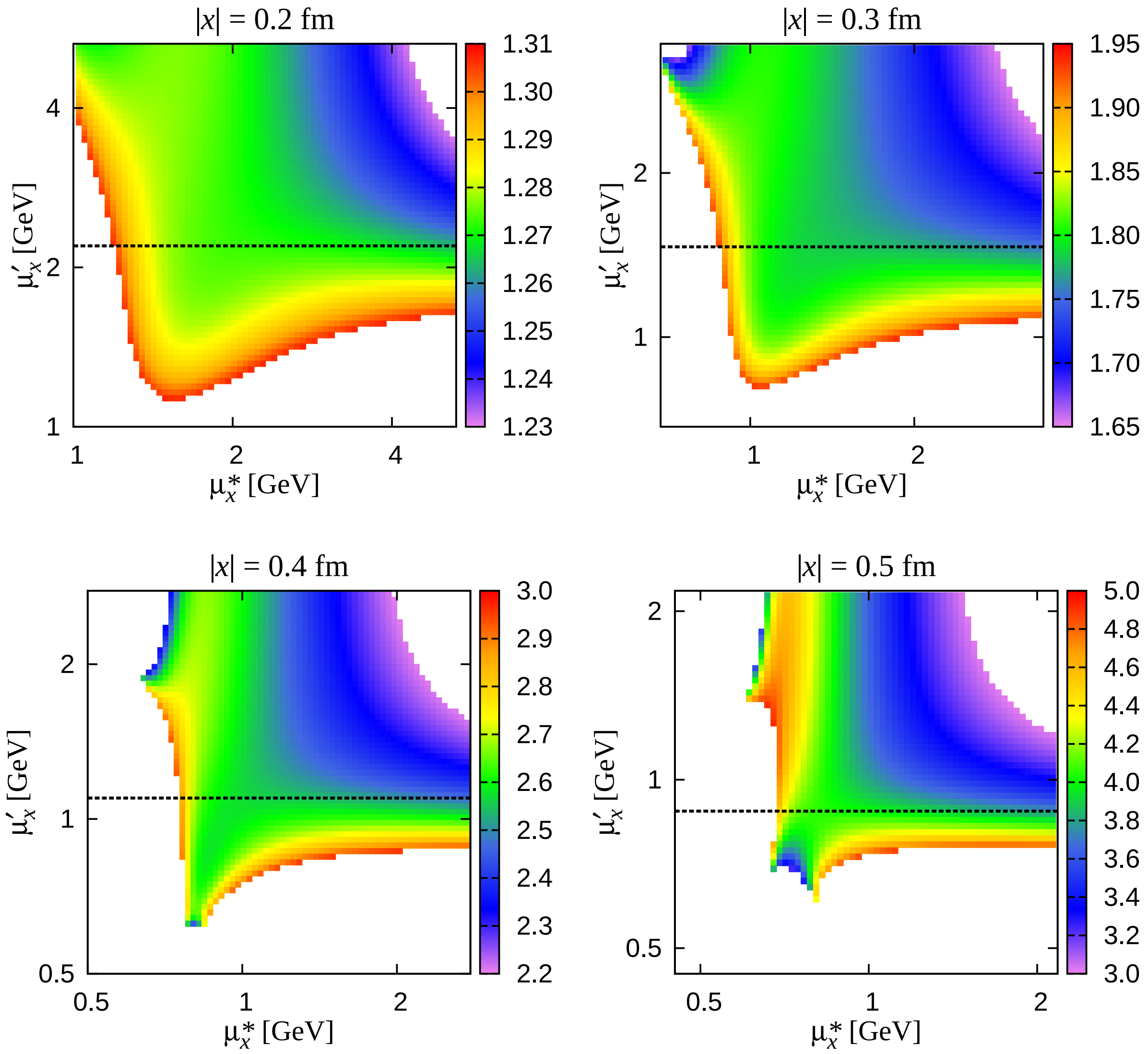

FIGURE 2.7: $\Pi_S^{\overline{\rm MS}}(2~{\rm GeV};x)/\Pi_S^{\rm free}(x)$ at the four-loop level at $n_f = 3$. The results at the specific distances 0.2 fm (top/left), 0.3 fm (top/right), 0.4 fm (bottom/left), and 0.5 fm (bottom/right) are shown as functions of μ_x^* and μ_x'. The dashed lines stand for our choice of μ_x', where the correlator shows small sensitivity to μ_x' and μ_x^*.

Setting μ_x' and μ_x^* by (2.22) and (2.23), we obtain the following numerical expansion at $n_f = 3$,

$$\Pi_S^{\overline{\rm MS}}(\mu_x'^{\,\rm opt};x)\Big|_{n_f=3} = \frac{3}{\pi^4 x^6}\Big(1 + 3.4029 a_s(\mu_x^{*,\rm opt}) + 9.7142 a_s(\mu_x^{*,\rm opt})^2 + 1.7011 a_s(\mu_x^{*,\rm opt})^3 + 26.366 a_s(\mu_x^{*,\rm opt})^4 + O(a_s^5)\Big), \tag{2.24}$$

whose coefficients are smaller than those in the expansion (2.20), (2.21) especially for the coefficients of $O(a_s^4)$. Evolving the renormalization scale of the correlator to 2 GeV, we obtain a well

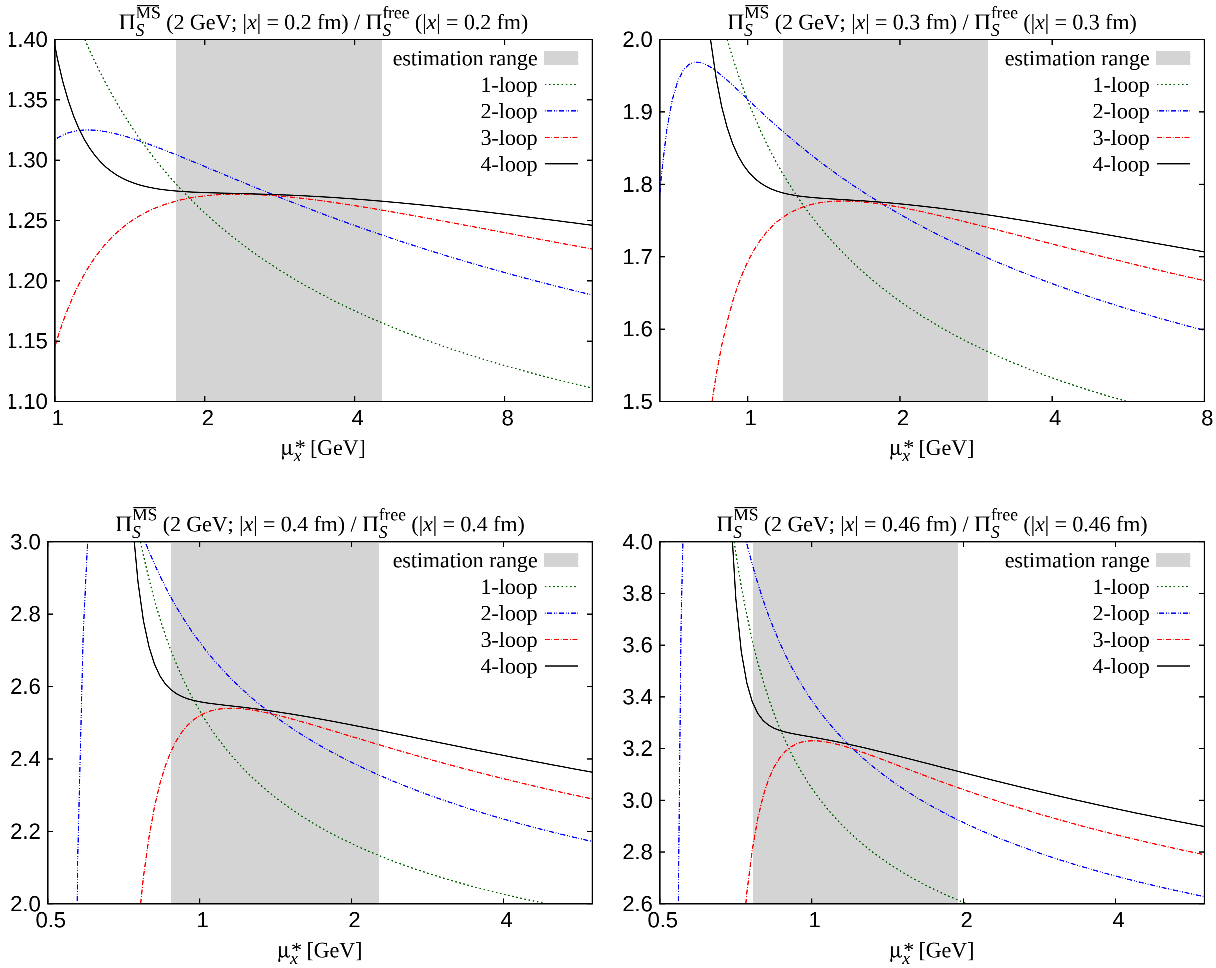

FIGURE 2.8: Scalar correlator renormalized at 2 GeV in the $\overline{\rm MS}$ scheme at the specific distances 0.2 fm (top/left), 0.3 fm (top/right), 0.4 fm (bottom/left), and 0.46 fm (bottom/right) as functions of μ_x^*. They are calculated at $n_f = 3$ and μ_x' is set by (2.22). The results truncated at a_s (dotted), a_s^2 (dashed double-dotted), a_s^3 (dashed dotted), and a_s^4 (solid) are plotted. The gray band represents the region in which we estimate the uncertainty of the perturbative calculation.

convergent correlator as shown in Fig. 2.9. The figure also shows the uncertainty of the perturbative calculation by the gray band, which is estimated by the maximum difference between the correlator at $\mu_x^* = \mu_x^{*,\rm opt}$ and those at μ_x^* in $[\frac{1}{1.6}\mu_x^{*,\rm opt}, 1.6\mu_x^{*,\rm opt}]$.

2.3 Momentum space correlators and dispersion relation

As mentioned in Section 2.1, current correlators in the coordinate space is convenient in the sense that they do not contain the contact terms. On the other hand, current correlators in the momentum space also have other advantages. The vector and axial-vector channels in the momentum space is decomposed into the transversal and longitudinal components and the decomposed parts are directly related to experiments as well as the Ward-Takahashi identity. In

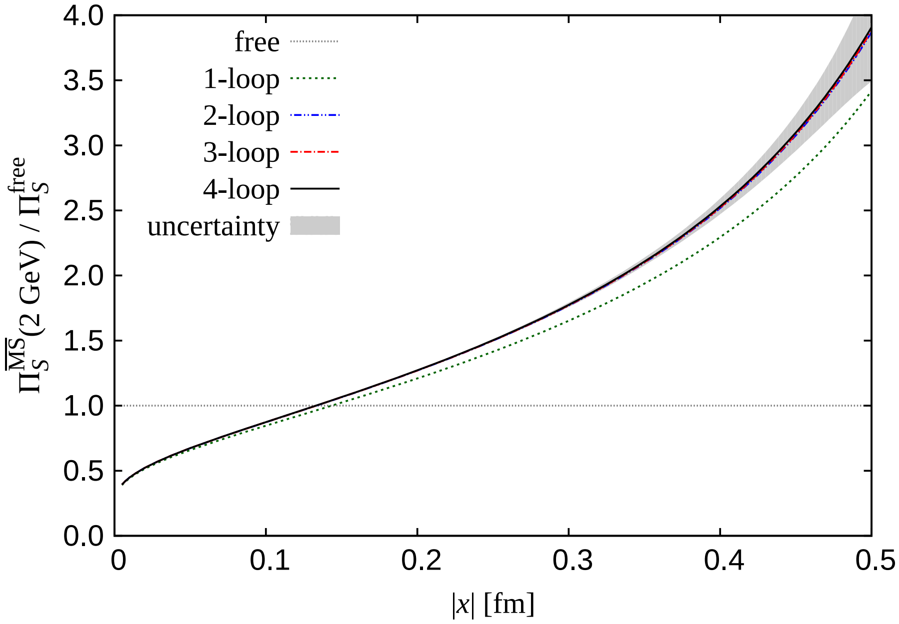

FIGURE 2.9: Scalar correlator renormalized at 2 GeV in the $\overline{\rm MS}$ scheme at $n_f = 3$. The scale parameters μ'_x and μ^*_x are set by (2.22) and (2.23). The results truncated at a_s^0 (fine-dotted), a_s (dotted), a_s^2 (dashed double-dotted), a_s^3 (dashed dotted), and a_s^4 (solid) are plotted. The gray region stands for the uncertainty of higher order corrections, which is estimated by the sensitivity to μ^*_x.

this section, we summarize the treatment of the momentum space correlators.

Current correlators in the momentum space are defined by the Fourier transforms

$$\widetilde{\Pi}_{S/P}(q) = \int \mathrm{d}^4x\, \mathrm{e}^{-\mathrm{i}qx}\, \Pi_{S/P}(x), \tag{2.25}$$

$$\widetilde{\Pi}_{V/A,\mu\nu}(q) = \int \mathrm{d}^4x\, \mathrm{e}^{-\mathrm{i}qx}\, \Pi_{V/A,\mu\nu}(x), \tag{2.26}$$

where q denotes the momentum variable in the Euclidean space.

The vector and axial-vector correlators can be decomposed as

$$\begin{aligned}\widetilde{\Pi}_{V/A,\mu\nu}(q) &= (q_\mu q_\nu - q^2\delta_{\mu\nu})\widetilde{\Pi}^{(1)}_{V/A}(-q^2) + q_\mu q_\nu \widetilde{\Pi}^{(0)}_{V/A}(-q^2)\\ &= (q_\mu q_\nu - q^2\delta_{\mu\nu})\widetilde{\Pi}^{(1+0)}_{V/A}(-q^2) + q^2\delta_{\mu\nu} \widetilde{\Pi}^{(0)}_{V/A}(-q^2),\end{aligned} \tag{2.27}$$

where $\widetilde{\Pi}^{(J)}_{V/A}(-q^2)$ stands for the correlator[2] associated with the hadrons of spin J and $\widetilde{\Pi}^{(1+0)}_{V/A}(-q^2)$ is defined by the sum of them,

$$\widetilde{\Pi}^{(1+0)}_{V/A}(-q^2) = \widetilde{\Pi}^{(1)}_{V/A}(-q^2) + \widetilde{\Pi}^{(0)}_{V/A}(-q^2). \tag{2.28}$$

---

[2] The negative sign of the argument $-q^2$ is conventional for Euclidean momenta.

In the coordinate space, any simple decomposition such as (2.27) cannot be obtained for full QCD[3]. The Ward-Takahashi identity guarantees $\Pi^{(0)}_V(-q^2) = 0$ in the isospin limit.

These decomposed parts of the correlators are related to experimental observables through the dispersion relation,

$$\widetilde{\Pi}^{(J)}_{V/A}(-q^2) = \frac{1}{\pi}\int_0^\infty \mathrm{d}s \frac{\mathrm{Im}\,\widetilde{\Pi}^{(J)}_{V/A}(s)}{(s+q^2)} - \text{subtractions}. \tag{2.29}$$

Here, the second term is to eliminate the divergence in the integral. The subtraction therefore leaves an unphysical arbitrary constant, which is the contact term.

For the vector channel, the imaginary part in (2.29) is related to the R-ratio from the electron-positron annihilation [53]

$$R_V(s) = \frac{\sigma(e^+e^- \to \text{hadrons}(V,s))}{\sigma(e^+e^- \to \mu^+\mu^-(s))}, \tag{2.30}$$

where $\sigma(X)$ stands for the total cross section for the reaction X. The electron-positron annihilation experiment measures the cross section at any scale above two times the electron mass and therefore observes the signals of strangeness and heavier particles as well as the up and down quarks. Since the electromagnetic current is composed of a combination of the flavor singlet and non-singlet currents, this experimental data involve both the flavor singlet and non-singlet channels. Applying the optical theorem, one can derive the relation

$$\mathrm{Im}\,\widetilde{\Pi}^{(1)}_V(s) = \frac{1}{6\pi}R_V(s). \tag{2.31}$$

The imaginary part in (2.29), as well as the ratio $R^{(J)}_V(s)$, is also related to the hadronic τ decay processes as reviewed in [54, 55]. The connection to the imaginary part is established through the spectral functions defined by

$$\rho^{(J)}_{V/A}(s) = \frac{m_\tau^2}{6|V_{ud}|^2 S_{\mathrm{EW}}} \frac{B(\tau^- \to \nu_\tau V/A(J))}{B(\tau^- \to \nu_\tau e^- \bar{\nu}_e)} \frac{\mathrm{d}N_{V/A}}{N_{V/A}\mathrm{d}s} \left[\left(1-\frac{s}{m_\tau^2}\right)^2\left(1+\frac{2s}{m_\tau^2}\right)\right]^{-1}. \tag{2.32}$$

Here, the Cabibbo-Kobayashi-Maskawa (CKM) matrix $|V_{ud}| = 0.97418(19)$ is taken from [56], S_{EW} accounts for the electroweak radiative corrections [57, 58]. We use the value $S_{\mathrm{EW}} = 1.0199(6)$ from [59]. $B(\tau^- \to \nu_\tau X)$ stands for the branching fraction of the decay process $\tau^- \to \nu_\tau X$. We use $B(\tau^- \to \nu_\tau e^- \bar{\nu}_e) = 17.83(4)\%$ reported by [60]. The normalized invariant mass-squared distribution $\mathrm{d}N_{V/A}/N_{V/A}\mathrm{d}s$ is measured by ALEPH [13, 39, 61–63] and OPAL [18]. We use the latest ALEPH data [39], whose values multiplied by the branching fraction $B(\tau^- \to \nu_\tau V/A(1))$ are found in [64]. The relation between the spectral functions and the

---

[3] Indeed, massless correlators in perturbation theory can be simply decomposed as shown in [38]. Considering mass corrections or OPE as discussed in Section 2.4, the projection operators change with the dimension of operators.

imaginary part of vacuum polarization is given by

$$\mathrm{Im}\,\widetilde{\Pi}^{(J)}_{V/A}(s) = \frac{1}{2\pi}\rho^{(J)}_{V/A}(s). \tag{2.33}$$

In perturbation theory with massless quarks, chiral symmetry guarantees the degeneracy of the spectral functions

$$\mathrm{Im}\,\widetilde{\Pi}^{(J)}_{V}(s)\big|^{\mathrm{pert}} = \mathrm{Im}\,\widetilde{\Pi}^{(J)}_{A}(s)\big|^{\mathrm{pert}}, \tag{2.34}$$

which is calculated up to the four-loop level for $J = 1$ [65, 66]. For $J = 0$, it vanishes in the isospin limit. Applying this perturbative spectral function to the dispersion relation (2.29) and performing Fourier transform to the position space, we obtain the vector correlator in perturbation theory, which is consistent with that in the previous section.

In the QCD vacuum, chiral symmetry is spontaneously broken and therefore the spectral functions of the vector and axial-vector channels are quite different at low energies. The difference is seen from the tau decay experiments for $J = 1$. For $J = 0$ the spectral functions of the vector channel is always zero, while that of the axial-vector channel contains the pion pole in the form $\propto f_\pi^2\delta(s - m_\pi^2)$ and a tiny correction of the excited states.

2.4 Mass correction and OPE

In perturbation theory with massless quarks, the degeneracies between the scalar and pseudoscalar channel, the vector and axial-vector channel are guaranteed. In the real QCD vacuum, these degeneracies are broken by the spontaneous breaking of chiral symmetry as well as the non-vanishing quark masses. In this section, we explain the corrections to the perturbative correlators based on the Operator Product Expansion (OPE), which is an idea to describe the non-perturbative effects as an expansion of (vacuum expectation values of) operators.

At first we discuss the OPE of the scalar and pseudoscalar correlators. In the momentum space, the OPE of the scalar and pseudoscalar correlators are sketched as

$$\widetilde{\Pi}^{\mathrm{OPE}}_{S/P}(-q^2) = \widetilde{\Pi}^{\mathrm{pert}}_{S/P}(-q^2) + \sum_{\mathcal{O}} \widetilde{C}^{S/P}_{\mathcal{O}}(q^2) q^{2-\dim\mathcal{O}}\langle\mathcal{O}\rangle, \tag{2.35}$$

where the first term on the RHS corresponds to the perturbative contribution including the mass corrections. The second term represents the non-perturbative effects. Here the operator $\mathcal{O}$ is

$$\mathcal{O} \in \{m_q\bar{q}q, \alpha_s G^2, m_q g_s\bar{q}Gq, \alpha_s(\bar{q}q)^2, \cdots\}, \tag{2.36}$$

and each Wilson coefficient $\widetilde{C}^{S/P}_{\mathcal{O}}$ is $O(\alpha_s^0)$ and do not have mass dimensions. In general, $\widetilde{C}^{\mathrm{S/P}}_{\mathcal{O}}$ depend on q^2 logarithmically such as $\ln(q^2/\mu^2)$ and mass corrections m_q^2/q^2. These coefficients

TABLE 2.1: Some relations between the momentum formula and the coordinate formula through Fourier transforms.

Momentum space	Coordinate space
$\frac{1}{q^2}$	$\frac{1}{4\pi^2}\frac{1}{x^2}$
$\frac{1}{q^2}\ln q^2$	$-\frac{1}{4\pi^2}\frac{1}{x^2}\ln^2 x^2$
$\frac{1}{q^4}(q_\mu q_\nu - q^2\delta_{\mu\nu})$	$-\frac{1}{4\pi^2}\frac{1}{x^2}\left(\frac{x_\mu x_\nu}{x^2}+\frac{\delta_{\mu\nu}}{2}\right)$
$\frac{1}{q^4}$	$-\frac{1}{16\pi^2}\ln x^2$
$\frac{1}{q^4}\ln q^2$	$\frac{1}{64\pi^2}\ln^2 x^2$
$\frac{1}{q^6}(q_\mu q_\nu - q^2\delta_{\mu\nu})$	$-\frac{1}{32\pi^2}\frac{x\mu x_\nu}{x^2}+\frac{3\delta_{\mu\nu}}{64\pi^2}\ln x^2$
$\frac{1}{q^6}$	$\frac{1}{128\pi^2}\ln x^2$

are known up to $\dim\mathcal{O}=8$ [4,67,68]. The Wilson coefficients at $\dim\mathcal{O}=4,6$ read

$$\widetilde{C}^{S/P}_{m\bar{q}q} = (1\pm 2) \mp \frac{2m_q^2}{q^2} + O(\alpha_s/\pi, m_q^4/q^4), \tag{2.37a}$$

$$\widetilde{C}^{S/P}_{\alpha_s G^2} = \frac{1}{8\pi} - \frac{(2\mp 9)m_q^2}{12\pi q^2} \mp \frac{m_q^2}{2\pi q^2}\ln q^2 + O(\alpha_s/\pi, m_q^4/q^4), \tag{2.37b}$$

$$\widetilde{C}^{S/P}_{mg_s\bar{q}Gq} = \pm 1 + O(\alpha_s/\pi, m_q^2/q^2), \tag{2.37c}$$

$$\widetilde{C}^{S/P}_{\alpha_s(\bar{q}q)^2} = -\frac{16\pi(4\pm 11)}{27} + O(\alpha_s/\pi, m_q^2/q^2). \tag{2.37d}$$

Here, the contribution of the four-quark condensate $\widetilde{C}^{S/P}_{a_s(\bar{q}q)^2}$ is calculated using the vacuum saturation assumption [69].

The short-distance behavior of the correlators in the coordinate space is understood by the Fourier transform

$$\Pi^{\mathrm{OPE}}_{S/P}(x^2) = \int \frac{\mathrm{d}^4 q}{(2\pi)^4}\mathrm{e}^{\mathrm{i}qx}\widetilde{\Pi}^{\mathrm{OPE}}_{S/P}(-q^2) = \Pi^{\mathrm{pert}}_{S/P}(x^2) + \sum_{\mathcal{O}} C^{S/P}_{\mathcal{O}}(x^2)x^{\dim\mathcal{O}-6}\langle\mathcal{O}\rangle. \tag{2.38}$$

For the first term on the RHS, the massless part is already discussed in the previous section. Since the remaining contributions are relatively small in $\lesssim 0.5$ fm, we consider only the tree-level terms of them.

Table 2.1 summarizes the Fourier transforms between the momentum and coordinate space used for the derivation of following results. Using these relations, we obtain

$$C^{S/P}_{m\bar{q}q} = \frac{1\pm 2}{4\pi^2} \pm \frac{m_q^2}{8\pi^2}x^2\ln(x/x_0)^2 + O(\alpha_s/\pi, m_q^4 x^4), \tag{2.39a}$$

$$C^{S/P}_{\alpha_s G^2} = \frac{1}{32\pi^3} + \frac{(2\mp 9)m_q^2}{192\pi^3}x^2\ln(x/x_0)^2 \mp \frac{m_q^2}{128\pi^3}x^2\ln^2 x^2 + O(\alpha_s/\pi, m_q^4 x^4), \tag{2.39b}$$

$$C^{S/P}_{mg_s\bar{q}Gq} = \mp\frac{1}{16\pi^2}\ln(x/x_0)^2 + O(\alpha_s/\pi, m_q^2 x^2), \tag{2.39c}$$

$$C^{S/P}_{a_s(\bar{q}q)^2} = \frac{4 \pm 11}{27} \ln(x/x_0)^2 + O(\alpha_s/\pi, m_q^2 x^2). \tag{2.39d}$$

Here, the logarithmic contributions involve dimensionful variable x_0, which appears from divergences of the integral defining the Fourier transform and is regularization and scheme dependent[4].

Next we discuss the vector and axial-vector correlators. These correlators in the coordinate space and in the momentum spaces are related through the Fourier transform,

$$\Pi_{V/A,\mu\nu}(x) = \int \frac{\mathrm{d}^4 q}{(2\pi)^4} \mathrm{e}^{\mathrm{i}qx} \widetilde{\Pi}_{V/A,\mu\nu}(q). \tag{2.40}$$

The longitudinal component of these correlators, which is extracted by taking the divergence $\sum_\mu \partial_\mu \Pi_{V/A,\mu\nu}(x)$, is calculated using PCAC relation.

Before entering into the details of the OPE, we briefly review the result from the Ward-Takahashi identity. In the momentum space, the vector and axial-vector correlators are usually written as (2.27), whose second term, the longitudinal component, is extracted by multiplying momentum vectors,

$$\widetilde{\Pi}^{(0)}_{V/A}(-q^2) = \sum_{\mu,\nu} \frac{q_\mu q_\nu}{q^4} \widetilde{\Pi}_{V/A,\mu\nu}(q). \tag{2.41}$$

In the case of degenerate valence quarks, the longitudinal component of the vector correlator is exactly zero,

$$\widetilde{\Pi}^{(0)}_{V}(-q^2) = 0, \tag{2.42}$$

while the axial-vector channel behaves as [68,70]

$$\widetilde{\Pi}^{(0)}_{A}(-q^2) = \frac{4m_q}{q^4}\langle\bar{q}q\rangle + \frac{4m_q^2}{q^4}\widetilde{\Pi}_P(-q^2). \tag{2.43}$$

This is derived by the PCAC relation. In the isospin limit, the longitudinal component of the correlators in the position space is given by

$$\delta_{\mu\nu} \int \frac{\mathrm{d}^4 q}{(2\pi)^4} \mathrm{e}^{\mathrm{i}qx} q^2 \widetilde{\Pi}^{(0)}_{V}(-q^2) = 0, \tag{2.44}$$

$$\delta_{\mu\nu} \int \frac{\mathrm{d}^4 q}{(2\pi)^4} \mathrm{e}^{\mathrm{i}qx} q^2 \widetilde{\Pi}^{(0)}_{A}(-q^2) = \delta_{\mu\nu} \frac{m_q\langle\bar{q}q\rangle}{\pi^2 x^2} + O(m_q^2). \tag{2.45}$$

Here $O(m_q^2)$ on the RHS of (2.45) corresponds to the contribution of the pseudoscalar correlator in (2.43). In the coordinate space, the longitudinal component is extracted by taking the divergence instead of multiplying the momentum vector. Then, we obtain

$$-\frac{\pi^2}{2m_q} x^2 \sum_{\mu,\nu} x_\nu \partial_\mu \Pi_{A,\mu\nu}(x) = \langle\bar{q}q\rangle + O(m_q). \tag{2.46}$$

---

[4] More precisely, x_0 depends also on the corresponding operators, *i.e.* we need to distinguish x_0's in (2.39a)–(2.39d) such as $x_0^{\mathcal{O}}$ with the corresponding operator $\mathcal{O}$. Since this distinction is not important in this work, we do not distinguish them for simplicity.

In Section 5.2, we demonstrate that the numerical results for the left hand side show a good agreement with the value of the chiral condensate. Note that (2.46) is derived without OPE and there is no need to add any perturbative correction to the first term.

Next, we summarize the OPE of the vector and axial-vector correlators. The longitudinal component of the vector correlator is, again, identical to zero (2.44), while the axial vector one is given by the Fourier transform of (2.43). The result is

$$\begin{aligned}\delta_{\mu\nu}\int\frac{\mathrm{d}^4q}{(2\pi)^4}\mathrm{e}^{\mathrm{i}qx}q^2\widetilde{\Pi}_A^{(0)}(-q^2) = {} & \delta_{\mu\nu}\frac{m_q\langle\bar{q}q\rangle}{\pi^2x^2}\\ & -\delta_{\mu\nu}\frac{3m_q^2}{8\pi^4x^2}\ln^2(x^2/x_0^2)\\ & +\delta_{\mu\nu}\left[-\frac{m_q^2\langle a_sGG\rangle}{32\pi^2}+\frac{m_q^3\langle\bar{q}q\rangle}{4\pi^2}\right]\ln(x/x_0)^2+\cdots .\end{aligned} \tag{2.47}$$

For the transversal part, the OPE in the momentum space is written as

$$\widetilde{\Pi}_{V/A}^{(1+0),\mathrm{OPE}}(-q^2) = \widetilde{\Pi}_{V/A}^{(1+0),\mathrm{pert}}(-q^2)+\sum_{\mathcal{O}}\widetilde{C}_{\mathcal{O}}^{V/A}(q^2)q^{-\dim\mathcal{O}}\langle\mathcal{O}\rangle, \tag{2.48}$$

$$\int\frac{\mathrm{d}^4q}{(2\pi)^4}\mathrm{e}^{\mathrm{i}qx}(q_\mu q_\nu-q^2\delta_{\mu\nu})\widetilde{\Pi}_{V/A}^{(1+0),\mathrm{OPE}}(-q^2) = \Pi_{V/A}^{\mathrm{pert}}(x^2)+\sum_{\mathcal{O}}C_{\mathcal{O},\mu\nu}^{V/A}(x)x^{\dim\mathcal{O}-6}\langle\mathcal{O}\rangle. \tag{2.49}$$

The Wilson coefficients in the momentum space are found to be [4, 68]

$$\widetilde{C}_{m\bar{q}q}^{V/A} = 2-\frac{8}{3}\frac{m_q^2}{q^2}+O(a_s,m_q^4/q^4), \tag{2.50a}$$

$$\widetilde{C}_{a_sG^2}^{V/A} = -\frac{1}{12}+\frac{m_q^2}{3q^2}+O(a_s,m_q^4/q^4), \tag{2.50b}$$

$$\widetilde{C}_{mg_s\bar{q}Gq} = 0, \tag{2.50c}$$

$$\widetilde{C}_{a_s(\bar{q}q)^2}^{V/A} = -\frac{32(2\mp 9)\pi^2}{81}+O(a_s,m_q^2/q^2), \tag{2.50d}$$

which lead to those in the coordinate space

$$C_{m\bar{q}q,\mu\nu}^{V/A} = -\frac{1}{2\pi^2}\left(\frac{\delta_{\mu\nu}}{2}+\frac{x_\mu x_\nu}{x^2}\right)+\frac{m_q^2}{12\pi^2}x_\mu x_\nu-\frac{m_q^2\delta_{\mu\nu}}{8\pi^2}x^2\ln(x/x_0)^2+O(a_s,m_q^4x^4), \tag{2.51a}$$

$$C_{a_sG^2,\mu\nu}^{V/A} = \frac{1}{48\pi^2}\left(\frac{\delta_{\mu\nu}}{2}+\frac{x_\mu x_\nu}{x^2}\right)-\frac{m_q^2}{96\pi^2}x_\mu x_\nu+\frac{m_q^2\delta_{\mu\nu}}{64\pi^2}x^2\ln(x/x_0)^2+O(a_s,m_q^4x^4), \tag{2.51b}$$

$$C_{mg_s\bar{q}Gq,\mu\nu}^{V/A} = 0, \tag{2.51c}$$

$$C_{a_s(\bar{q}q)^2,\mu\nu}^{V/A} = \frac{2\mp 9}{81}\frac{x_\mu x_\nu}{x^2}-\frac{2\mp 9}{54}\delta_{\mu\nu}\ln(x/x_0)^2+O(a_s,m_q^2x^2). \tag{2.51d}$$

Summing over the Lorentz diagonal components both for the transversal and longitudinal components, we obtain the OPE of the scalar-contracted vector and axial-vector correlators

$$\Pi^{\mathrm{OPE}}_{V/A}(x) = \Pi^{\mathrm{pert}}_{V/A}(x) + \sum_{\mathcal{O}} C^{V/A}_{\mathcal{O}}(x^2) x^{\dim \mathcal{O} - 6} \langle \mathcal{O} \rangle, \tag{2.52}$$

where the Wilson coefficients read

$$C^{V/A}_{m\bar{q}q} = \frac{1 \mp 4}{2\pi^2} \mp \frac{m_q^2}{2\pi^2} x^2 \ln(x/x_0)^2 + O(a_s, m_q^4 x^4), \tag{2.53a}$$

$$C^{V/A}_{a_s G^2} = \frac{1}{16\pi^2} \pm \frac{m_q^2}{16\pi^2} x^2 \ln(x/x_0)^2 + O(a_s, m_q^4 x^4), \tag{2.53b}$$

$$C^{V/A}_{m g_s \bar{q} G q} = 0, \tag{2.53c}$$

$$C^{V/A}_{a_s (\bar{q}q)^2} = -\frac{4 \mp 18}{27} \ln(x/x_0)^2 + O(a_s, m_q^2 x^2). \tag{2.53d}$$

Thus far, we have skipped the evaluation of the mass corrections to the perturbative contribution. At tree-level, correlators of massive quarks are analytically calculated as follows. The propagator of a non-interacting massive quark is given [71,72] by

$$\begin{aligned} S_F^{\mathrm{cont}}(x, m_q) &= \int \frac{\mathrm{d}^4 q}{(2\pi)^4} \mathrm{e}^{\mathrm{i}qx} \frac{-\mathrm{i}\not{q} + m_q}{q^2 + m_q^2} \\ &= \frac{m_q \not{x}}{4\pi^2 |x|^3} K_1(m_q|x|) + \frac{m_q^2 \not{x}}{8\pi^2 x^2} \left[K_0(m_q|x|) + K_2(m_q|x|) \right] + \frac{m_q^2}{4\pi^2 |x|} K_1(m_q|x|), \end{aligned} \tag{2.54}$$

with K_i being the modified Bessel functions. Then we can construct the massive correlator in the tree-level by taking the contraction,

$$\Pi^{\mathrm{free}}_{\Gamma}(x, m_q) = \mathrm{Tr}[S_F(x, m_q) \Gamma S_F(-x, m_q) \Gamma]. \tag{2.55}$$

Thus, the mass correction to the perturbative contribution are calculated. At $O(m_q^2)$, the correction is given by

$$\Pi^{\mathrm{pert}}_{P/S}(x) - \Pi^{\mathrm{pert,massless}}_{P/S}(x) = -\frac{3(2 \pm 1) m_q^2}{4\pi^4 x^4} + O(\alpha_s/\pi, m_q^4/x^2), \tag{2.56}$$

$$\Pi^{\mathrm{pert}}_{V/A}(x) - \Pi^{\mathrm{pert,massless}}_{V/A}(x) = -\frac{6(1 \mp 1) m_q^2}{\pi^4 x^4} + O(\alpha_s/\pi, m_q^4/x^2). \tag{2.57}$$

2.5 Quark-hadron duality violation

In Section 2.3, we introduced the spectral functions and the dispersion relation to calculate the current correlators. It should be emphasized that the spectral function is defined on the positive real axis of the invariant mass-squared s, which is in the Minkowski domain. It is known that a spectral function explained by OPE in the Minkowski regime truncated at a finite dimension of operators disagrees with that in full QCD, *i.e.* the OPE no longer works in the Minkowski. At the same time, the resonance structure of hadrons does not vanish even in roughly perturbative region ($\sim 2\ \mathrm{GeV}^2$). This problem is referred to as the violation of quark-hadron duality or the duality violation [21–24]. In this section, we review the quark-hadron duality and its violation in the Minkowski regime.

The quark-hadron duality is the duality between perturbation theory or OPE, which is described in terms of quark and gluon degrees of freedom, and the hadronic picture. The violation of the quark-hadron duality means that a quantity explained by OPE disagrees with that in full QCD beyond the truncation uncertainty of the operator expansion and the perturbative expansion of the Wilson coefficients.

One can understand that the duality violation arises from the singularity of the instanton contributions. Although we do not imply the instantons can quantitatively explain the mechanism of the duality violation, an introduction of an instanton-based approach is convenient to understand qualitatively how the duality violation arises. In the following, we discuss the one fixed-size instanton model just for the purpose of orientation.

Propagator $G_{\mathrm{inst}}(x,y)$ of a massless quark interacting with an instanton is known [73]. In the Euclidean representation, it has the part

$$G_{\mathrm{inst}}(x,y) = \frac{\widetilde{G}}{(x-y)^4}\frac{1}{[(x-z)^2+\rho^2]^{l_1}[(y-z)^2+\rho^2]^{l_2}}, \tag{2.58}$$

where z is the central position of the instanton, ρ is the fixed instanton size, $\widetilde{G}$ is a polynomial of x and y including the Dirac matrices, and

$$l_{1,2} = \frac{1}{2} \text{ or } \frac{3}{2}, \quad l_1 + l_2 = 2. \tag{2.59}$$

The singularity at $x - y = 0$ exists even in the propagator without the instanton and is not related to the duality violation. There are other singular points in the Minkowski region, which are located at $(x-y)^2 = -4\rho^2$ when $z = (x+y)/2$. This singularity violates the quark-hadron duality as follows. The contribution of this singularity to a correlator in the momentum space $\widetilde{\Pi}^{\mathrm{sin}}_{\Gamma}(q)$ is sketched as

$$\begin{aligned}
\widetilde{\Pi}^{\mathrm{sin}}_{\Gamma}(q) &\propto \int \mathrm{d}^4x\, \mathrm{e}^{-\mathrm{i}q(x-y)} \int \mathrm{d}^4z \frac{1}{[(x-z)^2+\rho^2][(y-z)^2+\rho^2]^3} \\
&\propto \int \mathrm{d}^4x\, \mathrm{e}^{-\mathrm{i}qx} \frac{1}{(x^2+\rho^2)} \int \mathrm{d}^4z\, \mathrm{e}^{-\mathrm{i}qz} \frac{1}{(z^2+\rho^2)^3} \\
&\propto K_1(\rho|q|)K_{-1}(\rho|q|) \xrightarrow{\rho|q|\gg 1} \frac{1}{|q|}\mathrm{e}^{-2\rho|q|}.
\end{aligned} \tag{2.60}$$

For the vector and axial-vector channel, this singular contribution to the spin-decomposed correlators $\widetilde{\Pi}^{(J)}_{V/A}(-q^2)$ defined in (2.27) obeys $\widetilde{\Pi}^{(J),\mathrm{sin}}_{V/A}(-q^2) \propto |q|^{-3}\mathrm{e}^{-2\rho|q|}$, which leads to the oscillatory behavior of the spectral function

$$\rho^{(J),\mathrm{sin}}_{V/A}(s) \propto \frac{1}{s^{3/2}}\cos(2\rho\sqrt{s}), \quad \rho^{(J),\mathrm{sin}}_{V/A}(s) = \rho^{(J)}_{V/A}(x) - \rho^{(J),\mathrm{OPE}}_{V/A}(s), \tag{2.61}$$

at large $s = -q^2$ in the Minkowski regime. Here, $\rho^{(J),\mathrm{OPE}}_{V/A}(s)$ stands for the OPE of the spectral function $\rho^{(J)}_{V/A}(s)$. Although the instanton-based approach is a useful tool to see the occurrence of the duality violation, such a simple model cannot give quantitative prediction.

The effect of the duality violation is usually evaluated by another model, which is based on the following two assumptions:

- Large but finite N_c to see resonances with non-vanishing widths.
- Regge assumption to guess the equidistant resonances.

The validity of these assumptions are discussed in [23, 25–27]. This model is convenient to explain the fact that the resonances in the spectral functions occur with a finite width and a mostly same interval of s. In the limit $N_c \to \infty$, each resonance in the spectral functions is proportional to the Dirac delta function. Therefore, the spectral function is a sum of delta functions. In QCD with a finite $N_c = 3$, the resonances have finite width. The equidistant resonances are explained by the Regge theory [74, 75] combined with the large N_c.

Applying this resonance-based model, we finally the following parametrization for the spectral functions,

$$\rho^{(J)}_{\Gamma}(s) \xrightarrow{\text{large } s} \mathrm{e}^{-\delta^{(J)}_{\Gamma} - \gamma^{(J)}_{\Gamma} s} \sin\left(\alpha^{(J)}_{\Gamma} + \beta^{(J)}_{\Gamma} s\right) + \rho^{(J),\mathrm{pert}}_{\Gamma}(s), \tag{2.62}$$

with four unknown parameters $\alpha^{(J)}_{\Gamma}, \beta^{(J)}_{\Gamma}, \gamma^{(J)}_{\Gamma}$, and $\delta^{(J)}_{\Gamma}$. Here, the perturbative contribution $\rho^{(J),\mathrm{pert}}_{\Gamma}(s)$ to the spectral function is known up to the four-loop level [65, 66].

$$\begin{aligned}\rho^{(J),\mathrm{pert}}_{\Gamma}(s) = \frac{1}{2}\Big[&1 + a_s(\sqrt{s}) + (1.9857 - 0.1152 n_f) a_s(\sqrt{s})^2 \\ &+ \big(-6.63694 - 1.20013 n_f - 0.00518 n_f^2\big) a_s(\sqrt{s})^3 \\ &+ \big(-156.61 + 18.77 n_f - 0.7974 n_f^2 + 0.0215 n_f^3\big) a_s(\sqrt{s})^4\Big].\end{aligned} \tag{2.63}$$

The resonance model (2.62) is similar to the single instanton model (2.61) except for the dumping factor and the phase shift.

We fit the ALEPH data [39, 64] of spin one components of the vector and axial-vector channels by the fit functions (2.62) based on the resonance model. The chi square fitting is implemented simultaneously among the vector and axial-vector channels with the consideration of the correlations between all data values. The detail is explained in Appendix E.4.2. The fit range is chosen as $1.6\ \mathrm{GeV}^2 \leq s \leq 2.7\ \mathrm{GeV}^2$ both for the vector and axial-vector channles. The

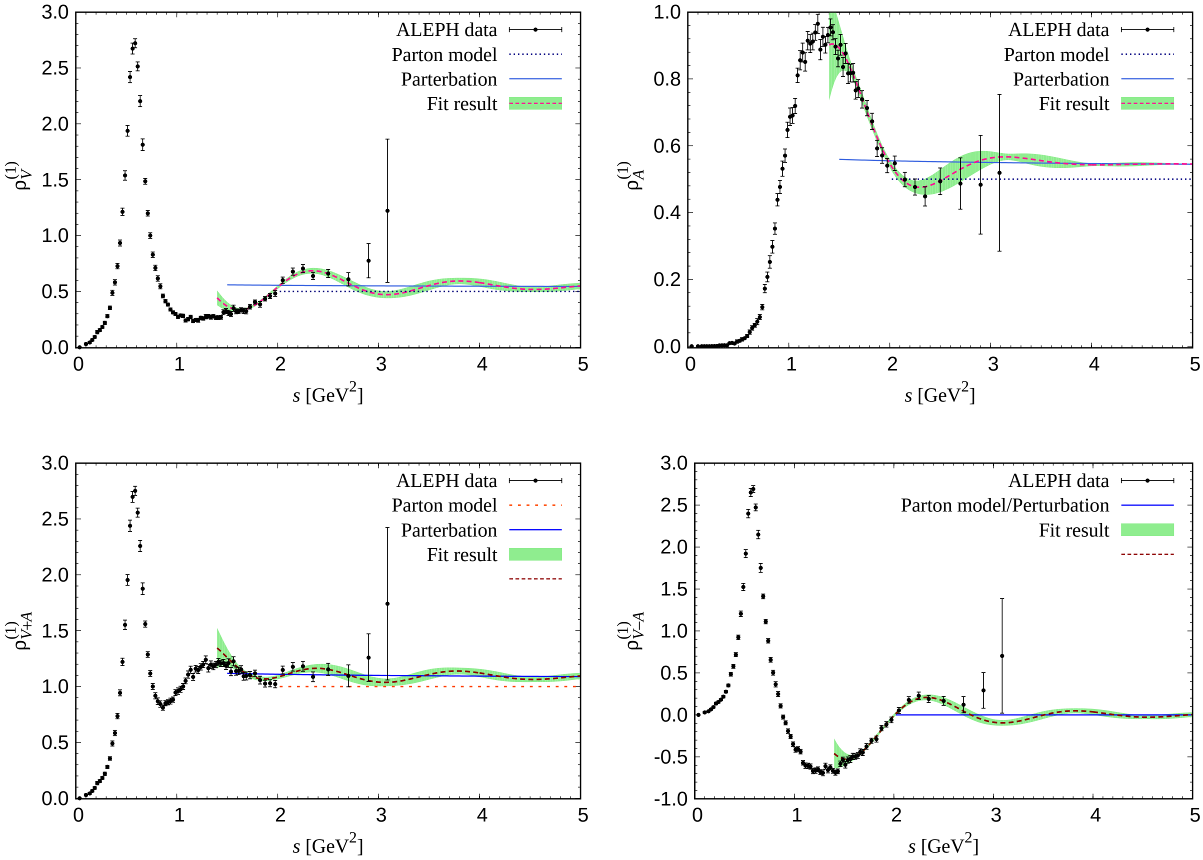

FIGURE 2.10: Spectral functions $\rho_\Gamma^{(1)}(s)$ measured by the ALEPH collaboration [30] for $\Gamma = V$ (top/left), $\Gamma = A$ (top/right), $\Gamma = V + A$ (bottom/left), and $\Gamma = V - A$ (bottom/right), plotted with the prediction of the parton model and perturbation theory, and the fit result according to the resonance model.

fit results read

$$\begin{aligned} &\delta_V^{(1)} = 0.32(27), \ \gamma_V^{(1)} = 0.72(9)\ \text{GeV}^{-2}, \ \alpha_V^{(1)} = -2.4(9), \ \beta_V^{(1)} = 4.3(2)\ \text{GeV}^{-2}, \\ &\delta_A^{(1)} = -1.5(5), \ \gamma_A^{(1)} = 1.7(2)\ \text{GeV}^{-2}, \ \alpha_A^{(1)} = 2.2(4.8), \ \beta_A^{(1)} = 3.6(1.2)\ \text{GeV}^{-2}. \end{aligned} \tag{2.64}$$

The chi square divided by the degrees of freedom is 1.28.

Figure 2.10 shows the four channels of the spectral functions, $\rho_V^{(1)}$ (top/left), $\rho_A^{(1)}$ (top/right), $\rho_{V+A}^{(1)} = \rho_V^{(1)} + \rho_A^{(1)}$(bottom/left), and $\rho_{V-A}^{(1)} = \rho_V^{(1)} - \rho_A^{(1)}$ (bottom/right) as functions of the invariant mass-squared s. Here, the experimental data (circles) and the fit results (dashed curve) as well as the predictions of perturbation theory (solid curve) and the parton model (dotted line) are plotted. As seen in the figure, the experimental data disagree with the prediction of perturbation theory in the region $s \lesssim 2.5\ \text{GeV}^2$. The fit result based on the resonance model also disagree with perturbation theory up to $s \simeq 3\ \text{GeV}^2$. These facts implies the quark-hadron duality is significantly violated and therefore the duality violating contribution need to be considered.

2.6 Correlators converted from experiments

Using the dispersion relation (2.29), we can convert the spectral functions to the corresponding correlators as

$$\Pi^{(1)}_{V/A}(x) = \sum_{\mu} \int \frac{\mathrm{d}^4 q}{(2\pi)^4} \mathrm{e}^{\mathrm{i}qx} (q_\mu q_\mu - q^2 \delta_{\mu\mu}) \widetilde{\Pi}^{(1)}_{V/A}(-q^2) = -3 \int \frac{\mathrm{d}^4 q}{(2\pi)^4} \mathrm{e}^{\mathrm{i}qx} q^2 \Pi^{(1)}_{V/A}(-q^2), \tag{2.65}$$

which is the contribution of the spin-one component. The dispersion relation in terms of $\rho^{(1)}_{V/A}$ is given by

$$\widetilde{\Pi}^{(1)}_{V/A}(-q^2) = \frac{1}{2\pi^2} \int_0^\infty \mathrm{d}s \frac{\rho^{(1)}_{V/A}(s)}{s+q^2}. \tag{2.66}$$

Inserting this to (2.65), we obtain

$$\Pi^{(1)}_{V/A}(x) = \frac{3}{8\pi^4} \int_0^\infty \mathrm{d}s\ s^{3/2} \rho^{(1)}_{V/A}(s) \frac{K_1(\sqrt{s}|x|)}{|x|}. \tag{2.67}$$

Thus, we can calculate the spin-one contribution to the correlators with the spectral function $\rho^{(1)}_{V/A}(s)$, which obtained from the experiment and perturbation theory.

The spin-zero contribution is treated as follows. In the isospin limit, the spin-zero contribution to the vector channel is exactly zero $\rho^{(0)}_V(s) = 0$ and therefore $\Pi_V(x) = \Pi^{(1)}_V$. The spin-zero component for the axial-vector channel contains, on the other hand, the pion pole. The magnitude of the pion pole is estimated from the pion decay constant through the PCAC relation. Thus, the axial-vector correlator including the pion pole can be calculated as

$$\Pi_A(x) \simeq \frac{3}{8\pi^4} \int_0^\infty \mathrm{d}s\ s^{3/2} \rho^{(1)}_A(s) \frac{K_1(\sqrt{s}|x|)}{|x|} - \frac{f_\pi^2 M_\pi^3}{4\pi^2} \frac{K_1(M_\pi |x|)}{|x|}. \tag{2.68}$$

The contribution of other poles of the excited states of the pion is negligible. Schäfer and Shuryak [14] converted the ALEPH data [61] to the Euclidean correlators in the coordinate space including the pion pole and the results were used for the tests of prediction of the quenched lattice calculation by DeGrand [8].

In this work, we analyze the quantity

$$R_{V/A}(x) = \frac{\Pi^{(1)}_{V/A}(x)}{\Pi^{\text{free}}_{V/A}(x)|_{m_q=0}}, \tag{2.69}$$

where the pion pole in the axial-vector channel is dropped, using the latest ALEPH data [39] and the 14 lattice ensembles dynamically generated with the simulation parameters closer to the physical point than those in [8]. We focus only on the spin-one components, *i.e.* we do not include the second term on the RHS of (2.68) in the analysis because the complicated mass dependence of the pion pole could make the chiral extrapolation more difficult.

Figure 2.11 shows $R_{V/A}(x)$ calculated from the following three methods. One is based on

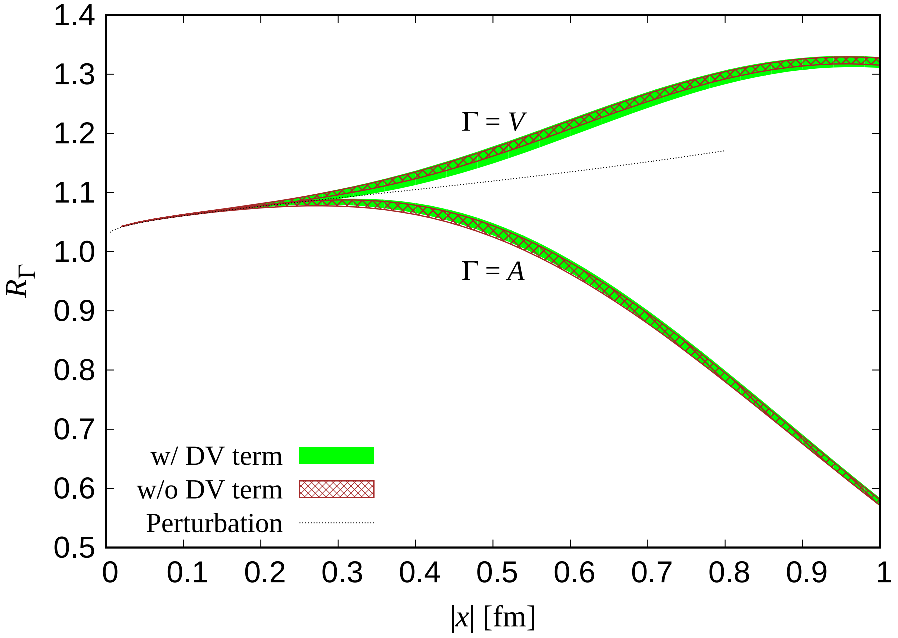

FIGURE 2.11: $R_{V/A}$ calculated from the ALEPH spectral functions, perturbation theory, and resonance based model plotted as functions of $|x|$.

perturbation theory, in which the vector and axial-vector channels are degenerate. The second method is to use the ALEPH spectral function for $s \leq 2.7$ GeV^2 and perturbation theory for larger s. The other is the resonance model which is explained in the previous section. In this method, we use the ALEPH data for $s \leq 2.7$ GeV^2 and the fit result (2.64) of the model for larger s. As expected, the effect of the duality violation does not appear significantly in the Euclidean domain. We can observe a slight dependence on the treatment of the spectral function in $s > m_\tau^2$. The results of the combined channels $V + A$ and $V - A$ are shown with the lattice results in Section 5.1 (Figs. 5.1,5.5) and Appendix F (Figs. F.5,F.6). We find that the perturbative region is seen in $x \lesssim 0.2$ fm and the degeneracy between the vector and axial-vector channels is violated already at $x = 0.3$ fm. Therefore the discretization effects need to be under control in the region $x \gtrsim 0.2$ fm to determine the strong coupling constant from lattice calculations.

It is also useful for the analysis of lattice results to investigate the dominance of the resonances over the correlators at each distance $|x|$. Figure 2.12 shows the decomposition of $R_V(x)$ into several contributions of different regions of s. "Perturbation" means the contribution of the spectral function in the region $s > 2.7$ GeV^2, which is calculated by using perturbation theory. In the region $s \leq 2.7$ GeV^2, we split the region of s into the resonance of the ρ meson $(m_\rho - 0.15 \text{ GeV})^2 < s < (m_\rho + 0.15 \text{ GeV})^2$, and above and below the resonance. From the figure, we find that the vector correlator is not dominated by the ρ meson in the region $x \lesssim 0.5$ fm, while the perturbative contribution occupies only 50% of the total at $x \simeq 0.5$ fm. We also show the same plot for the axial-vector channel in Fig. 2.13. The region of "Perturbation" is the same as for the vector channel $s > 2.7$ GeV^2, while the resonance of a_1 meson is chosen

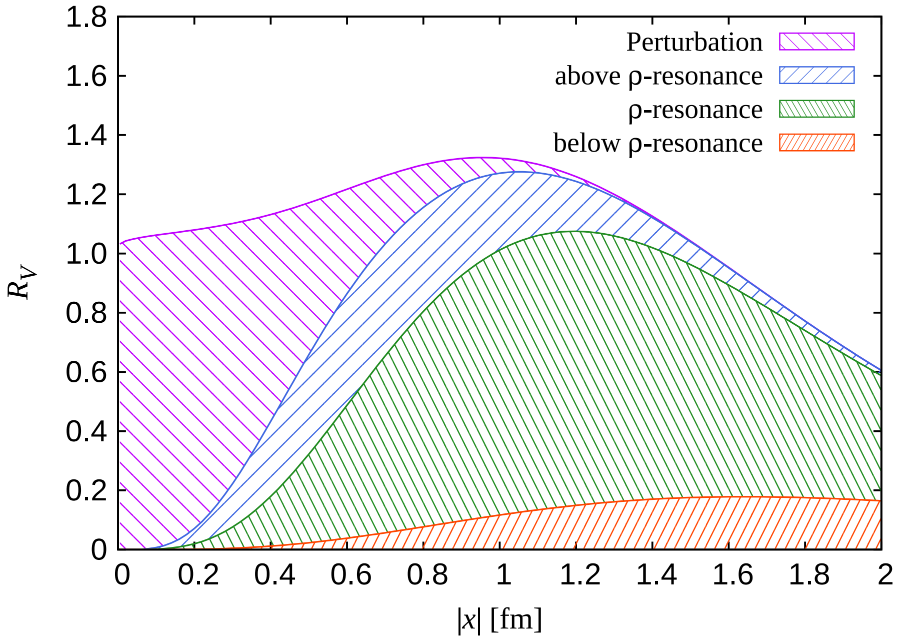

FIGURE 2.12: Decomposition of the contribution of the spectral function $\rho_V(s)$ to $R_V(x)$.

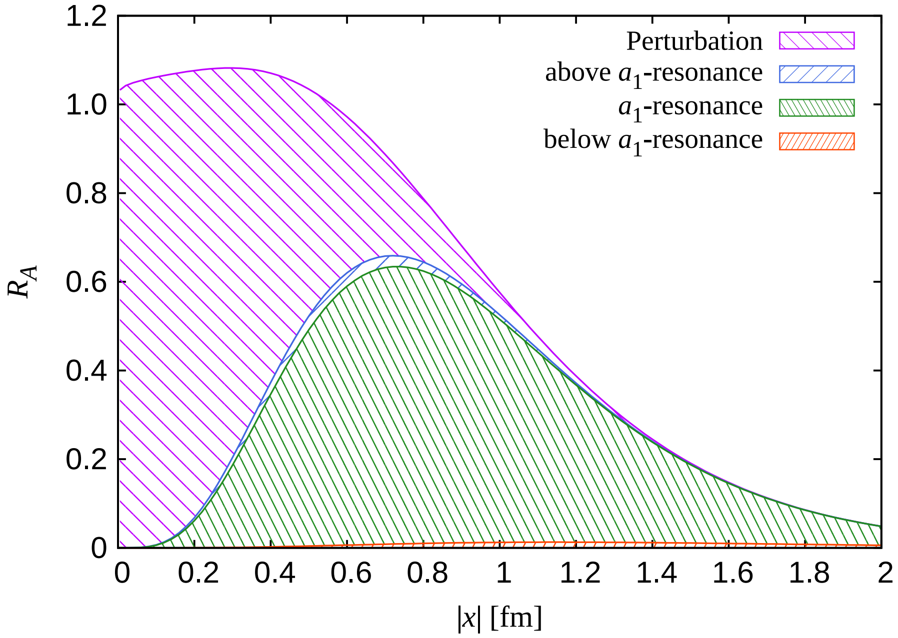

FIGURE 2.13: Decomposition of the contribution of the spectral function $\rho_A(s)$ to $R_A(x)$.

as $(m_{a_1} - 0.40\ \mathrm{GeV})^2 < s < (m_{a_1} + 0.40\ \mathrm{GeV})^2$. Both of these figures suggest that the non-perturbative contribution is very significant already at $|x| \sim 0.5$ fm. Around there, perturbation theory is not reliable and a non-perturbative technique is needed to investigate the correlators.

Chapter 3

Lattice calculation

3.1 Lattice correlators

On the lattice, rotational symmetry is broken to hypercubic symmetry and therefore scalar correlator at a lattice point is not necessarily equal to that at another point with the same x^2. For example, the scalar correlators at $(0, 0, 0, 2a)$ and (a, a, a, a) are different, while those in the continuum theory agree with each other. In this section, we classify the correlators on the lattice with respect to the hypercubic symmetry.

At first, we explain how to classify the correlators which are Lorentz scalar in the continuum theory. Since two-point correlators are always parity even, the pseudoscalar channel can be classified in the same manner as the scalar channel. The classification is done by the identity

$$\Pi_{S/P}(\mathcal{O}_4(x)) = \Pi_{S/P}(x), \tag{3.1}$$

where $\mathcal{O}_d$ stands for an arbitrary d-dimensional hypercubic transformation including $\det \mathcal{O}_d = -1$. Here a negative component $-x_\mu$, which needs to be introduced with the transformation $\mathcal{O}_d$, means $L_\mu - x_\mu$ in a finite box $L_1 \times L_2 \times L_3 \times L_4$ with the periodic or anti-periodic boundary condition. We find 322 independent separations in the region $1 \leq (x/a)^2 \leq 100$. Other scalar quantities such as the scalar-contracted vector and axial vector correlators $\Pi_{V/A}(x)$ are also classified in the same manner.

About the vector and axial-vector channels with the Lorentz indices, there are two types of Lorentz components for the classification. One is the Lorentz diagonal components $\Pi_{V/A,\mu\mu}(x)$, in which a lattice point is interpreted as a set of one special component x_μ with μ-direction and the other three dimensional coordinate $\bar{x}_{(\mu)}$ of other components,

$$\Pi_{V/A,\mu\mu}(x) = \Pi_{V/A,\mu\mu}(x_\mu; \bar{x}_{(\mu)}). \tag{3.2}$$

Then, the hypercubic symmetry guarantees

$$\Pi_{V/A,\mu\mu}(-x_\mu; \bar{x}_{(\mu)}) = \Pi_{V/A,\mu\mu}(x_\mu; \bar{x}_{(\mu)}), \tag{3.3a}$$

$$\Pi_{V/A,\mu\mu}(x_\mu; \mathcal{O}_3(\bar{x}_{(\mu)})) = \Pi_{V/A,\mu\mu}(x_\mu; \bar{x}_{(\mu)}), \tag{3.3b}$$

$$\Pi_{V/A,\mu'\mu'}(x_{\mu'}; \bar{x}_{(\mu')}) = \Pi_{V/A,\mu\mu}(x_\mu; \bar{x}_{(\mu)}) \quad \text{if } x_{\mu'} = x_\mu. \tag{3.3c}$$

Sorting the Lorentz diagonal components of the vector and axial-vector correlators by this relation, we obtain 968 independent separations in $1 \leq (x/a)^2 \leq 100$.

The Lorentz off-diagonal components, which belong to the other type of the classification, are similarly written as

$$\Pi_{V/A,\mu\bar{\mu}}(x) = \Pi_{V/A,\mu\bar{\mu}}(x_\mu, x_{\bar{\mu}}; \bar{x}_{(\mu,\bar{\mu})}), \tag{3.4}$$

where the two special components x_μ and $x_{\bar{\mu}}$ with μ- and $\bar{\mu}$-direction ($\mu \neq \bar{\mu}$) are distinguished from the other two components $\bar{x}_{(\mu,\bar{\mu})}$. Then the hypercubic symmetry yields the relations

$$\Pi_{V/A,\bar{\mu}\mu}(x_\mu, x_{\bar{\mu}}; \bar{x}_{(\mu,\bar{\mu})}) = \Pi_{V/A,\mu\bar{\mu}}(x_\mu, x_{\bar{\mu}}; \bar{x}_{(\mu,\bar{\mu})}), \tag{3.5a}$$

$$\Pi_{V/A,\mu\bar{\mu}}(x_{\bar{\mu}}, x_\mu; \bar{x}_{(\mu,\bar{\mu})}) = \Pi_{V/A,\mu\bar{\mu}}(x_\mu, x_{\bar{\mu}}; \bar{x}_{(\mu,\bar{\mu})}), \tag{3.5b}$$

$$\Pi_{V/A,\mu\bar{\mu}}(-x_\mu, x_{\bar{\mu}}; \bar{x}_{(\mu,\bar{\mu})}) = -\Pi_{V/A,\mu\bar{\mu}}(x_\mu, x_{\bar{\mu}}; \bar{x}_{(\mu,\bar{\mu})}), \tag{3.5c}$$

$$\Pi_{V/A,\mu\bar{\mu}}(x_\mu, x_{\bar{\mu}}; \mathcal{O}_2(\bar{x}_{(\mu,\bar{\mu})})) = \Pi_{V/A,\mu\bar{\mu}}(x_\mu, x_{\bar{\mu}}; \bar{x}_{(\mu,\bar{\mu})}), \tag{3.5d}$$

$$\Pi_{V/A,\mu'\bar{\mu}}(x_{\mu'}, x_{\bar{\mu}}; \bar{x}_{(\mu',\bar{\mu})}) = \Pi_{V/A,\mu\bar{\mu}}(x_\mu, x_{\bar{\mu}}; \bar{x}_{(\mu,\bar{\mu})}) \quad \text{if } x_{\mu'} = x_\mu. \tag{3.5e}$$

Although (3.5c) is a relation with sign flip, the correlators at the two points indicated by (3.5c) are still related and therefore not independent. Sorting by these relations, we obtain 1,318 separations in $1 \leq (x/a)^2 \leq 100$. The representatives of these equivalence classes are labeled by fixed directions $\mu = 1, \bar{\mu} = 2$ and coordinate parameters x_1, x_2 and x^2.

The above discussion is exact after the ensemble average. On a single gauge configuration, correlators do not satisfy the above identities. In the analysis, correlators at one gauge configuration is interpreted as the averages over all points in the same equivalence class.

We need to mention another lattice artifact due to the violation of the current conservation. Since we use local currents $\bar{u}(x)\Gamma d(x)$ to calculate the correlators, the vector current is not conserved, *i.e.*

$$\sum_\mu \partial_\mu \Pi^{\text{lat}}_{V,\mu\nu}(x) \neq 0, \tag{3.6}$$

for any simple derivatives on the lattice, resulting in a nontrivial renormalization factor $Z_V \neq 1$. Because of this, we need to determine the renormalization factors of the (axial-)vector current as well as the (pseudo)scalar density. The result of the renormalization is shown in Chapter 4.

3.2 Lattice action and ensembles

In this work, we perform lattice calculations on the gauge ensembles of $2+1$-flavor Möbius domain-wall fermions [40, 41] generated by JLQCD collaboration [42]. Möbius domain-wall fermion is a generalization of the domain-wall fermion [43,44], which has good chiral symmetry on the lattice. In addition, we employ the three-step stout link smearing [76] and the tree-level Symanzik improved gauge action [77, 78]. The detail of our lattice action is described in Appendix C.

TABLE 3.1: Lattice ensembles used in this work.

β	a [fm]	$N_s^3 \times N_t \times L_s$	am_s	am_q	am_{res}	aM_π	N_{conf}	N_{src}
4.17	0.0804	$32^3 \times 64 \times 12$	0.0300	0.0070	0.00017(1)	0.1263(4)	200	4
				0.0120	0.00015(2)	0.1618(3)	200	2
				0.0190	0.00015(3)	0.2030(3)	200	2
		$48^3 \times 96 \times 12$	0.0400	0.0035	0.00022(2)	0.0921(1)	200	2
		$32^3 \times 64 \times 12$		0.0070	0.00023(4)	0.1260(4)	200	4
				0.0120	0.00012(8)	0.1627(3)	200	2
				0.0190	0.00015(3)	0.2033(3)	200	2
4.35	0.0547	$48^3 \times 96 \times 8$	0.0180	0.0042	$\sim 10^{-5}$	0.0820(3)	200	2
				0.0080		0.1127(3)	200	1
				0.0120		0.1381(3)	200	1
			0.0250	0.0042		0.0831(4)	200	2
				0.0080		0.1130(3)	200	1
				0.0120		0.1387(3)	200	1
4.47	0.0439	$64^3 \times 128 \times 8$	0.0150	0.0030		0.0632(2)	200	1

Table 3.1 summarizes the ensembles. The input strange quark mass m_s is only for a sea quark, while the mass m_q of the two degenerate quarks, up and down, is used for both the valence and sea quarks. The computed pion masses M_π are in the region 230–500 MeV. The lattice cutoffs $a = $ 0.044–0.080 fm, which are determined though the Wilson-flow scale [79], are the state-of-the-art for simulations with the Ginsparg-Wilson fermions. The residual mass m_{res} is controlled to O(1 MeV) on our coarsest lattice and mostly negligible for the finer lattices. The volumes $N_s^3 \times N_t = (L/a)^3 \times (T/a)$ are chosen such that $M_\pi L$ is not smaller than 4 to avoid the finite volume effects [80]. For each ensemble, $N_{\mathrm{conf}} = 200$ configurations are sampled from 10,000 molecular dynamics time. For each configuration, we calculate the correlators from one or more (N_{src}) source points. We use the IroIro++ simulation code [81] for these calculations.

3.3 Reduction of discretization effect

Figure 3.1 shows the pseudoscalar correlator $\Pi_P^{\mathrm{lat}}(x)$ calculated non-perturbatively on the ensemble at $\beta = 4.35$, $(am_q, am_s) = (0.0042, 0.0180)$. This figure also shows the mean field approximation $\Pi_P^{\mathrm{lat,mean}}(x)$ of the pseudoscalar correlator on the lattice and its asymptotic form $\Pi_P^{\mathrm{asym,mean}}(x)$ in the long-distance limit. The mean field approximation on the lattice is calculated by a contraction of the propagators of the domain-wall fermions in the mean field theory and its long-distance limit is calculated by applying Taylor expansion about the momentum $aq_\mu = 0$. (see Appendix D for more detail).

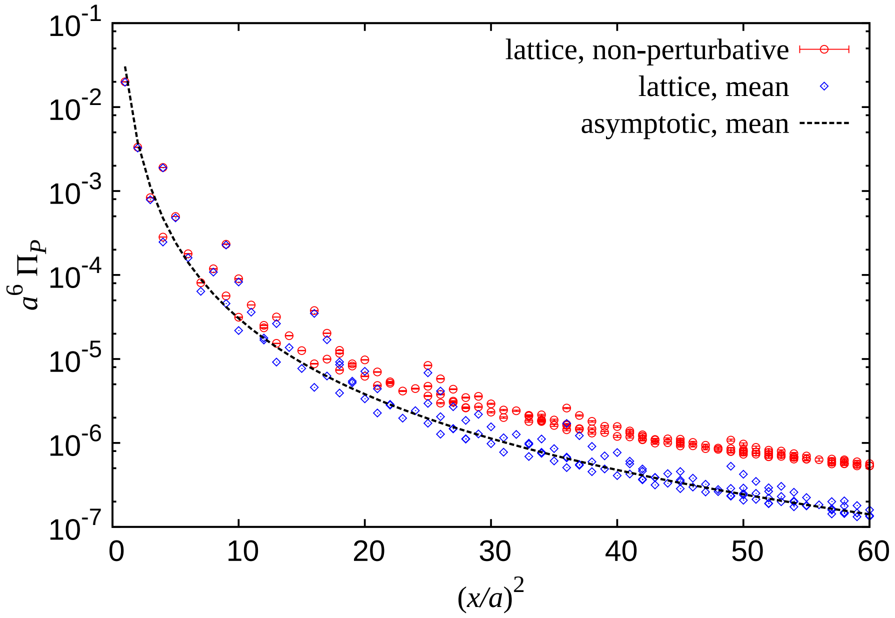

FIGURE 3.1: Pseudoscalar correlator obtained by the lattice calculation (circles) and its mean field approximation (diamonds) at the same valence mass. The dashed curve represents the asymptotic behavior of the mean field approximation. The lattice data on the $48^3 \times 96$ at $\beta = 4.35$ and $(am_q, am_s) = (0.0042, 0.0180)$ are plotted as a representative.

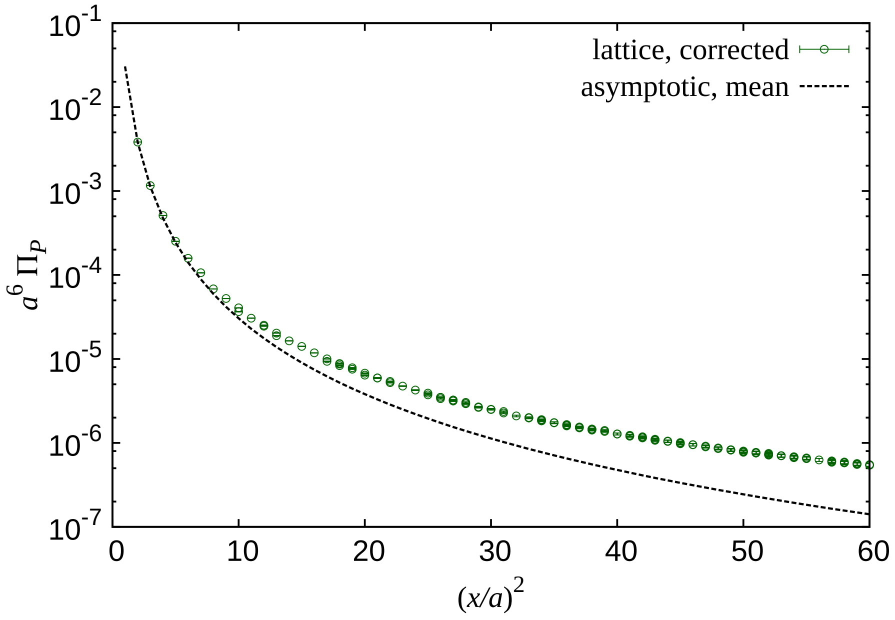

FIGURE 3.2: Pseudoscalar correlator after applying the subtraction (3.7). The result on the same ensemble as in Fig. 3.1 is shown.

The non-perturbative lattice data are not on a smooth curve due to discretization effects. A similar discretization effect as seen in the free theory as well as in the mean field approximation describes the bulk of the discretization effects. We therefore improve the lattice data by a subtraction,

$$\Pi_\Gamma^{\rm lat}(x) \to \Pi_\Gamma^{\rm lat}(x) - \left(\Pi_\Gamma^{\rm lat,mean}(x) - \Pi_\Gamma^{\rm asym,mean}(x)\right). \tag{3.7}$$

As seen in Fig. 3.2, which shows the pseudoscalar correlator after this subtraction, we obtain much smoother correlators.

Figures 3.3 and 3.4 show the pseudoscalar and vector correlators, respectively, after applying the subtraction (3.7). They are normalized by the continuum free correlator $\Pi_{P/V}^{\rm cont,free}(x)$ in the chiral limit and plotted in a linear scale. Here, we introduce a parameter θ, which is defined as an angle between the four-dimensional point x and the direction $(1,1,1,1)$. In four-dimension, we can choose the representatives of equivalent lattice points with respect to hypercubic symmetry, which is discussed in Section 3.1, to satisfy $\theta \leq 60^\circ$. This parameter is strongly correlated with the discretization effects as discussed in [31,37], *i.e.* the discretization effects increase as θ increases. This tendency is observed even after applying the subtraction (3.7).

As seen in Fig. 3.5, which is a magnification of Fig. 3.4 in the range $0^\circ \leq \theta \leq 30^\circ$, there are discretization effects visible already at $\theta = 30^\circ$. Although the points (0,3,3,3) and (1,1,3,4)[1] are both at $(x/a)^2 = 27$ and $\theta = 30^\circ$, the values disagree beyond the statistical error. The same is observed for the data at (0,4,4,4) and (2,2,2,6) sharing $(x/a)^2 = 48$ and $\theta = 30^\circ$. The similar situation occurs more frequently for $\theta > 30^\circ$. Namely, the data in the region $\theta \geq 30^\circ$ cannot be simply parametrized by any functions of θ, and we therefore omit them in the analysis. Figure 3.5 also indicates that the lattice data at $\theta < 30^\circ$ may slightly depend on θ. For the determination of the renormalization factor in the next section, we separately treat the discretization effects of the data of $\theta < 20^\circ$ and of $\theta \geq 20^\circ$.

In the rest of this section, we give some comments on the tree-level corrections. In the previous studies [36,37], the tree-level correction was done multiplicatively instead of the additive (3.7), *i.e.* they performed the tree-level correction by multiplying the lattice correlator $\Pi_\Gamma^{\rm lat}(x)$ by $\Pi_\Gamma^{\rm cont,free}(x)/\Pi_\Gamma^{\rm lat,free}(x)$. However, the additive correction must be better to reduce the discretization effect at tree-level since the discretization effects at short distances can be described as a perturbative series of the discretization effects. In fact, we observe that the additive correction is better, from the comparison between the results of the additive correction shown in Figs. 3.3 and 3.4 and the multiplicative correction, which is shown in Fig. 3.6.

Furthermore, the additive tree-level correction is improved by the mean field improvement. The normalization of the lattice correlators at tree-level $\Pi_\Gamma^{\rm lat,free}(x)$ is different from that in full QCD $\Pi_\Gamma^{\rm lat}(x)$ because of the contribution of the tadpole diagrams [82]. Although this tree-level correction in this work does not lead to an apparent problem because the stout link smearing reduces the tadpole effects, the difference of the normalization becomes large as simulation is done with strong coupling (small β) region or without the smearing.

---

[1] Here, we indicate lattice points in lattice unit for simplicity.

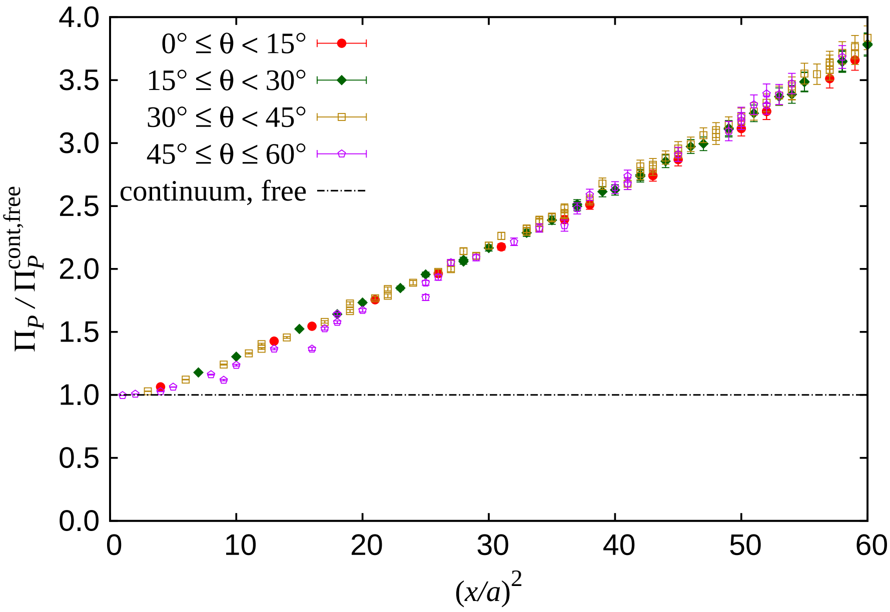

FIGURE 3.3: Pseudoscalar correlator divided by the tree-level continuum correlator after applying the subtraction (3.7). The data in $0^\circ \leq \theta < 15^\circ$ (circles), $15^\circ \leq \theta < 30^\circ$ (diamonds), $30^\circ \leq \theta < 45^\circ$ (squares), and $45^\circ \leq \theta \leq 60^\circ$ (pentagons) are separately plotted. The result on the same ensemble as in Fig. 3.1 is shown.

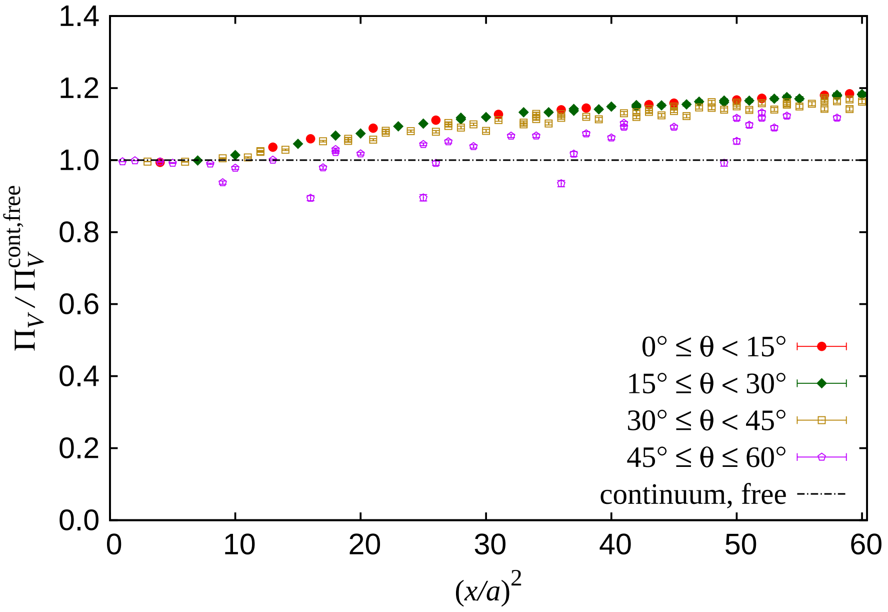

FIGURE 3.4: Same as Fig. 3.3 but for the vector channel.

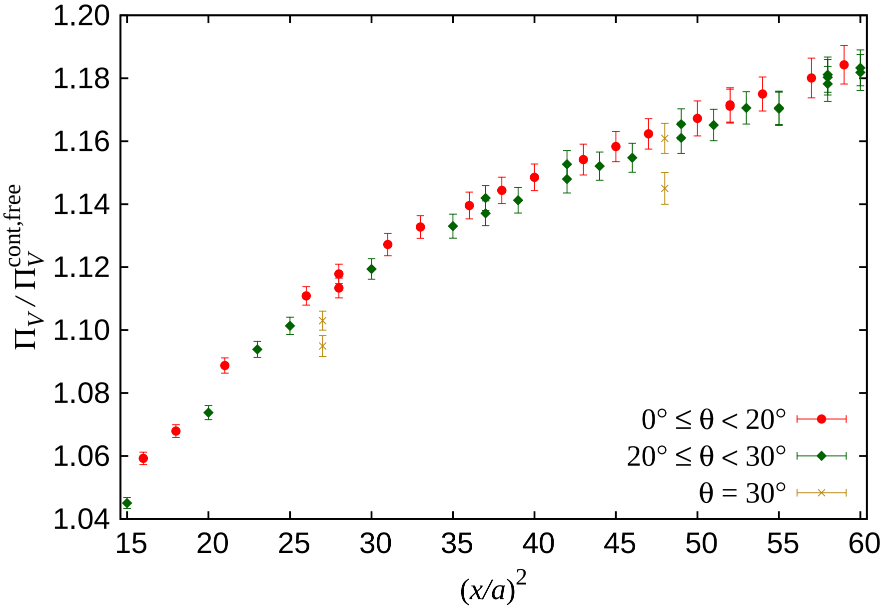

FIGURE 3.5: Detailed view of Fig. 3.4. The Data in $0° \leq \theta < 20°$ (circles), $20° \leq \theta < 30°$ (diamonds), and at $\theta = 30°$ (crosses) are separately plotted. Data at $\theta > 30°$ are omitted.

3.4 Subtraction of finite volume effect

From the viewpoint of chiral perturbation theory (ChPT) in the p-regime [80], the finite volume effects on the pion mass and the decay constants are mostly suppressed when $M_\pi L \gtrsim 4$ because the finite volume effects on these quantities start occurring at the loop correction of ChPT, whose first order is mostly negligible when $M_\pi L \gtrsim 4$. On the other hand, point-to-point correlators contain finite volume effect at the tree-level, which relates correlators $\Pi_\Gamma^{L^3\times T}(x)$ in a finite volume ($M_\pi L, M_\pi T \gtrsim 4$) with periodic boundaries to those $\Pi_\Gamma^\infty(x)$ in the infinite volume as

$$\Pi_\Gamma^{L^3\times T}(x) = \Pi_\Gamma^\infty(x) + \sum_{x_0} \Pi_\Gamma^\infty(x - x_0), \tag{3.8}$$

where the sum over x_0 runs over

$$x_0 \in \{(\pm L, 0, 0, 0), (0, \pm L, 0, 0), (0, 0, \pm L, 0), (0, 0, 0, \pm T), (\pm L, \pm L, 0, 0), \cdots\}. \tag{3.9}$$

Since the pseudoscalar correlator is expected to contain large finite volume effects due to the pion pole, we focus on the pseudoscalar channel.

Note that the three-dimensional space integral of (3.8)

$$\int d^3x\, \Pi_P^{L^3\times T}(\vec{x}, t) = \int d^3x\, \Pi_P^\infty(\vec{x}, t) + \sum_{n_{t_0}=\pm 1}^{\pm\infty} \int d^3x\, \Pi_P^\infty(\vec{x}, t - n_{t_0} T). \tag{3.10}$$

is independent of the finite size L, Since the second term on the RHS is negligible except for the

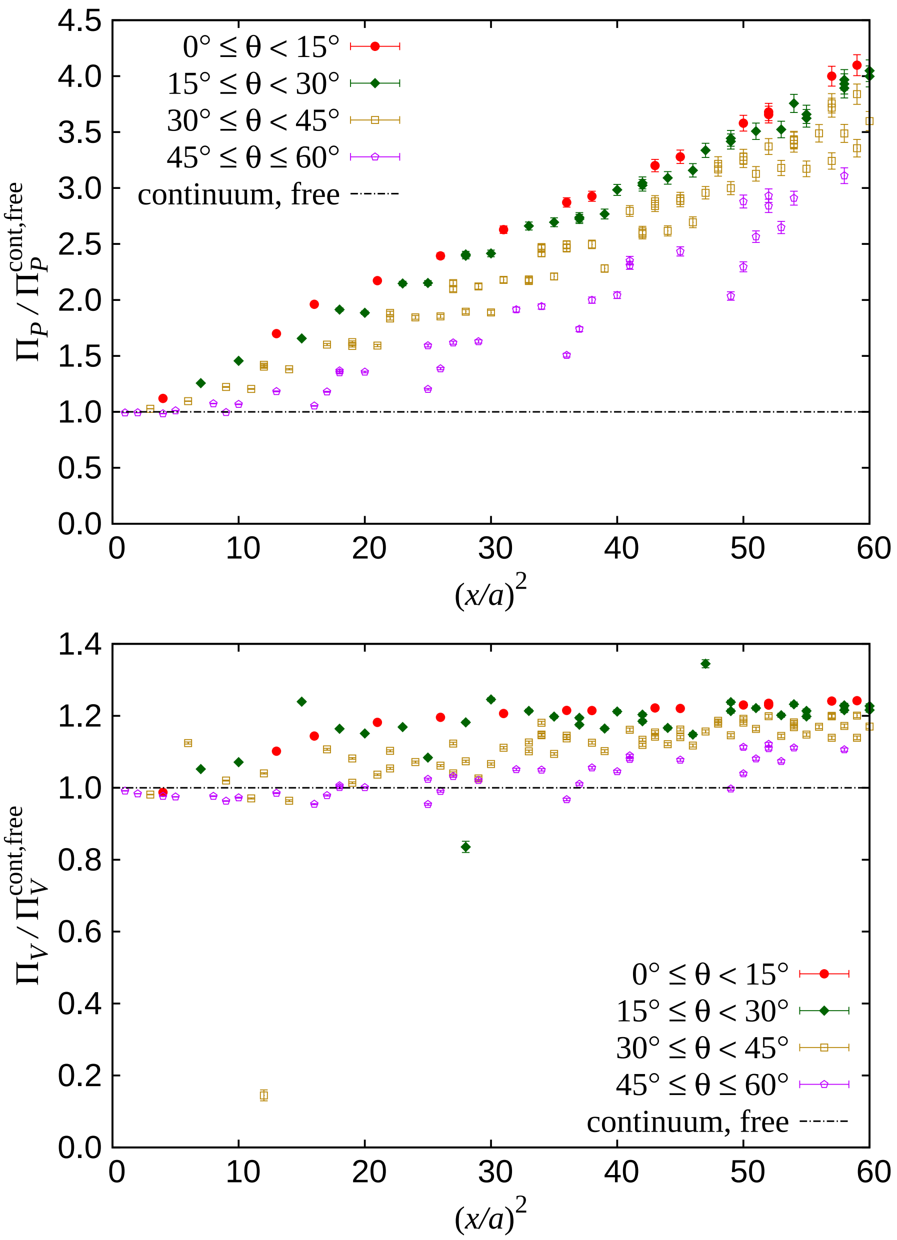

FIGURE 3.6: Pseudoscalar (left) and vector (right) correlators divided by the tree level continuum correlator after applying the tree level correction by the multiplicative manner. The data in $0^\circ \leq \theta < 15^\circ$ (circles), $15^\circ \leq \theta < 30^\circ$ (diamonds), $30^\circ \leq \theta < 45^\circ$ (squares), and $45^\circ \leq \theta \leq 60^\circ$ (pentagons) are separately plotted. The result on the same ensemble as in Fig. 3.1 is shown.

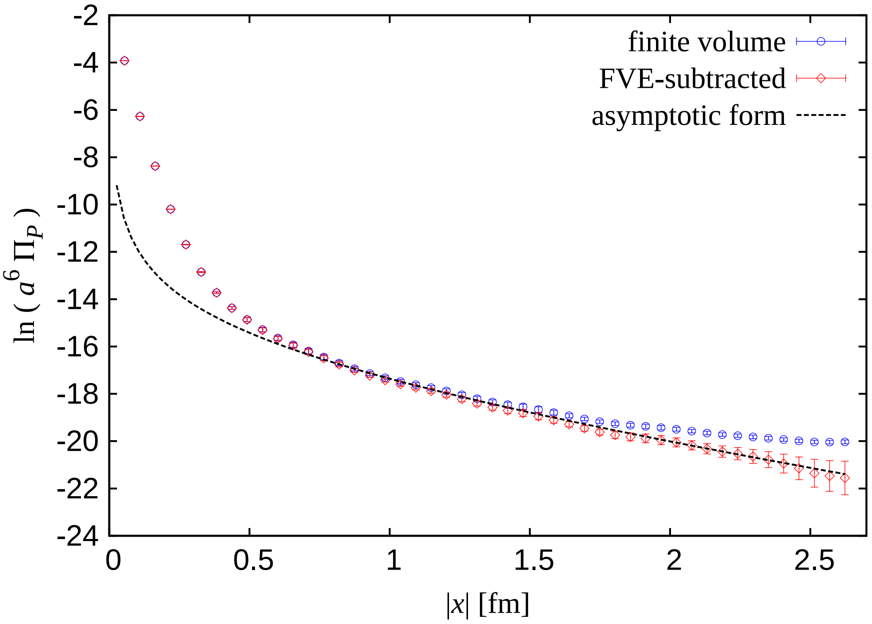

FIGURE 3.7: Point-to-point correlator of the pseudoscalar channel in the time-direction ($|x| = t$) before (diamonds) and after (circles) applying the subtraction (3.13) of the finite volume effects. Dashed curve corresponds to the asymptotic form (3.12), whose z_0 and M_π are determined from the zero momentum correlator. Data on the same ensemble as in Fig. 3.1 are plotted.

contribution of $n_{t_0} = 1$, the parameters M_π, z_0 in the long-distance behavior of $\int \mathrm{d}^3x \Pi_P^\infty(\vec{x}, t) \to z_0 \mathrm{e}^{-M_\pi t}$ are appropriately extracted from the finite volume data $\Pi_P^{L^3\times T}(x)$ using the fit function

$$\int \mathrm{d}^3x\, \Pi_P^{L^3\times T}(\vec{x}, t) \xrightarrow{t, T-t \gtrsim 1/\Lambda_{\mathrm{QCD}}} z_0(\mathrm{e}^{-M_\pi t} + \mathrm{e}^{-M_\pi (T-t)}). \tag{3.11}$$

These parameters are also related to the long-distance point-to-point correlator $\Pi_P^\infty(x)$ in the infinite volume,

$$\Pi_P^\infty(x) \xrightarrow{|x| \gtrsim 1/\Lambda_{\mathrm{QCD}}} \frac{z_0 M_\pi^2}{2\pi^2} \frac{K_1(M_\pi |x|)}{|x|}, \tag{3.12}$$

where K_1 stands for the modified Bessel function. Inserting this into (3.8), we obtain the relation to subtract the finite volume effects

$$\Pi_P^\infty(x) = \Pi_P^{L^3\times T}(x) - \frac{z_0 M_\pi^2}{2\pi^2} \sum_{x_0} \frac{K_1(M_\pi |x - x_0|)}{|x - x_0|}, \tag{3.13}$$

which is calculated by using M_π and z_0 extracted from the asymptotic form of the zero-momentum correlator.

Figure 3.7 shows the point-to-point correlator of the pseudoscalar channel before (diamond) and after (circle) applying the subtraction (3.13) of the finite volume effects, calculated on the ensemble at $\beta = 4.35, am_q = 0.0042, am_s = 0.0180$. Correlators only on the time axis $(\vec{0}, t(= |x|))$ is plotted. Dashed curve corresponds to the asymptotic form (3.12) of the pseudoscalar correlator, whose z_0 and M_π is determined from the zero momentum correlator (3.10). The correlator

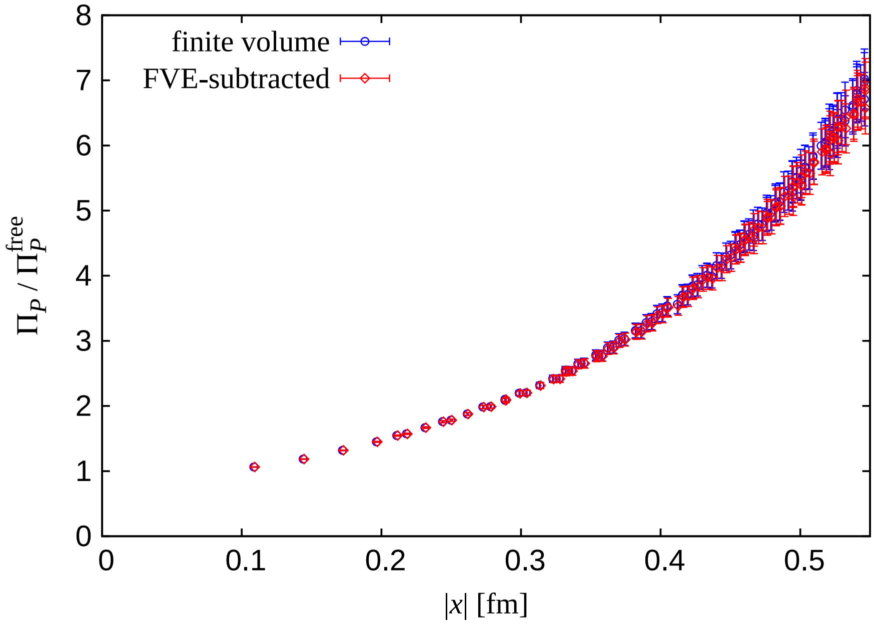

FIGURE 3.8: Point-to-point correlator of the pseudoscalar channel before (diamond) and after (circle) applying the subtraction (3.13). Data on the same ensemble as in Fig. 3.1 are plotted.

after applying the subtraction (3.13) coincides with the asymptotic form at long distances.

From Fig. 3.7, we find that the finite volume effects are significant at $x \gtrsim 1$ fm. In Fig. 3.8, we compare $\Pi_P(x)/\Pi_P^{\text{free}}(x)$ before and after the subtraction (3.13) in the short distances $x \lesssim 0.5$ fm and find that the magnitude of the finite volume effect in the pseudoscalar correlator at the short distances is less than 20% of the statistical errors. Since the finite volume effects are already small in the pseudoscalar correlator, those in other channels are expected to be negligible. In this work, we apply the subtraction (3.13) only for the pseudoscalar channel.

In Chapter 5, we investigate the difference between the vector and axial-vector correlators, which does not include the dominant contribution from perturbation theory. Therefore the difference may be more sensitive to the wrapping-around effects of the pion. The finite volume effect on the axial-vector correlator $\Pi_A(x)$ is estimated as follows.

At long distances, the contribution of the transversal component is suppressed and therefore the axial-vector correlator is approximated as

$$\Pi_A(x) \to \int \frac{\mathrm{d}^4 q}{(2\pi)^4} \mathrm{e}^{\mathrm{i}qx} q^2 \widetilde{\Pi}_A^{(0)}(-q^2). \tag{3.14}$$

This asymptotic form is related to the zero-momentum correlator by

$$\int \mathrm{d}^3x\, \Pi_{A,44}(t,\vec{x}) = \int \mathrm{d}^3x \int \frac{\mathrm{d}^4 q}{(2\pi)^4} \mathrm{e}^{-\mathrm{i}qx} q^2 \widetilde{\Pi}_A^{(0)}(-q^2). \tag{3.15}$$

Therefore, we can similarly estimate the long-distance behavior of $\Pi_A^\infty(x)$ in the infinite box as

$$\Pi_A^\infty(x) \to \frac{M_\pi^2 z_0^A}{2\pi^2}\frac{K_1(M_\pi|x|)}{|x|}, \tag{3.16}$$

where z_0^A and M_π are obtained by the fit for the zero-momentum correlator at large t,

$$\int \mathrm{d}^3x \Pi_{A,44}^{L^3\times T}(\vec{x},t) \xrightarrow{t,T-t\gtrsim 1/\Lambda_{\mathrm{QCD}}} z_0^A(\mathrm{e}^{-M_\pi t} + \mathrm{e}^{-M_\pi(T-t)}). \tag{3.17}$$

Chapter 4

Non-perturbative renormalization of quark currents

4.1 Renormalization of composite operators on the lattice

Green's functions involving some composite operators may contain divergent terms even if the fundamental fields, their masses, and coupling constants are already renormalized. Renormalization of composite operators is therefore needed for the calculation of a scheme-dependent quantities containing composite operators, such as the matrix elements of the weak effective Hamiltonian. See the review [83] for more explanations of lattice calculations.

The renormalization of a composite operator $O(x)$ is done multiplicatively,

$$O^R(\mu; x) = Z^R(\mu) O^0(x), \tag{4.1}$$

where the superscripts R and 0 stand for the renormalization scheme and a symbol to indicate unrenormalized operators, respectively, and Z^R is the renormalization factor at the scale μ in the scheme R, which is conventionally chosen to the $\overline{\mathrm{MS}}$ scheme. The situation is usually more complicated due to the operator mixing, *i.e.* (4.1) should be generalized to

$$O_i^R(\mu; x) = \sum_j Z_{ij}^R(\mu) O_j^0(x), \tag{4.2}$$

with possible mixed operators $O_i(x)$, all of which may couple to the same state.

In this work, we renormalize the quark bilinear operators on the lattice. Since quark bilinears composed of Ginsparg-Wilson fermions do not suffer from operator mixings, we can assume the renormalization can be implemented in a simple manner (4.1). The vector (and axial-vector) current in the continuum is the simplest because they are not renormalized in virtue of the current conservation low. On the lattice, the local vector current, $V_\mu(x) = \bar{u}(x)\gamma_\mu d(x)$, used in this work is not conserved and therefore a finite renormalization to match the continuum is necessary. Scale-dependent operators such as the scalar and pseudoscalar currents diverge in the continuum limit (or the limit of a regularization parameter) and their renormalization is always necessary. Precise chiral symmetry of the domain-wall fermion ensures the equality of the renormalization factors of the scalar and pseudoscalar densities, or that of the vector and axial-vector currents.

There are several ways to renormalize composite operators. One is based on lattice perturbation theory, which is reviewed in [84]. Perturbative calculation on the lattice is very complicated and increasing the loop order is difficult. Therefore, it is difficult to renormalize precisely by using the lattice perturbation theory. Non-perturbative methods are also applied. One is the application of Ward-Takahashi identities, [85, 86] which can determine renormalization constants very precisely. Although the Ward-Takahashi identities are applicable for limited channels, it is useful for a consistency check of the renormalization by other methods.

One widely used method for non-perturbative renormalization is the use of the Schrödinger functional [87, 88], which is defined with the Dirichlet boundary condition in the time direction. It defines the Schrödinger functional renormalization scheme [89]. This method provides a gauge invariant renormalization and very precise results by combining with the step scaling procedure [90]. A disadvantage of this method is a large computational cost compared to other approaches. The Schrödinger functional for the Möbius domain-wall fermion, which is used in this work, is recently formulated [91] as a generalization of that for the domain-wall fermion [92]. See the review [93] for more detail.

There is another widely used renormalization method through the Regularization Independent Momentum Subtraction (RI/MOM) scheme [94], which is also called the Rome Southampton method. In this method, the renormalization condition is imposed on the vertex function involving the composite operator of interest with external quarks at a certain momentum. The machine cost of this method is relatively cheap and a lot of groups have applied it. There are some disadvantage of this method, the necessity of a gauge fixing and the presence of the window problem. The latter requires the renormalization point μ_{mom} to be in the window $\Lambda_{\mathrm{QCD}} \ll \mu_{\mathrm{mom}} \ll \pi/a$ in order to avoid both the discretization effect and the large uncertainty of the perturbative matching.

In this work, we use another renormalization procedure, *so called X-space method*, which is firstly suggested by [35] and applied in [36, 37]. The renormalization condition in this method is similar to that in the RI/MOM, but is imposed on current correlators. There are some advantages, *i.e.* the method provides fully gauge invariant renormalization procedure and is free from the contact terms. Therefore, this method prevents mixing with certain types of operators and is suitable for the renormalization of weak matrix elements, which is necessary for *e.g.* $K \to \pi\pi$ decays. For the iso-vector (pseudo)scalar and (axial-)vector bilinear operators, The perturbative matching in this method is available to the four-loop level [38]. The disadvantage of this method is the window problem as seen in the RI/MOM method. In this work, we carefully take into account this point by utilizing the OPE which is discussed in Section 2.4.

4.2 Renormalization by X-space method

We renormalize the quark bilinear operators on the lattice to those in the $\overline{\mathrm{MS}}$ scheme at a renormalization scale, which is often set to 2 or 3 GeV. Neglecting the operator mixing, the renormalization is multiplicative, *i.e.*

$$O_\Gamma^{\overline{\mathrm{MS}}}(2\ \mathrm{GeV}; x) = Z_\Gamma^{\overline{\mathrm{MS}}/\mathrm{lat}}(2\ \mathrm{GeV}, a) O_\Gamma^{\mathrm{lat}}(a; x), \tag{4.3}$$

where $\Gamma \in \{S, P, V, A\}$, $O_\Gamma \in \{S, P, V_\mu, A_\mu\}$, and $Z_\Gamma^{\overline{\mathrm{MS}}/\mathrm{lat}}(2\ \mathrm{GeV}, a)$ is the renormalization constant.

The renormalization condition in the X-space method is imposed by requiring

$$\left(\widetilde{Z}_\Gamma^{\overline{\mathrm{MS}}/\mathrm{lat}}(2\ \mathrm{GeV}, a; x)\right)^2 \Pi_\Gamma^{\mathrm{lat}}(a; x) = \Pi_\Gamma^{\overline{\mathrm{MS}}}(2\ \mathrm{GeV}; x), \tag{4.4}$$

or equivalently,

$$\widetilde{Z}_\Gamma^{\overline{\mathrm{MS}}/\mathrm{lat}}(2\ \mathrm{GeV}, a; x) = \sqrt{\frac{\Pi_\Gamma^{\overline{\mathrm{MS}}}(2\ \mathrm{GeV}; x)}{\Pi_\Gamma^{\mathrm{lat}}(a; x)}}, \tag{4.5}$$

at a finite distance x.

Note that $\widetilde{Z}_\Gamma^{\overline{\mathrm{MS}}/\mathrm{lat}}(2\ \mathrm{GeV}, a; x)$ still contains some dependence on x. It originates from some errors arising in the continuum $\Pi_\Gamma^{\overline{\mathrm{MS}}}(2\ \mathrm{GeV}; x)$ and lattice $\Pi_\Gamma^{\mathrm{lat}}(a; x)$ correlators. The continuum one suffers from the truncation of the perturbative expansion as we discussed in Section 2.2. On the other hand, the lattice correlator contains discretization effects. In addition, the x-dependence of $\widetilde{Z}_\Gamma^{\overline{\mathrm{MS}}/\mathrm{lat}}(2\ \mathrm{GeV}, a; x)$ is also caused by non-perturbative effects at large $|x|$ in full QCD, which are not encoded in $\Pi_\Gamma^{\overline{\mathrm{MS}}}(2\ \mathrm{GeV}; x)$ in perturbation theory. In order to extract the renormalization constant, which must be independent of x, the distance $|x|$ of correlators should be chosen in a window $a \ll |x| \ll 1/\Lambda_{\mathrm{QCD}}$ to suppress these possible errors. In the following subsections, the systematic effects arising in $\widetilde{Z}_\Gamma^{\overline{\mathrm{MS}}}(2\ \mathrm{GeV}, a; x)$ are discussed in more detail and the renormalization factors are determined.

4.3 Determination of Z_V

With domain-wall fermions that precisely satisfy the Ginsparg-Wilson relation, the identity $Z_V^{\overline{\mathrm{MS}}/\mathrm{lat}}(a) = Z_A^{\overline{\mathrm{MS}}/\mathrm{lat}}(a)$ is valid. In the analysis of $Z_V^{\overline{\mathrm{MS}}/\mathrm{lat}}(a)$, the renormalization scale 2 GeV can be omitted because the current conservation ensures its scale independence.

Figure 4.1 shows x-dependence of $\widetilde{Z}_V^{\overline{\mathrm{MS}}/\mathrm{lat}}(a; x)$ and $\widetilde{Z}_A^{\overline{\mathrm{MS}}/\mathrm{lat}}(a; x)$, which are defined by (4.5), at three input masses and $\beta = 4.35, am_s = 0.0180$. For $|x| < 0.2$ fm, the results increase toward the short-distance regime due to the remnant discretization effects as discussed later. For $|x| > 0.25$ fm, there is a significant splitting between the vector and axial-vector channels due to the non-perturbative effects.

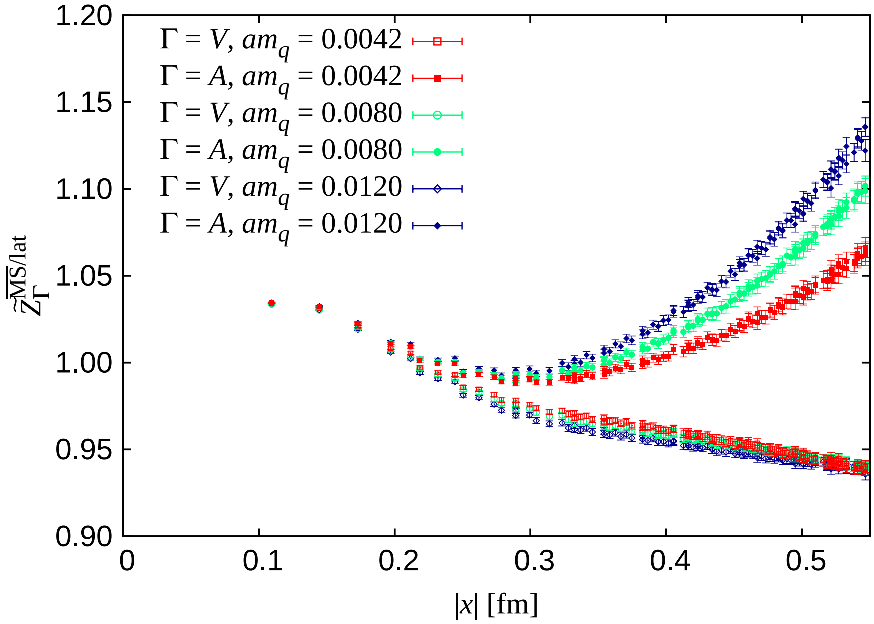

FIGURE 4.1: $\widetilde{Z}_V^{\overline{\rm MS}/{\rm lat}}(a;x)$ (open points) and $\widetilde{Z}_A^{\overline{\rm MS}/{\rm lat}}(a;x)$ (filled points) calculated by (4.5) at the three input masses $am_q = 0.0042$ (squares), 0.080 (circles), 0.0120 (diamonds) and $\beta = 4.35, am_s = 0.0180$.

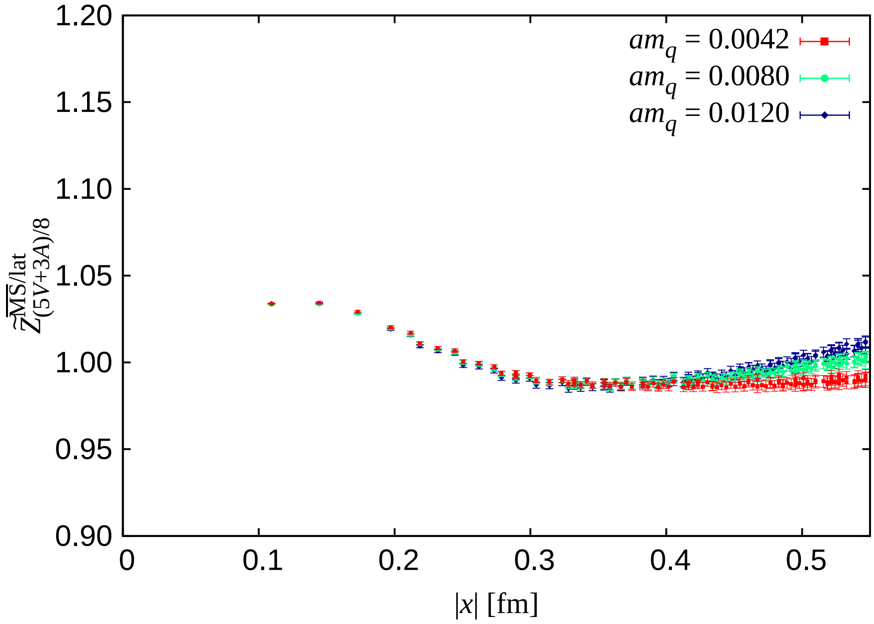

FIGURE 4.2: $\widetilde{Z}_{(5V+3A)/8}^{\overline{\rm MS}/{\rm lat}}(a;x)$ defined by (4.7). The results on the same ensembles as in Fig. 4.1 are shown.

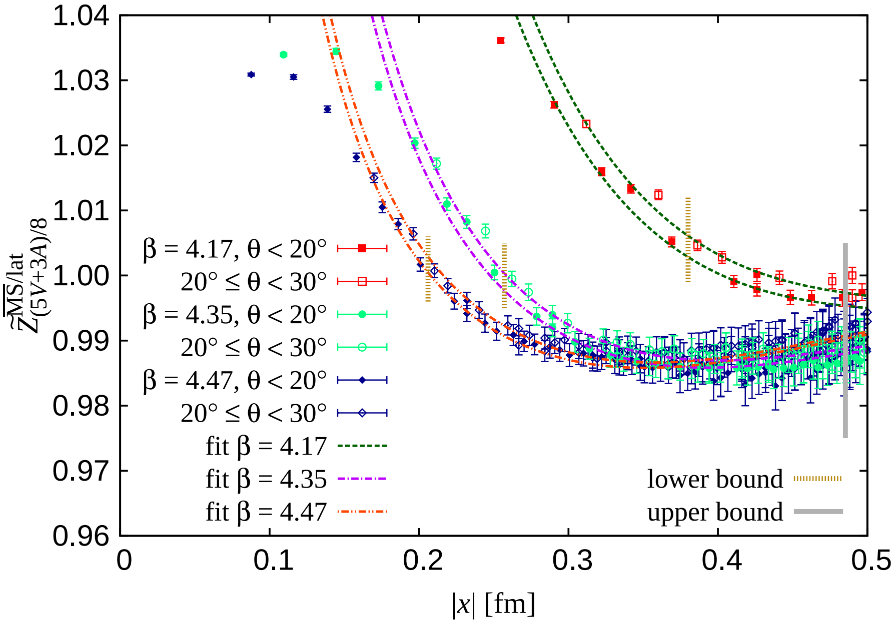

FIGURE 4.3: $\widetilde{Z}^{\overline{\rm MS}/{\rm lat}}_{(5V+3A)/8}(a;x)$ at the three of β with $M_\pi \sim 300$ MeV. For each β, the results at smaller am_s is plotted. The data at $\theta < 20°$ (filled points) and $20° \leq \theta < 30°$ (open points) are separately plotted. The fit results for both $\theta < 20°$ and $20° \leq \theta < 30°$ are also plotted by the curves.

The leading non-perturbative effect is described by OPE. According to the discussion in Section 2.4, the coefficients $c^V_{4,\bar{q}q}$ and $c^A_{4,\bar{q}q}$ in the OPE of the vector and axial-vector correlators,

$$\Pi_{V/A}(x) = \frac{c_0}{x^6} + \frac{c^{V/A}_{4,\bar{q}q} m_q \langle \bar{q}q \rangle + c^{V/A}_{4,G} \langle GG \rangle}{x^2} + \cdots , \tag{4.6}$$

satisfy $c^V_{4,\bar{q}q}/c^A_{4,\bar{q}q} = -3/5$ at tree level. The combination $\frac{1}{8}(5\Pi_V + 3\Pi_A)$ is therefore expected to cancel the leading contribution of the chiral condensate. Therefore we analyze

$$\widetilde{Z}^{\overline{\rm MS}/{\rm lat}}_{(5V+3A)/8}(a;x) = \sqrt{\frac{\Pi^{\overline{\rm MS}}_V(a;x)}{\frac{1}{8}\left(5\Pi^{\rm lat}_V(a;x) + 3\Pi^{\rm lat}_A(a;x)\right)}}, \tag{4.7}$$

to extract the renormalization constant suppressing the non-perturbative effect. We find that both the $|x|$-dependence and the mass dependence are dramatically reduced as shown in Fig. 4.2. Although there is no mass dependence remaining for $\widetilde{Z}^{\overline{\rm MS}/{\rm lat}}_{(3V+5A)/8}(a;x)$ in the OPE for the operators of dimension four, the data still have sizable mass dependence for $|x| > 0.4$ fm. This mass dependence may originate from higher dimensional operators including $m_q^2\langle GG\rangle$ and $m_q^3\langle\bar{q}q\rangle$. Another mass-independent operator $\langle\bar{q}q\bar{q}q\rangle$ with the same mass dimension should also be considered.

Figure 4.3 shows $\widetilde{Z}^{\overline{\rm MS}/{\rm lat}}_{(5V+3A)/8}(a;x)$ obtained at three β values with approximately matched quark masses. The position where $\widetilde{Z}^{\overline{\rm MS}/{\rm lat}}_{(5V+3A)/8}(a;x)$ starts deviating from a constant toward short distances moves as the lattice spacing is reduced, indicating that this deviation is due to the discretization effects. The most significant discretization effect is of $O(a^2)$ which appears as $(a/x)^2$. Since we already subtract discretization effects at the tree-level, $\alpha_s(\beta)(a/x)^2$ is the leading remaining discretization effects. As discussed in Section 3.3, we discard the data in $\theta \geq 30°$ and parametrize the discretization effects in $0° \leq \theta < 20°$ and in $20° \leq \theta < 30°$ separately as described below.

We determine $Z_V^{\overline{\mathrm{MS}}/\mathrm{lat}}$ by a simultaneous fit of the data on all ensembles using the fit function

$$\widetilde{Z}^{\overline{\mathrm{MS}}/\mathrm{lat}}_{(5V+3A)/8}(a;x) = Z_V^{\overline{\mathrm{MS}}/\mathrm{lat}}(\beta) + C_{-2}(\theta)\alpha_s(\beta)(a/x)^2 + C_{4,G}x^4 + (C_{6,q} + C_{6,mG}m_q^2 + C_{6,mq}m_q^3)x^6, \tag{4.8}$$

with nine free parameters $Z_V^{\overline{\mathrm{MS}}/\mathrm{lat}}(4.17)$, $Z_V^{\overline{\mathrm{MS}}/\mathrm{lat}}(4.35)$, $Z_V^{\overline{\mathrm{MS}}/\mathrm{lat}}(4.47)$, $C_{-2}(\theta < 20°)$, $C_{-2}(20° \leq \theta < 30°)$, $C_{4,G}$, $C_{6,q}$, $C_{6,mG}$, and $C_{6,mq}$. Here, the last four parameters correspond to the contribution of $\langle a_s GG\rangle$, $\langle \bar{q}q\bar{q}q\rangle$, $m_q^2\langle GG\rangle$, and $m_q^3\langle \bar{q}q\rangle$, respectively. In this analysis, we neglect the $O(a_s)$ correction to the Wilson coefficients of these operators. The terms of $O(x^6)$ involve the logarithmic dependence $\ln(x/x_0)^2$ as discussed in Section 2.4. Here we do not consider this effect because $\ln(x/x_0)^2$ is roughly constant in the fit range and their effects cannot be identified. The fit results are shown in Fig. 4.3 by the curves. Here, both the results for $\theta < 20°$ and $20° \leq \theta < 30°$ are plotted.

In Table 4.1, the results for $Z_V^{\overline{\mathrm{MS}}/\mathrm{lat}}$ are summarized with the errors from various sources. The first error is the statistical error. The second represents the discretization error. The central value is the fit result with a lower bound $(x_{\mathrm{low}}/a)^2 = 23$, which is shown in Fig. 4.3. and the second error is estimated by moving the lower bound in the region $19 \leq (x_{\mathrm{low}}/a)^2 \leq 27$ and taking the largest difference from the central value. The third is an estimate of the uncertainty of the higher order corrections of the perturbative expansion as discussed in Section 2.2. The central value is calculated with $\mu_x^{*,\mathrm{opt}}$ in (2.14) and the uncertainty is estimated by the maximum difference of results with μ_x^* in the region $[\frac{1}{2}\mu_x^{*,\mathrm{opt}}, 2\mu_x^{*,\mathrm{opt}}]$. The last error is from the uncertainty of Λ_{QCD} or of the strong coupling constant. We use the value $\Lambda_{\mathrm{QCD}}^{\overline{\mathrm{MS}},n_f=3} = 340(8)$ MeV reported by Particle Data Group [60]. The uncertainty of the lattice spacing does not significantly affect the results. The upper bound of the fit range is fixed to 0.485 fm.

TABLE 4.1: Result for the renormalization factor $Z_V^{\overline{\mathrm{MS}}/\mathrm{lat}}(a)$ of the vector channel.

β	$Z_V^{\overline{\mathrm{MS}}/\mathrm{lat}}(a)$	Errors			
		Stat.	Disc.	μ_x^*	Λ_{QCD}
4.17	0.9553	(53)	(74)	(8)	(5)
4.35	0.9636	(34)	(46)	(7)	(4)
4.47	0.9699	(26)	(38)	(6)	(4)

The fit result for other parameters reads

$$\begin{aligned} &C_{-2}(\theta < 20^\circ) = 14.0(1.2)(2.0)(1)(1), && C_{-2}(20^\circ \leq \theta < 30^\circ) = 15.1(1.1)(2.2)(1)(-),\\ &C_{4,G} = 0.564(190)(187)(99)(14)\ \mathrm{fm}^{-4}, && C_{6,q} = -0.109(61)(56)(4)(3)\ \mathrm{fm}^{-6},\\ &C_{6,mG} = -19.8(31.5)(5)(3)(1)\ \mathrm{fm}^{-4}, && C_{6,mq} = 192(125)(2)(2)(1)\ \mathrm{fm}^{-3}. \end{aligned}$$

The error estimation is same as in Table 4.1. The consistency of this analysis can be checked by evaluating the gluon condensate from the fit result. Using (2.53b) and the fit result $C_{4,G}$, we obtain $\langle(\alpha_s/\pi)GG\rangle = 0.017(6)(6)(3)\,(-)\ \mathrm{GeV}^4$ at the lowest order of α_s/π. The errors are estimated in the similar manner. This result is in good agreement with known values, *e.g.* $\langle(\alpha_s/\pi)GG\rangle = 0.012\ \mathrm{GeV}^4$ from the sum rule for charmonium [4] and $\langle(\alpha_s/\pi)GG\rangle = 0.006(12)\ \mathrm{GeV}^4$ from the spectral functions of hadronic τ decays [20].

4.4 Determination of Z_S

The domain-wall fermions also guarantee the agreement of the renormalization constants of the scalar $Z_S^{\overline{\mathrm{MS}}/\mathrm{lat}}(a)$ and pseudoscalar $Z_P^{\overline{\mathrm{MS}}/\mathrm{lat}}(a)$ densities. The determination of $Z_S^{\overline{\mathrm{MS}}/\mathrm{lat}}(a)$ and $Z_P^{\overline{\mathrm{MS}}/\mathrm{lat}}(a)$ may be more complicated due to the instanton-induced 't Hooft interactions [7, 10], which affect the scalar and pseudoscalar correlators significantly and are not described by OPE. Since the instanton effects to the scalar and pseudoscalar correlators are the same magnitude with an opposite sign, the naïve average $\frac{1}{2}(\Pi_S(x)+\Pi_P(x))$ may cancel such effects and could be well explained by OPE. The average contains the contribution of the chiral condensate in OPE, which we try to cancel by using the difference between the vector and axial-vector correlators. Namely, we analyze

$$\begin{aligned} &\widetilde{Z}^{\overline{\mathrm{MS}}/\mathrm{lat}}_{(S+P)/2+(V-A)/16}(2\ \mathrm{GeV}, a; x)\\ &\qquad = \sqrt{\frac{\Pi_S^{\overline{\mathrm{MS}}}(2\ \mathrm{GeV}; x)}{\frac{1}{2}\left(\Pi_S^{\mathrm{lat}}(a;x) + \Pi_P^{\mathrm{lat}}(a;x)\right) + \frac{1}{16}\left(\Pi_V^{\mathrm{lat}}(a;x) - \Pi_A^{\mathrm{lat}}(a;x)\right)}}, \end{aligned} \tag{4.9}$$

whose OPE does not depend on the chiral condensate $m_q\langle\bar{q}q\rangle x^4$ at tree-level. Since we neglect the $O(a_s)$ correction to the Wilson coefficients in this analysis, we omit the renormalization factor for $\Pi_V^{\mathrm{lat}}(a;x) - \Pi_A^{\mathrm{lat}}(a;x)$.

We implement the simultaneous fit to the data of (4.9) with the same function as (4.8). The results are summarized in Table 4.2. The error estimation is done in the same manner as that for the vector channel. We choose the lower bound of the fit range as $(x_{\mathrm{low}}/a)^2 = 16$ for the central value and estimate the second error by changing x_{low} in the region $12 \leq (x_{\mathrm{low}}/a)^2 \leq 20$. The central $\mu_x^* = \mu_x^{*,\mathrm{opt}}$ is given by (2.23) and the third error is estimated by varying μ_x^* in the region $[\frac{1}{1.6}\mu_x^{*,\mathrm{opt}}, 1.6\mu_x^{*,\mathrm{opt}}]$. The upper bound of the fit range is fixed to 0.460 fm. The fit result is shown in Fig. 4.4 for the same ensembles as in Fig. 4.3.

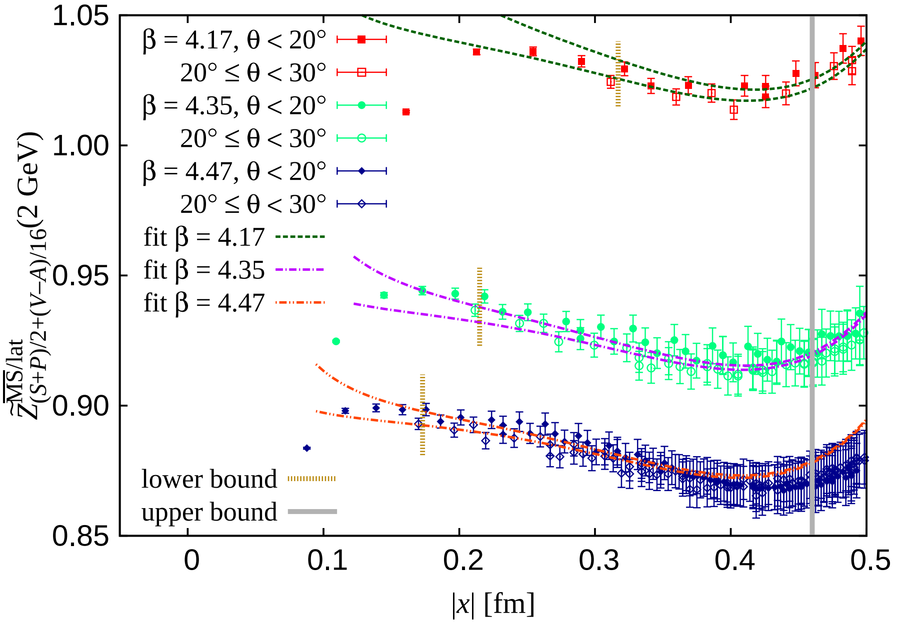

FIGURE 4.4: Same as Fig. 4.3 but for $\widetilde{Z}^{\overline{\rm MS}}_{(S+P)/2+(V-A)/16}(2\ {\rm GeV}, a; x)$

The fit result for other parameters reads

$$\begin{aligned} &C_{-2}(\theta < 20^\circ) = 2.25(1.37)(1.81)(58)(77), && C_{-2}(20^\circ \le \theta < 30^\circ) = 0.522(1.39)(1.72)(60)(80),\\ &C_{4,G} = -2.27(52)(25)(23)(33)\ {\rm fm}^{-4}, && C_{6,q} = 7.71(52)(1.08)(2.19)(45)\ {\rm fm}^{-6},\\ &C_{6,mG} = 212(156)(4)(3)(2)\ {\rm fm}^{-4}, && C_{6,mq} = -432(622)(18)(7)(3)\ {\rm fm}^{-3}. \end{aligned}$$

The error estimation is same as in Table 4.2. Unlike the case of the vector channel, the discretization effects are mostly consistent with zero.

TABLE 4.2: Result for the renormalization factor $Z_S^{\overline{\rm MS}/{\rm lat}}(2\ {\rm GeV}, a)$ of the scalor channel.

β	$Z_S^{\overline{\rm MS}/{\rm lat}}(2\ {\rm GeV}, a)$	Errors			
		Stat.	Disc.	μ_x^*	$\Lambda_{\rm QCD}$
4.17	1.0372	(93)	(77)	(57)	(58)
4.35	0.9342	(57)	(43)	(37)	(34)
4.47	0.8926	(41)	(35)	(30)	(25)

Chapter 5

Validity of lattice calculation of current correlators

5.1 $V+A$ and $V-A$ from the spectral function of hadronic tau decays

In this section, we test the consistency between the lattice calculations and the experimental correlators, which are converted from the ALEPH spectral functions as discussed in Section 2.6. We analyze the sum and difference of the vector and axial-vector correlators normalized by the tree-level correlator:

$$R_{V\pm A}(x) = \left(Z_V^{\overline{\mathrm{MS}}/\mathrm{lat}}(a)\right)^2 \frac{\Pi_V^{(1)}(x) \pm \Pi_A^{(1)}(x)}{2\Pi_V^{\mathrm{free}}(x)}. \tag{5.1}$$

Here, the correlators are projected onto the contribution of spin one,

$$\Pi_V^{(1)}(x) = \Pi_V(x), \tag{5.2}$$

$$\Pi_A^{(1)}(x) = \Pi_A(x) - \sum_{x_0} \frac{z_0^A M_\pi^2}{2\pi^2} \frac{K_1(M_\pi|x-x_0|)}{|x-x_0|}, \tag{5.3}$$

with z_0^A and M_π being the fit parameters for the zero-momentum correlator (3.17). The sum over x_0 runs over

$$x_0 \in \{(0,0,0,0), (\pm L,0,0,0), (0,\pm L,0,0), (0,0,\pm L,0), (0,0,0,\pm T), (\pm L,\pm L,0,0), \ldots\}, \tag{5.4}$$

to subtract both the contribution of the pion pole and its finite volume effects.

The $V-A$ channel vanishes in the massless perturbation theory. The non-vanishing value of this channel is due to the chiral symmetry breaking. On the other hand, the chirally symmetric contributions such as the perturbative contribution are encoded only in the $V+A$ channel. Thus, the investigation of the $V+A$ and $V-A$ provides a clean separation of the different kind of contributions.

Figure 5.1 shows the results of $R_{V+A}(x)$ at different β with matched pion masses $M_\pi \sim$ 300 MeV. Here, we also show the prediction of perturbation theory (dashed line) and the experimental result using the dispersion relation, which is calculated with (hatched band) and

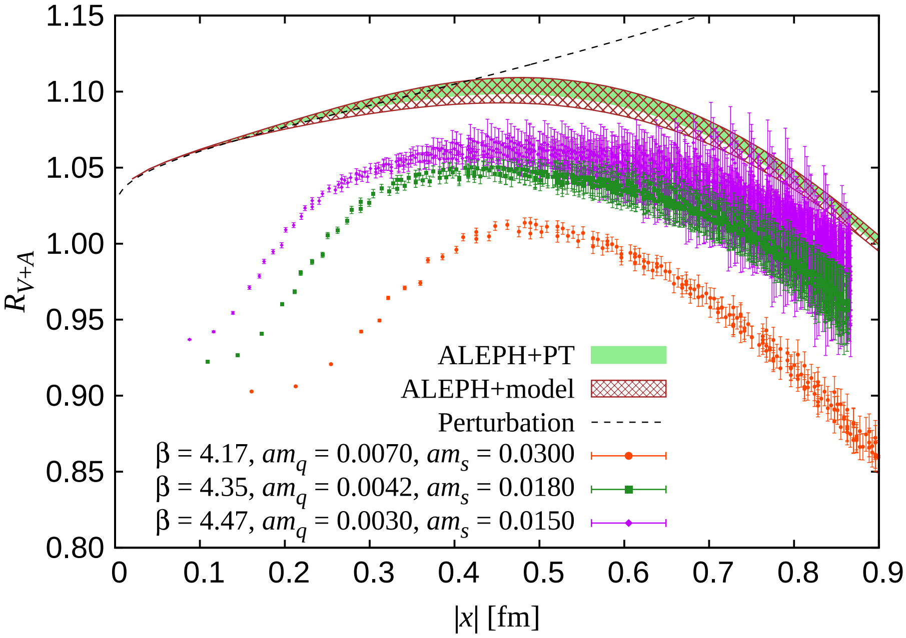

FIGURE 5.1: R_{V+A} calculated at the same ensembles as in Fig. 4.2, plotted with the prediction of perturbation theory (dashed curve) and the result of the experiment (bands).

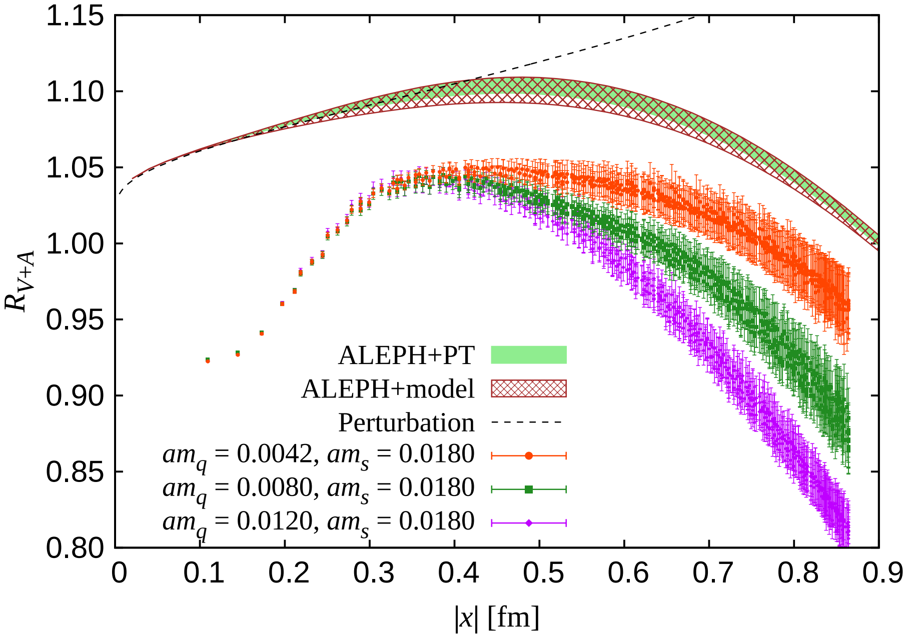

FIGURE 5.2: Same as Fig. 5.1 but calculated at the same ensembles as in Fig. 4.1.

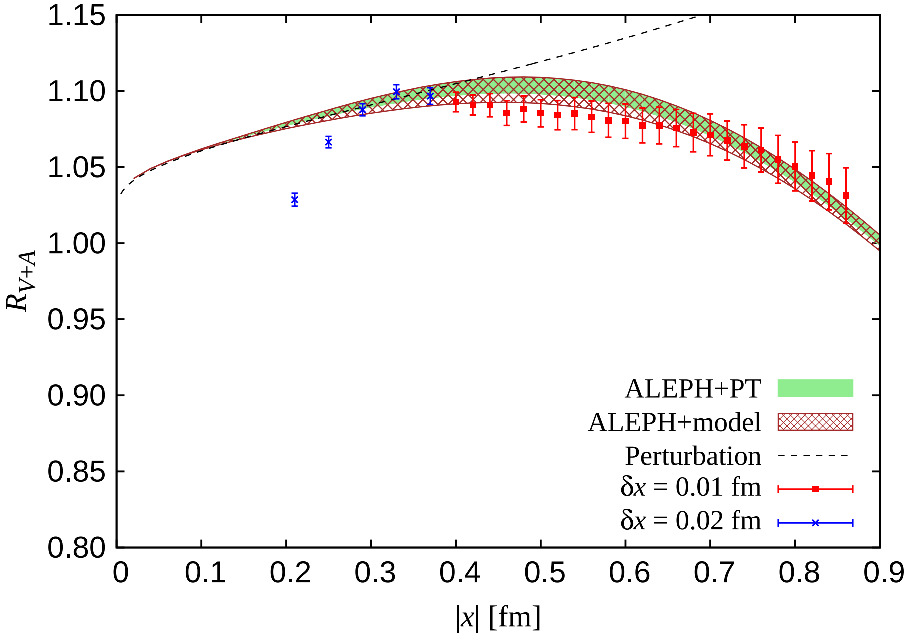

FIGURE 5.3: Extrapolation of R_{V+A} to the physical point.

without (filled band) the duality violating term $\rho^{\rm DV}_{V/A}(s)$ of the spectral function in $s > 2.8$ GeV^2 (See Section 2.6 for more detail). As we saw in the previous chapter, there is a significant dependence on the lattice spacing, which is well managed by a term $\propto a^2$ at middle and long distances. The result at a smaller lattice spacing is closer to the experimental result, implying that the continuum extrapolation gets close to the experiment. The mass dependence is visible at long distances as shown in Fig. 5.2. The fact that result at a smaller mass is closer to the experiment implies the chiral extrapolation also gets close to the experiment. The dependence on the strange quark mass is not clear as seen in Fig. F.5, which shows the result for all ensembles.

We extrapolate lattice data to the physical point, *i.e.* continuum limit and physical pion mass as follows. At first, we separate the lattice data into bins with respect to x such as

$$B_i = [x_i - \delta x, x_i + \delta x], \quad i = 1, 2, \dots, N, \tag{5.5}$$

with a sequence of x_i and width δx, and average $R_{V+A}(a, M_\pi; x)$ over x in the bin,

$$\overline{R}_{V+A}(a, M_\pi; x_i) \equiv \frac{1}{|B_i(a)|} \sum_{x \in B_i(a)} R_{V+A}(a, M_\pi; x), \tag{5.6}$$

where $B_i(a)$ stands for the set of lattice sites in the window B_i collected from the lattice at the spacing a. We extrapolate the data in B_i using the fit function

$$\overline{R}_{V+A}(a, M_\pi; x_i) = R_{V+A}(0, m_\pi, x_i) + c^+_{m,i}(M_\pi^2 - m_\pi^2) + c^+_{a,i} a^2, \tag{5.7}$$

with three free parameters $R_{V+A}(0, m_\pi, x_i), c^+_{m,i}$ and $c^+_{a,i}$. The result is shown in Fig. 5.3. The consistency between the lattice result and the experiment is seen in the region of $x > 0.3$ fm.

Figure 5.4 shows the result of $R_{V-A}(x)$ at matched pion masses $M_\pi \simeq 300$ MeV and different β. In the figure, we do not see the significant dependence on the lattice spacing in short distances ($\lesssim 0.5$ fm) unlike the case of $R_{V+A}(x)$. This is because the most significant discretization effect at short-distances is perturbative, which is cancelled for the $V-A$ channel. $R_{V-A}(x)$ vanishes in the short-distance limit because of chiral symmetry of the Möbius domain-wall fermions. The slight deviation of the result at $\beta = 4.47$ at longer distances is possibly due to the poor statistics.

In Fig. 5.5, which shows the result at different masses and at same β, we find a clear dependence on input mass at short distances ($\lesssim 0.5$ fm) and the chiral extrapolation is expected to get close to the experimental result. At longer distances, the statistical fluctuation becomes larger and the mass dependence becomes less clear, though we can expect from the result on all ensembles shown in Fig. F.6 that the chiral extrapolation gets close to the experiment.

We extrapolate $R_{V-A}(x)$ to the physical mass in the same manner as for $R_{V+A}(x)$,

$$\begin{aligned} \overline{R}_{V-A}(a, M_\pi; x_i) &\equiv \frac{1}{|B_i(a)|} \sum_{x \in B_i(a)} R_{V-A}(a, M_\pi; x), \\ \overline{R}_{V-A}(a, M_\pi; x_i) &= R_{V-A}(0, m_\pi, x_i) + c^-_{m,i}(M_\pi^2 - m_\pi^2) + c^-_{a,i} a^2, \end{aligned} \tag{5.8}$$

with $c^-_{m,i}$ and $c^-_{a,i}$ being the parameters to control the mass dependence and cutoff dependence, respectively. The result is shown in Fig. 5.6. The consistency between the lattice result and the experiment is seen in the region of $x > 0.2$ fm.

5.2 Chiral condensate from axial Ward identity

In this section, we show the result of the analysis of the chiral condensate calculated from the PCAC relation. On the lattice, some modifications to (2.46) is needed. The violation of the current conservation induces the discretization effect from the derivative term as well as the non-trivial renormalization as discussed in the previous chapter. Fortunately, the discretization effect from the derivative is mostly eliminated by subtracting the counterpart of the vector channel. We also take account of the violation of the Ginsparg-Wilson relation by adding the residual mass m_{res} to the valence quark mass m_q. In addition, we renormalize the chiral condensate by multiplying the renormalization factor $Z_S^{\overline{\mathrm{MS}}/\mathrm{lat}}(2\ \mathrm{GeV}; a)$ of the scalar density to 2 GeV in the $\overline{\mathrm{MS}}$ scheme determined in [95]. Consequently, we modify (2.46) to

$$\Sigma^{\overline{\mathrm{MS}}}_{m_q}(2\ \mathrm{GeV}; x) \equiv \frac{\pi^2 Z_V^{\overline{\mathrm{MS}}/\mathrm{lat}}(a)^2 Z_S^{\overline{\mathrm{MS}}/\mathrm{lat}}(2\ \mathrm{GeV}; a)}{2(m_q + m_{res})} x^2 \sum_{\mu,\nu} x_\nu \nabla_\mu \big(\Pi_{A,\mu\nu}(x) - \Pi_{V,\mu\nu}(x)\big), \tag{5.9}$$

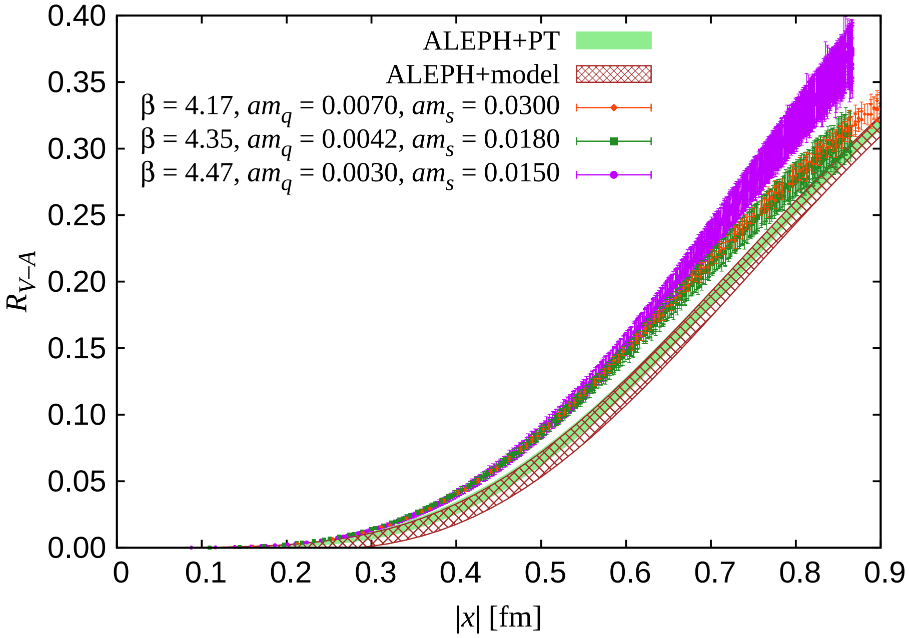

FIGURE 5.4: R_{V-A} calculated at the same ensembles as in Fig. 4.2, plotted with result of the experiment with (hatched band) and without the duality violating term.

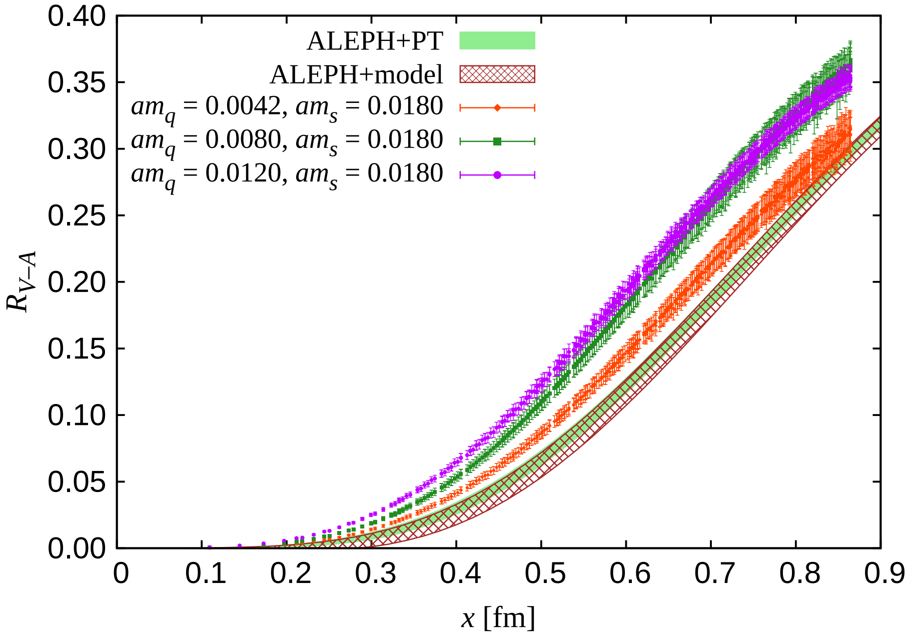

FIGURE 5.5: Same as Fig. 5.4 but calculated at the same ensembles as in Fig. 4.1.

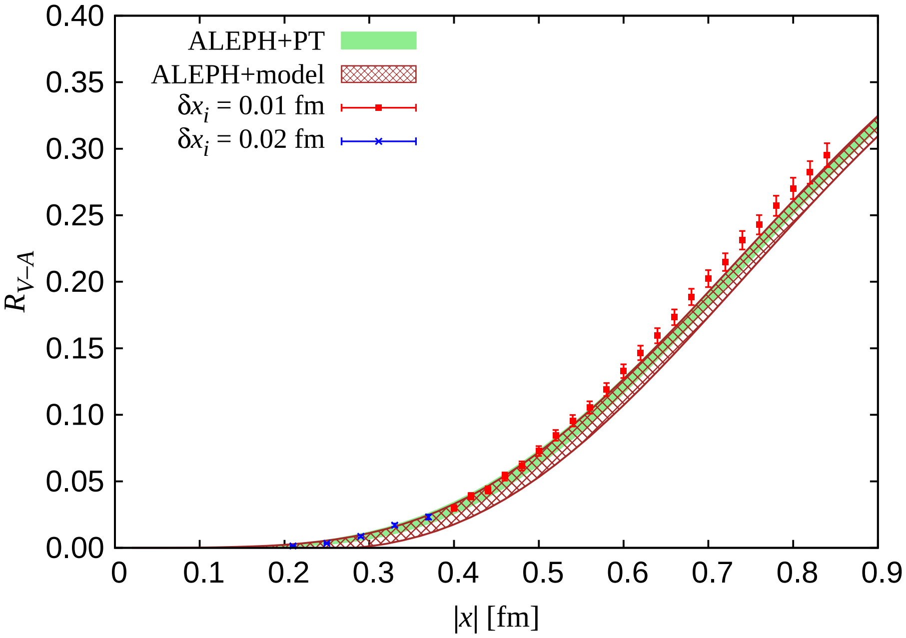

FIGURE 5.6: Extrapolation of R_{V-A} to the physical point.

where the derivative ∇_μ on the lattice is defined as a symmetric difference,

$$\nabla_\mu f(x) = \frac{f(x+a\hat{\mu}) - f(x-a\hat{\mu})}{2a}, \tag{5.10}$$

with $\hat{\mu}$ being the unit vector for the μ-direction.

This quantity may be contaminated by the finite volume effect due to the pion pole. The finite volume effect on Σ_{m_q} is estimated as follows. Let us define

$$K(x) \equiv \sum_{\mu,\nu} x_\nu \nabla_\mu \big(\Pi_{A,\mu\nu}(x) - \Pi_{V,\mu\nu}(x)\big). \tag{5.11}$$

This quantity in the infinite box $K^\infty(x)$ is approximated by

$$\begin{aligned} K^\infty(x) &\to \sum_{\mu,\nu} x_\nu \partial_\mu \Pi_{A,\mu\nu}(x) \\ &= -\sum_\mu x_\mu \partial_\mu \int \frac{\mathrm{d}^4 q}{(2\pi)^4} \mathrm{e}^{-\mathrm{i}qx} q^2 \widetilde{\Pi}_A^{(0)}(-q^2), \end{aligned} \tag{5.12}$$

at long distances. Since the Fourier integral on the RHS is related to the zero-momentum correlator by (3.15), $K^\infty(x)$ has the asymptotic form in the long-distance limit,

$$\begin{aligned} K^\infty(x) &\to -\frac{M_\pi^2 z_0^A}{2\pi^2} \sum_\mu x_\mu \partial_\mu \frac{K_1(M_\pi|x|)}{|x|} \\ &= \frac{M_\pi^2 z_0^A}{4\pi^2} \left[M_\pi K_0(M_\pi|x|) + \frac{2K_1(M_\pi|x|)}{|x|} + M_\pi K_2(M_\pi|x|) \right] \equiv K^{\infty,c}(x), \end{aligned} \tag{5.13}$$

with z_0^A and M_π being the fit parameters for the zero-momentum correlator (3.17). $K^{L^3\times T}(x)$, which is defined by (5.11) in a finite box $L^3 \times T$, is approximated by

$$K^{L^3\times T}(x) \simeq K^{\infty}(x) + \sum_{x_0} K^{\infty,c}(x - x_0), \tag{5.14}$$

where x_0 runs over all possible source points shown in (3.9). Inserting $K^\infty(x)$ into (5.9), we obtain

$$\Sigma_{m_q}^{\overline{\mathrm{MS}}}(2\ \mathrm{GeV}; x) = \frac{\pi^2 Z_V^{\overline{\mathrm{MS}}/\mathrm{lat}}(a)^2 Z_S^{\overline{\mathrm{MS}}/\mathrm{lat}}(2\ \mathrm{GeV}; a)}{2(m_q + m_{res})} x^2 \left(K^{L^3\times T}(x) - \sum_{x_0} K^{\infty,c}(x - x_0) \right), \tag{5.15}$$

which is analyzed in this work.

Figures 5.7 and 5.8 show the results at some ensembles. The light-green and gray bands stand for the last [96] and second last [97] update of the FLAG average of the chiral condensate $\Sigma^{\overline{\mathrm{MS}}}(2\ \mathrm{GeV}) = -\lim_{m_q,m_s\to 0}\langle \bar{q}q\rangle^{\overline{\mathrm{MS}}}(2\ \mathrm{GeV})$ at $n_f = 2{+}1$. This chiral condensate can in principle be realized by taking the chiral limit of $\Sigma_{m_q}^{\overline{\mathrm{MS}}}(2\ \mathrm{GeV}; x)$. Certainly, one can find from Fig. 5.7 that the result at a smaller mass is closer to the FLAG average. From Fig. 5.8, which shows the results of different β with matched pion masses $\sim$ 300 MeV, we find that there is no significant dependence on the lattice spacing.

We extrapolate $\Sigma_{m_q}^{\overline{\mathrm{MS}}}(2\ \mathrm{GeV})$ to the chiral limit and the continuum limit. We separate lattice data into bins with respect to x by (5.5) and average $\Sigma_{m_q}^{\overline{\mathrm{MS}}}$ over $x \in B_i(a)$,

$$\bar{\Sigma}_{m_q}^{\overline{\mathrm{MS}}}(2\ \mathrm{GeV}; a, M_\pi; x_i) \equiv \frac{1}{|B_i(a)|} \sum_{x\in B_i(a)} \Sigma_{m_q}^{\overline{\mathrm{MS}}}(2\ \mathrm{GeV}; a, M_\pi; x), \tag{5.16}$$

Then, we perform the simultaneous fit using the fit functions

$$\bar{\Sigma}_{m_q}^{\overline{\mathrm{MS}}}(2\ \mathrm{GeV}; a, M_\pi; x_i) = \Sigma^{\overline{\mathrm{MS}}}(2\ \mathrm{GeV}) + c_m(x_i)M_\pi^2 + c_a(x_i)a^2, \quad i = 1, 2, \ldots, N, \tag{5.17}$$

with some dozens of of free parameters $\Sigma^{\overline{\mathrm{MS}}}(2\ \mathrm{GeV})$, $c_m(x_i)$'s and $c_a(x_i)$'s. Note that since the extrapolated value $\Sigma^{\overline{\mathrm{MS}}}(2\ \mathrm{GeV})$ must be independent of x unlike the case of $R_{V\pm A}(x)$ discussed in the previous section, the global fit is performed for all x_i as well as all ensembles. Table 5.1 summarizes the result with several fit ranges and bin widths parametrized by x_1, x_N and δx. The dependence on the bin width is mostly negligible. On the other hand, the dependence on the fit range is comparable to the statistical error. Containing this uncertainty as a systematic error, we determine the chiral condensate as $\left(\Sigma^{\overline{\mathrm{MS}}}(2\ \mathrm{GeV})\right)^{1/3} = 284.9 \pm 4.0_{\mathrm{stat}} \pm 8.8_{\mathrm{sys}}$ MeV. Here, the central value and the statistical error are estimated as the average of the four results at the fit range 0.23–0.83 fm with various widths δx, while the systematic error is estimated as the maximum difference between the central value and the results at various fit ranges. Other systematic errors such as the uncertainty due to the systematic error of the renormalization factors are sufficiently smaller than the shown two errors. This result is almost consistent with the

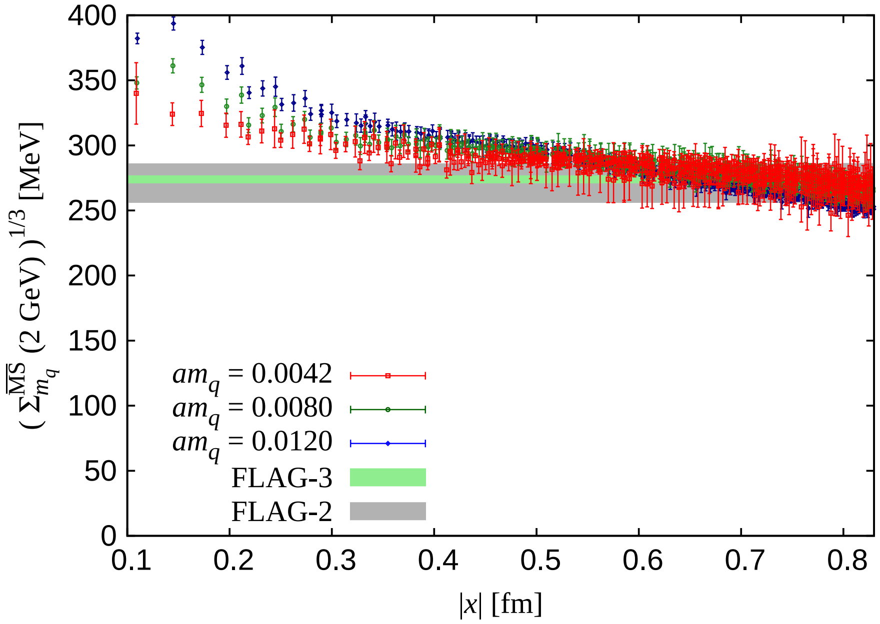

FIGURE 5.7: Cubic root of $\Sigma_{m_q}^{\overline{\mathrm{MS}}}(2\ \mathrm{GeV}, a)$. The results at the same ensembles as in Fig. 4.1 are shown. The light-green and gray band stand for the FLAG average and the ambiguity of the chiral condensate at 2 GeV in the $\overline{\mathrm{MS}}$ scheme with $n_f = 3$.

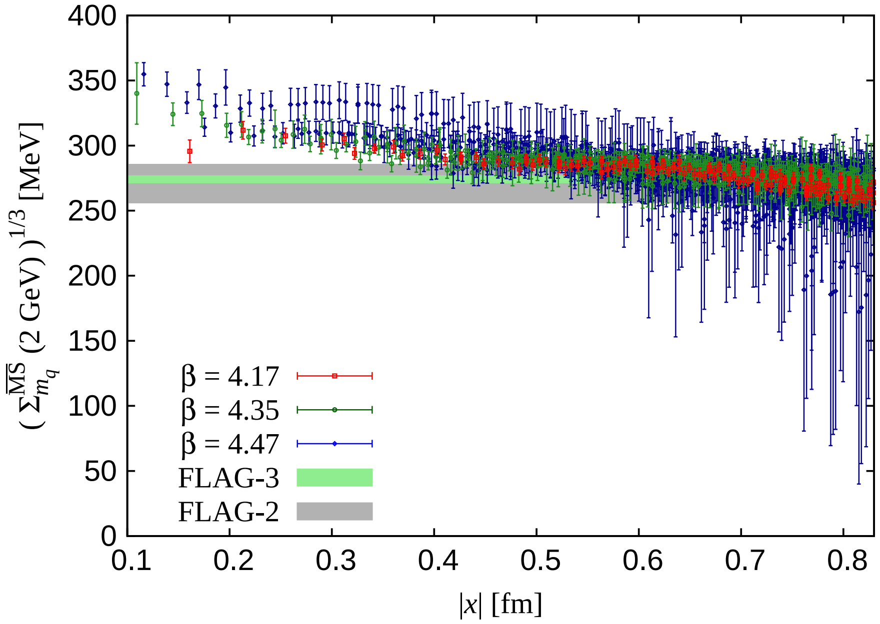

FIGURE 5.8: Same as Fig. 5.7 but the result at the same ensembles as in Fig. 4.3.

TABLE 5.1: Chiral condensate extracted from the global fit using (5.17) at various fit ranges and bin widths.

$x_1 - \delta x/2$ [fm]	$x_N + \delta x/2$ [fm]	δx [fm]	N	$\Sigma^{\overline{\mathrm{MS}}}(2\ \mathrm{GeV})^{1/3}$ [MeV]
0.23	0.83	0.02	30	$284.3(4.0)$
0.23	0.83	0.04	15	$285.2(4.0)$
0.23	0.83	0.06	10	$284.5(4.0)$
0.23	0.83	0.10	6	$285.7(4.0)$
0.23	0.43	0.04	5	$293.7(5.4)$
0.31	0.51	0.04	5	$290.7(5.0)$
0.39	0.59	0.04	5	$288.9(4.6)$
0.47	0.67	0.04	5	$285.5(4.4)$
0.55	0.75	0.04	5	$280.8(4.0)$
0.63	0.83	0.04	5	$276.2(3.8)$

FLAG average [96] $274(3)$ MeV and the result by another method by the stochastic calculation of the Dirac spectrum using the same lattice ensembles [98] $270.0(4.9)$ MeV.

Chapter 6

Conclusion and discussion

We have investigated the current correlators of the iso-triplet scalar and pseudoscalar densities and the vector and axial-vector currents using the lattice simulation with $2+1$-flavor Möbius domain-wall fermions.

The renormalization factors of the (pseudo)scalar density and the (axial-)vector current is determined, by the X-space method, with the precision of $O(1\%)$ or less. Through the renormalization process, it turns out that OPE is useful in $|x| < 0.45$ fm.

Consistency between the lattice results and experimental data is seen both for the $V+A$ and $V-A$ channels. For the $V+A$ channel, the agreement between the experiment and the lattice results from our ensembles is seen in the region $|x| > 0.3$ fm. The discretization effects in the $V-A$ channel is on the other hand much smaller than those in the $V+A$ channel. The agreement between the experiment and the lattice result of the $V-A$ channel is seen at $|x| \simeq 0.2$ fm and longer.

The chiral condensate is extracted by an approach based on the PCAC relation. We obtain $\Sigma^{\overline{\mathrm{MS}}}(2\ \mathrm{GeV})^{1/3} = 284.9(9.7)$ MeV, which is almost consistent with the FLAG average of the chiral condensate for the $2+1$-flavor QCD.

Throughout this work, we have seen the potential of current correlators as a tool to investigate QCD. At short and middle distances, they are not investigated a lot by lattice simulations. In this work, we tested the validity of the lattice calculation at short and middle distances by comparing with the experiments as well as with OPE. Then, we could identify the region where a channel of correlator is mostly perturbative. For example, it terned out that the vector and axial-vector correlators are mostly perturbative in the region $|x| \lesssim 0.3$ fm. Thus, lattice study of current correlators can give a judgment about the region where a continuum theory such as perturbation theory and OPE is applicable. This judgment is convenient when one uses a perturbative approach to analyze some experimental data or to give some predictions.

Current correlators provide a rich source of information on the QCD vacuum from the perturbative to non-perturbative regime. As the distance of the two currents becomes longer, the non-perturbative effects due to the spontaneous breaking of chiral symmetry becomes more significant. This gradual arising of the non-perturbative effects can be investigated by analyzing current correlators. Therefore, current correlators could be helpful to understand the non-perturbative structure of the QCD vacuum.

Appendix A

Euclidean formulation

Lattice simulations are implemented always in the Euclidean space. In this appendix, we review the connection between the Minkowski and Euclidean formulations. The Minkowski notation we employed here is

$$g_{\mu\nu} = \mathrm{diag}(1, -1, -1, -1), \quad \mu, \nu = 0, 1, 2, 3, \tag{A.1}$$

$$\{\gamma_\mu^M, \gamma_\nu^M\} = 2g_{\mu\nu} \cdot \mathbb{1}_{\mathrm{spin}}, \tag{A.2}$$

$$\gamma_5^M = \mathrm{i}\gamma_0^M\gamma_1^M\gamma_2^M\gamma_3^M. \tag{A.3}$$

We can relate the field theory in the Minkowski space to that in the Euclidean space by the analytic continuation with respect to the time variable x_0^M to the imaginary axis. In the Euclidean space, the time variable x_0^M is substituted by

$$x_4 = +\mathrm{i}x_0^M, \tag{A.4}$$

while the substitutions for the other directions are identical:

$$x_i = x_i^M, \quad i = 1, 2, 3. \tag{A.5}$$

Then, the square of the coordinate variable obeys the Euclidean metric as follows.

$$\left(x^M\right)^2 = \left(x^M\right)_0^2 - \left(x^M\right)_i^2 = -x_4^2 - x_i^2 = -x^2 \tag{A.6}$$

On the other hand, the definition of the momentum q_μ in the Euclidean space should be chosen as $q = (q_i, q_4) = (q_i, \mathrm{i}q_0)$ because the product of q^M and x^M in the Minkowski metric should becomes the product of q and x in the Euclidean metric:

$$q^M x^M = q_0^M x_0^M - q_i^M x_i^M = -q_4 x_4 - q_i x_i = -qx. \tag{A.7}$$

Thus, the substitution rule for q is same as x.

With the Euclidean metric $\delta_{\mu\nu}$, the algebra of gamma matrices is imposed to obey

$$\{\gamma_\mu, \gamma_\nu\} = 2\delta_{\mu\nu} \cdot \mathbb{1}_{\mathrm{spin}}. \tag{A.8}$$

A conventional choice of the relation between γ^M_μ and γ_μ obeying (A.8) is given by[1]

$$\gamma_i = -\mathrm{i}\gamma^M_i, \ \ \gamma_4 = \gamma^M_0. \tag{A.9}$$

The chirality operator γ_5 in the Euclidean space is determined so that it anti-commutes with γ_μ $(\mu = 1, 2, 3, 4)$ and satisfies $\gamma_5^2 = 1$,

$$\gamma_5 = \gamma_1\gamma_2\gamma_3\gamma_4 = \gamma^M_5. \tag{A.10}$$

For other Lorentz vectors or tensors $\omega_{\mu_1\cdots\mu_p}$, the substitution rule should be opposite to that of the coordinate variable x or p,

$$\omega_{\mu_1\cdots\mu_p} = (-\mathrm{i})^{N_{\vec{\mu}}}\omega^M_{\mu'_1\cdots\mu'_p}, \tag{A.11}$$

where $(\mu_k, \mu'_k) = (i, i), \ i = 1, 2, 3$ or $(\mu_k, \mu'_k) = (4, 0)$ and $N_{\vec{\mu}}$ is the number of 0 in $(\mu_1, \cdots, \mu_p)$. This substitution rule is understood from the context of the differential geometry. A tensor field ω with respect to the basic variable $\xi(= x$ or $p)$ has the form

$$\omega(\xi) = \sum_{\mu_1,\cdots,\mu_p} \omega_{\mu_1\cdots\mu_p}(\xi)\mathrm{d}\xi^{\mu_1} \otimes \cdots \otimes \mathrm{d}\xi^{\mu_p}. \tag{A.12}$$

Since the tensor field ω is geometric and independent of coordinates ξ, the following relation must be guaranteed.

$$\begin{aligned} \omega(\xi) = \omega^M(\xi^M) &= \sum_{\mu'_1,\cdots,\mu'_p} \omega^M_{\mu'_1\cdots\mu'_p}(\xi^M)\mathrm{d}\xi^{M\ \mu'_1} \otimes \cdots \otimes \mathrm{d}\xi^{M\ \mu'_p} \\ &= \sum_{\mu_1,\cdots,\mu_p} (-\mathrm{i})^{N_{\vec{\mu}}}\omega^M_{\mu'_1\cdots\mu'_p}(\xi^M)\mathrm{d}\xi^{\mu_1} \otimes \cdots \otimes \mathrm{d}\xi^{\mu_p}. \end{aligned} \tag{A.13}$$

The independency of the basis $\mathrm{d}\xi^{\mu_1} \otimes \cdots \otimes \mathrm{d}\xi^{\mu_p}$ ensures eq. (A.11). As an example of this substitution, the gauge field $A_\mu(x)$ obeys

$$A_i(x) = A^M_i(x^M), \ \ A_4(x) = -\mathrm{i}A^M_0(x^M), \tag{A.14}$$

and the differential operator ∂_μ obeys

$$\partial_i = \partial^M_i, \ \ \partial_4 = -\mathrm{i}\partial^M_0. \tag{A.15}$$

Next, we discuss a integral over the spacetime or momentum variable. It should be noted, when we change the integral path of the time or energy variable from the real axis to the imaginary axis, that singularities of the integrand may lead to a wrong result of the complex integral.

---

[1] More precisely, the substitution of variables from Minkowski to Euclidean changes metric $g_{\mu\nu}$ into $-\delta_{\mu\nu}$. However we assume the metric in Euclidean formulation is $\delta_{\mu\nu}$. This inconsistency leads to the difference between substitution rules for the gamma matrices and for x and p.

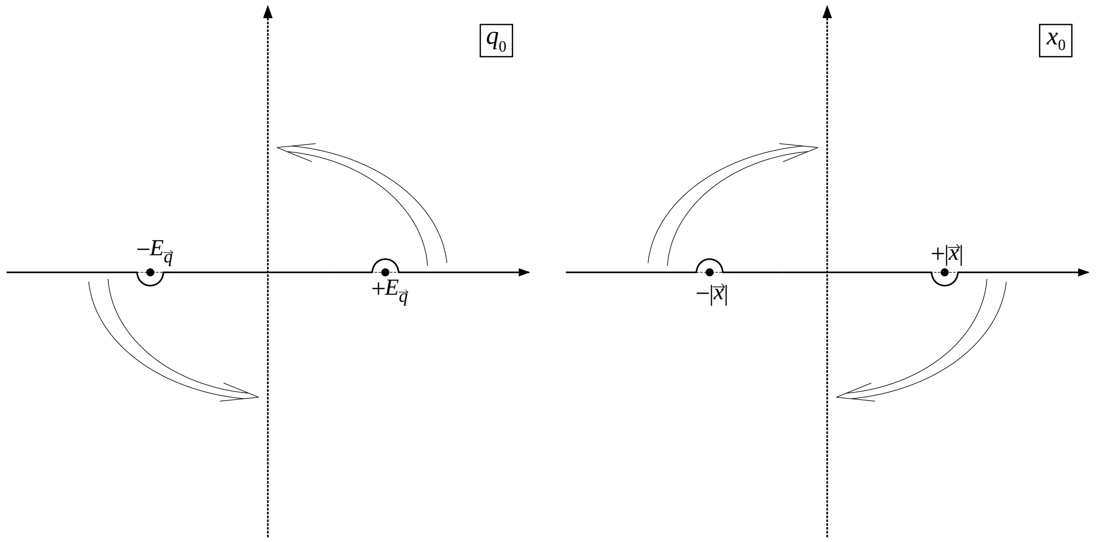

FIGURE A.1: Wick's rotation from the Minkowski to the Euclidean space in the momentum (left panel) and coordinate spaces (right panel). The dots stand for the singular points of a propagator. The difference of the positions of the singular points leads to the difference of directions between two Wick's rotations for the momentum and coordinate spaces.

Feynman propagators in the Minkowski momentum space have singularities at q^M satisfying $\left(q^M\right)^2 - m^2 + \mathrm{i}\epsilon = 0$, while those in the coordinate space have the corresponding singularities at x^M satisfying $\left(x^M\right)^2 - \mathrm{i}\epsilon = 0$. This means the contour of the integral of a propagator in the momentum space is different from that in the coordinate space as shown in Fig. A.1. This difference causes the different direction of the Wick rotations. The integration route of the time direction should be rotated through $-\pi/2$, while that of the energy direction in the momentum space should be rotated through $+\pi/2$. Consequently, the relation of integrals over the time direction between the Minkowski and Euclidean formulas is given by

$$\int_{-\infty}^{+\infty} \mathrm{d}x_0^M \cdots = -\mathrm{i} \int_{-\infty}^{+\infty} \mathrm{d}x_4 \cdots , \tag{A.16}$$

$$\int_{-\infty}^{+\infty} \frac{\mathrm{d}q_0^M}{2\pi} \cdots = +\mathrm{i} \int_{-\infty}^{+\infty} \frac{\mathrm{d}q_4}{2\pi} \cdots . \tag{A.17}$$

Fourier transform of a Minkowski function $f(x)$,

$$\tilde{f}^M\left(q^M\right) = \int \mathrm{d}^4 x^M \, \mathrm{e}^{\mathrm{i}q^M x^M} f^M\left(x^M\right), \;\; f^M\left(x^M\right) = \int \frac{\mathrm{d}^4 q^M}{(2\pi)^4} \mathrm{e}^{-\mathrm{i}q^M x^M} \tilde{f}^M\left(q^M\right), \tag{A.18}$$

becomes

$$\tilde{f}^M\big(M(q)\big) = -\mathrm{i} \int \mathrm{d}^4 x \, \mathrm{e}^{-\mathrm{i}qx} f^M\big(M(x)\big), \;\; f^M\big(M(x)\big) = \mathrm{i} \int \frac{\mathrm{d}^4 q}{(2\pi)^4} \mathrm{e}^{\mathrm{i}qx} \tilde{f}^M\big(M(q)\big), \tag{A.19}$$

where, $M(x) = (-\mathrm{i}x_4, \vec{x})$ and $M(q) = (-\mathrm{i}q_4, \vec{q})$ are Minkowski vectors. Defining

$$f(x) = f^M\big(M(x)\big), \;\; \tilde{f}(q) = \mathrm{i}\tilde{f}^M\big(M(q)\big), \tag{A.20}$$

we obtain the Fourier transforms in the Euclidean formulation.

$$\tilde{f}(q) = \int \mathrm{d}^4x \, \mathrm{e}^{-\mathrm{i}qx} f(x), \;\; f(x) = \int \frac{\mathrm{d}^4q}{(2\pi)^4} \mathrm{e}^{\mathrm{i}qx} \tilde{f}(q). \tag{A.21}$$

We finally discuss the Euclidean action and the path integral. The partition function for a Minkowski action,

$$Z_M\big[S^M\big] = \int \mathcal{D}(\text{fields})^M \, \mathrm{e}^{\mathrm{i}S^M}, \;\; S^M = \int \mathrm{d}^4x^M \, \mathcal{L}^M\big(x^M\big), \tag{A.22}$$

corresponds to that for the conventional Euclidean action,

$$Z[S] = \int \mathcal{D}(\text{fields}) \, \mathrm{e}^{-S}, \;\; S = \int \mathrm{d}^4x \, \mathcal{L}(x). \tag{A.23}$$

From these formulas and the substitution rule for the integral (A.16), the relation $\mathcal{L} = -\mathcal{L}^M$ is necessary. In the following, some typical Lagrangians in the Euclidean space are listed.

- ϕ^4 real scalar field

  Lagrangian in the Minkowski space is given as follows.

  $$\mathcal{L}^M(x) = -\frac{1}{2}\phi^M\big(x^M\big)(\partial_M^2 + m^2)\phi^M\big(x^M\big) - \frac{\lambda}{4!}\big(\phi^M\big)^4\big(x^M\big). \tag{A.24}$$

  Using (A.20), Lagrangian in the Euclidean space takes the form

  $$\mathcal{L}(x) = \frac{1}{2}\phi(x)(-\partial^2 + m^2)\phi(x) + \frac{\lambda}{4!}\phi^4(x). \tag{A.25}$$

- Dirac field coupling with a gauge field

  The Minkowski Lagrangian is

  $$\mathcal{L}^M\big(x^M\big) = \overline{\psi}^M\big(x^M\big)(\mathrm{i}\not{D}_M - m)\psi\big(x^M\big). \tag{A.26}$$

  Using (A.14) and (A.15), the substitution rule for the covariant derivative $D_\mu^M = \partial_\mu^M - \mathrm{i}gA_\mu^M$ is obtained as

  $$D_i = D_i^M, \;\; D_4 = -\mathrm{i}D_0^M. \tag{A.27}$$

  Combining this relation with the substitution rule for gamma matrices (A.9) the following form is found.

  $$\mathcal{L} = \overline{\psi}(\not{D} + m)\psi. \tag{A.28}$$

- Yang-Mills part of a gauge field

  The Minkowski Lagrangian is

$$\mathcal{L}^M = -\frac{1}{2}\mathrm{tr}\big[F^M_{\mu\nu}F^{\mu\nu}_M\big], \tag{A.29}$$

  which becomes

$$\mathcal{L} = \frac{1}{2}\mathrm{tr}\big[F_{\mu\nu}F_{\mu\nu}\big]. \tag{A.30}$$

Note that, these Euclidean Lagrangian is positive valued obeying the Boltzmann statistics. This fact allows us to perform the lattice computation by Monte Carlo simulations.

Appendix B

Scale setting of perturbative expansions

B.1 Renormalization group in perturbation theory

The scale dependence of the strong coupling constant $a_s = \alpha_s/\pi$ is described by the beta function, which is defined in the renormalization group equation,

$$\mu^2 \frac{\mathrm{d}}{\mathrm{d}\mu^2} a_s = a_s \beta(a_s) = -\sum_{i=0}^{\infty} \beta_i a_s^{i+2}, \tag{B.1}$$

whose coefficients β_i are known up to the four-loop level [46],

$$\begin{aligned}
\beta_0 =& \frac{1}{4}\left(11 - \frac{2}{3} n_f\right), \\
\beta_1 =& \frac{1}{16}\left(102 - \frac{38}{3} n_f\right), \\
\beta_2 =& \frac{1}{64}\left(\frac{2857}{2} - \frac{5033}{18} n_f + \frac{325}{54} n_f^2\right), \\
\beta_3 =& \frac{1}{256}\left(\frac{149753}{6} + 3564\zeta_3 - \left[\frac{1078361}{162} + \frac{6508}{27}\zeta_3\right] n_f \right. \\
& \left. + \left[\frac{50065}{162} + \frac{6508}{2592}\zeta_3\right] n_f^2 + \frac{1093}{729} n_f^3\right).
\end{aligned} \tag{B.2}$$

Solving the renormalization group equation (B.1), one can relate the coupling constants renormalized at two different scales as

$$\begin{aligned}
a_s(\mu) = a_s(\mu') \Bigg\{ & 1 + \beta_0 l_{\mu',\mu} a_s(\mu') + (\beta_0^2 l_{\mu',\mu} + \beta_1) l_{\mu',\mu} a_(\mu')^2 \\
& + \left(\beta_0^3 l_{\mu',\mu}^2 + \frac{5}{2}\beta_0\beta_1 l_{\mu',\mu} + \beta_2\right) l_{\mu',\mu} a_s(\mu')^3 \\
& + \left[\beta_0^4 l_{\mu',\mu}^3 + \frac{13}{3}\beta_0^2\beta_1 l_{\mu',\mu}^2 + 3\left(\frac{\beta_1^2}{2} + \beta_0\beta_2\right) l_{\mu',\mu} + \beta_3\right] l_{\mu',\mu} a_s(\mu')^4 + O(a_s^5) \Bigg\}.
\end{aligned} \tag{B.3}$$

Introducing the typical scale Λ_{QCD}, a coupling constant at a scale μ is also given by

$$
\begin{aligned}
a_s(\mu) = \frac{1}{\beta_0 l_{\mu,\Lambda_{\mathrm{QCD}}}} \Bigg[1 &- \frac{\beta_1}{\beta_0^2} \frac{\ln l_{\mu,\Lambda_{\mathrm{QCD}}}}{l_{\mu,\Lambda_{\mathrm{QCD}}}} + \frac{\beta_1^2}{\beta_0^4 l_{\mu,\Lambda_{\mathrm{QCD}}}^2} \left(\ln^2 l_{\mu,\Lambda_{\mathrm{QCD}}} - \ln l_{\mu,\Lambda_{\mathrm{QCD}}} + \frac{\beta_2\beta_0}{\beta_1^2} - 1 \right) \\
&- \frac{\beta_1^3}{\beta_0^6 l_{\mu,\Lambda_{\mathrm{QCD}}}^3} \left(\ln^3 l_{\mu,\Lambda_{\mathrm{QCD}}} - \frac{5}{2} \ln^2 l_{\mu,\Lambda_{\mathrm{QCD}}} - \left(2 - \frac{3\beta_0\beta_2}{\beta_1^2} \right) \ln l_{\mu,\Lambda_{\mathrm{QCD}}} + \frac{1}{2} - \frac{\beta_0^2\beta_3}{2\beta_1^3} \right) \\
&+ O\left(\frac{\beta_1^4}{\beta_0^8 l_{\mu,\Lambda_{\mathrm{QCD}}}^4} \right) \Bigg],
\end{aligned}
\tag{B.4}
$$

where $l_{\mu,\mu'}$ is defined by

$$
l_{\mu,\mu'} = \ln(\mu^2/\mu'^2). \tag{B.5}
$$

We numerically use Λ_{QCD} as the value of Particle Data Group [60],

$$
\Lambda_{\mathrm{QCD}} = 340(8)\ \mathrm{MeV}. \tag{B.6}
$$

In general, an off-shell renormalization scheme induces the scale dependence of many quantities as well as the strong coupling constant. Renormalization group equation of a quantity Π is defined by

$$
\mu^2 \frac{\mathrm{d}}{\mathrm{d}\mu^2} \Pi = \Pi\gamma(a_s) = -\Pi \sum_{i=0}^{\infty} \gamma_i a_s^{i+1}, \tag{B.7}
$$

where γ stands for the anomalous dimension of Π. The formal solution of this equation is easily written as

$$
\Pi(\mu') = \exp\left(\int_{a_s(\mu)}^{a_s(\mu')} \frac{\mathrm{d}z}{z} \frac{\gamma(z)}{\beta(z)} \right) \Pi(\mu) = \frac{\rho(a_s(\mu'))}{\rho(a_s(\mu))} \Pi(\mu), \tag{B.8}
$$

here $\rho(z)$ can be analytically calculated as

$$
\begin{aligned}
\rho(z) = z^{\overline{\gamma}_0} \Bigg\{ 1 &+ (\overline{\gamma}_1 - \overline{\beta}_1\overline{\gamma}_0) z + \frac{1}{2} \left[(\overline{\gamma}_1 - \overline{\beta}_1\overline{\gamma}_0)^2 + \overline{\gamma}_2 + \overline{\beta}_1^2\overline{\gamma}_0 - \overline{\beta}_1\overline{\gamma}_1 - \overline{\beta}_2\overline{\gamma}_0 \right] z^2 \\
&+ \Bigg[\frac{1}{6} (\overline{\gamma}_1 - \overline{\beta}_1\overline{\gamma}_0)^3 + \frac{1}{2} (\overline{\gamma}_1 - \overline{\beta}_1\overline{\gamma}_0)(\overline{\gamma}_2 + \overline{\beta}_1^2\overline{\gamma}_0 - \overline{\beta}_1\overline{\gamma}_1 - \overline{\beta}_2\overline{\gamma}_0) \\
&+ \frac{1}{3} (\overline{\gamma}_3 - \overline{\beta}_1^3\overline{\gamma}_0 + 2\overline{\beta}_1\overline{\beta}_2\overline{\gamma}_0 - \overline{\beta}_3\overline{\gamma}_0 + \overline{\beta}_1^2\overline{\gamma}_1 - \overline{\beta}_2\overline{\gamma}_1 - \overline{\beta}_1\overline{\gamma}_2) \Bigg] z^3 + O(z^4) \Bigg\},
\end{aligned}
\tag{B.9}
$$

$$
\overline{\beta}_i = \frac{\beta_i}{\beta_0}, \quad \overline{\gamma}_i = \frac{\gamma_i}{\beta_0}. \tag{B.10}
$$

The anomalous dimension of the scalar and pseudoscalar density is -1 times the mass anomalous dimension $\gamma^m(a_s)$, which is calculated up to the five-loop level [51, 52, 99]. The analytic forms up to the four-loop level are

$$\begin{aligned}
\gamma_0^m =& 1, \\
\gamma_1^m =& \frac{1}{16}\left(\frac{202}{3} - \frac{20}{9} n_f\right), \\
\gamma_2^m =& \frac{1}{64}\left(1249 - \left[\frac{2216}{27} + \frac{160}{3}\zeta_3\right] n_f - \frac{140}{81} n_f^2\right), \\
\gamma_3^m =& \frac{1}{256}\left(\frac{4603055}{162} + \frac{135680}{27} - 8800\zeta_5\right. \\
& - \left[\frac{91723}{27} + \frac{34192}{9}\zeta_3 - 880\zeta_4 - \frac{18400}{9}\zeta_5\right] n_f \\
& \left. + \left[\frac{5242}{243} + \frac{800}{9}\zeta_3 - \frac{160}{3}\zeta_4\right] n_f^2 - \left[\frac{322}{243} - \frac{64}{27}\zeta_3\right] n_f^3\right).
\end{aligned} \tag{B.11}$$

B.2 Scale setting problem

At first, we discuss the perturbative expansion of a scale independent quantity. Using the solution (B.3), we have an arbitrariness about the choice of the renormalization scale of the coupling constant in a perturbative expansion,

$$\Pi = \sum_i c_i(\mu) a_s(\mu)^i = \sum_i c_i(\mu^*) a_s(\mu^*)^i, \tag{B.12}$$

where $c_i(\mu)$ stands for the coefficients of the perturbative expansion with respect to the strong coupling coupling $a_s(\mu)$ renormalized at μ. Although the all order calculation exactly keeps the second equality of this equation, any finite order calculation may violate this exact equality, leading to the dependence of renormalization scale of the coupling constant. If one chooses an extremely bad scale μ_{bad}, the perturbative expansion would clearly has poor convergence such as

$$\Pi = 1 + a_s(\mu_{\text{bad}}) + 10000 a_s(\mu_{\text{bad}})^2. \tag{B.13}$$

On the contrary, there should be the optimal scale in which the unknown higher order contributions are the smallest and the perturbative expansion shows a good convergence.

There have been a lot of studies to search the systematic manner to determine the optimal scale since more than 30 years ago. The most famous one is so-called *the BLM scale* suggested by Brodsky, Lapage and Mackenzie in 1983 [47], which is motivated by an idea of absorbing the higher order contributions of the gluon vacuum polarization into the coupling constant. The scale is chosen such that the perturbative coefficient at a_s^2 becomes independent of number n_f of flavors and, more precisely, the one-loop coefficients β_0 of the beta function. Since this suggestion is suitable only for $O(a_s^2)$ calculation, generalization of the systematic way of the scale setting which is applicable for any order has been studied for a long time.

Inserting (B.9) into (B.8) and expanding into the series of a scale-shifted coupling constant, we obtain the general expression of the perturbative expansion of a scale dependent quantity,

$$\Pi(\mu') = \frac{\rho(a_s(\mu'))}{\rho(a_s(\mu))}\Pi(\mu) = \sum_i c_i(\mu^*, \mu')a_s(\mu^*)^i, \tag{B.14}$$

where $\{c_i(\mu^*, \mu')\}$ stands for the set of perturbative coefficients of $\Pi(\mu')$, which appears with the perturbative coupling $a_s(\mu^*)$. The essence of the equation is that a set of perturbative coefficients at a scale can be converted to that at any scale to the same order. Unlike scale independent quantities, the systematic method of the scale setting for scale dependent quantities has not been investigated.

Appendix C

Lattice action used in this work

C.1 Ginsparg-Wilson relation

It is well known as the name of the Nielsen-Ninomiya theorem [100–102] that chiral symmetry is difficult to realize on the lattice. If the lattice action hold chiral symmetry, at least one of the unexpected properties such as the existence of doublers, the violation of locality or hermiticity of the Dirac operator, appears.

For many years, the Nielsen-Ninomiya theorem was interpreted as the ultimate limitation for a further development of lattice gauge theory until the *natural* chiral symmetry on the lattice was suggested as the satisfaction of the Ginsparg-Wilson relation [45],

$$D\gamma_5 + \gamma_5 D = aD\gamma_5 D, \tag{C.1}$$

where D stands for a Dirac operator. In the continuum theory, a Dirac operator with chiral symmetry obeys (LHS) $= 0$. On the lattice, the interpretation of the chiral symmetry is shifted [103] by $O(a)$ such that the chiral rotation is modified as

$$\begin{aligned} \psi &\to \exp(\mathrm{i}\theta\gamma_5)\psi \quad \Rightarrow \quad \psi \to \exp\left[\mathrm{i}\theta\gamma_5\left(\mathbb{1} - \frac{a}{2}D\right)\right]\psi, \\ \overline{\psi} &\to \overline{\psi}\exp(\mathrm{i}\theta\gamma_5) \quad \Rightarrow \quad \overline{\psi} \to \overline{\psi}\exp\left[\mathrm{i}\theta\gamma_5\left(\mathbb{1} - \frac{a}{2}D\right)\right], \end{aligned} \tag{C.2}$$

with a parameter $\theta \in \mathfrak{u}(N_f)$. If D obeys (C.1), the fermion part of the lattice action $\overline{\psi}D\psi$ is invariant under the modified chiral rotation (C.2). The RHS on the Ginsparg-Wilson relation (C.1) is yielded from the perspective of renormalization group rather than an irrelevant viewpoint just to reproduce, in the continuum limit, the usual chiral symmetry. Therefore it is very natural that the chiral symmetry on the lattice is defined as the satisfaction of the Ginsparg-Wilson relation.

The most simple Ginsparg-Wilson operator is the overlap operator [104], which is given by

$$D_{\mathrm{ov}} = \frac{1}{a}(\mathbb{1} + \gamma_5\,\mathrm{sgn}[H]), \quad H = \gamma_5 A, \tag{C.3}$$

where A denotes some suitable γ_5-hermitian operator usually chosen as Wilson-Dirac operator and H is usually referred to as *kernel*. The sign function is given by $\mathrm{sgn}[X] = X/\sqrt{X^\dagger X}$. The overlap operator satisfies the Ginsparg-Wilson relation and therefore has the exact chiral symmetry on the lattice. Since the overlap formulation takes large computational cost, other kinds of Ginsparg-Wilson formulations such as domain-wall fermion are investigated.

C.2 Domain-wall fermion

Domain-wall fermion [43, 44] provides another kind of the Ginsparg-Wilson fermions and related to the overlap fermion. The domain-wall formulation enhances the time-spatial dimension by introducing the fifth dimension.

The fermion action of the domain-wall fermions is given by

$$S_{\mathrm{DW}}[\Psi, \overline{\Psi}, U] = \sum_{x,y} \sum_{s,r=0}^{L_s-1} \overline{\Psi}(x,s) D_{\mathrm{DW}}(x,s;y,r) \Psi(y,r), \tag{C.4}$$

with the five dimensional fermion field $\Psi_f(x,s)$ and the fifth dimensional coordinates s, r, which run over $0, 1, \ldots, L_s - 1$. Here, we omit the flavor subscription f and consider the one-flavor system. The generalization to N_f-flavor is easy to implement. Using the Wilson-Dirac operator $D_{\mathrm{W}}(-M_0)$ with a large negative mass $-M_0$, the five-dimensional domain-wall operator D_{DW} is defined by

$$D_{\mathrm{DW}} = \begin{pmatrix} D_{||} & -P_- & 0 & \ldots & 0 & mP_+ \\ -P_+ & D_{||} & -P_- & 0 & \ldots & 0 \\ 0 & -P_+ & D_{||} & \ddots & 0 & \vdots \\ \vdots & 0 & \ddots & \ddots & \ddots & \vdots \\ 0 & \ldots & \ddots & -P_+ & D_{||} & -P_- \\ mP_- & 0 & \ldots & 0 & -P_+ & D_{||} \end{pmatrix}, \tag{C.5}$$

where we defined

$$D_{||} = \frac{\mathbb{1}}{a} + D_{\mathrm{W}}(-M_0), \tag{C.6}$$

$$P_\pm = \frac{1 \pm \gamma_5}{2}. \tag{C.7}$$

The mass parameter m stands for the mass of the quark. This matrix is the representation for the fifth dimension and each component has a indices of the usual four-dimensional coordinate as well as of the color and spin. The link fields are not accommodated in the links for the fifth direction.

The four-dimensional Ginsparg-Wilson operator is constructed as follows. Neuberger [105] showed the relation

$$\det[D_{\mathrm{DW}}] = \det[D_{\mathrm{ov}}^{(L_s)}] \det[D_{\mathrm{PV}}], \tag{C.8}$$

where $D_{\rm ov}^{(L_s)}$ becomes $D_{\rm ov}$ in the infinite size of the fifth direction $L_s \to \infty$ and the Pauli-Villars operator $D_{\rm PV}$ is defined by

$$D_{\rm PV} = D_{\rm DW}|_{m=1/a}. \tag{C.9}$$

In order to cancel $\det[D_{\rm PV}]$ in (C.8), He introduced, on the five-dimensional lattice, the pseudofermion fields Φ and $\overline{\Phi}$, which are bosonic but Grassmann-odd and *so called* Pauli-Villars fields, as the action

$$S_{\rm PV}[\Phi, \overline{\Phi}, U] = \sum_{x,y} \sum_{s,r=0}^{L_s-1} \overline{\Phi}(x,s) D_{\rm PV}(x,s;y,r) \Phi(y,r). \tag{C.10}$$

Then, the path integral describes a nearly overlap system,

$$\int \mathcal{D}[\Psi, \overline{\Psi}, \Phi, \overline{\Phi}, U]\, \mathrm{e}^{-S_{\rm DW}-S_{\rm PV}-S_G} = \int \mathcal{D}[U] \det[D_{\rm ov}^{(L_s)}] \mathrm{e}^{-S_G}, \tag{C.11}$$

with any gauge action $S_G[U]$. Neuberger [105] also showed the form

$$\begin{aligned} D_{\rm ov}^{(L_s)} &= \frac{1}{a}\left((1+m) + (1-m)\gamma_5 \tanh\left(\frac{L_s}{2}\widetilde{H}\right)\right) \\ &\to \frac{1}{a}\left((1+m) + (1-m)\gamma_5 \,\mathrm{sgn}\big[\widetilde{H}\big]\right), \end{aligned} \tag{C.12}$$

where the Shamir kernel $\widetilde{H}$ is a variant of H in (C.3),

$$\widetilde{H} = \gamma_5 \frac{D_{\rm W}}{2 + D_{\rm W}}. \tag{C.13}$$

Taking the chiral limit and infinite L_s, we can construct the Ginsparg-Wilson operator with the exact chiral symmetry on the lattice.

C.3 Möbius Domain-wall fermion

We can change the asymptotic form (C.12) by generalizing the domain-wall operator to the Möbius domain-wall operator [40, 41]. The fermion action of Möbius domain-wall fermions is given by

$$S_{\rm MDW} = \sum_{x,y} \sum_{s,r=0}^{L_s-1} \overline{\Psi}(x,s) D_{\rm MDW}(x,s;y,r) \Psi(y,r), \tag{C.14}$$

with the five dimensional fermion field $\Psi(x,s)$ and the Dirac operator,

$$D_{\mathrm{MDW}} = \begin{pmatrix} \widetilde{D}^1 & -P_- & 0 & \dots & 0 & mP_+ \\ -P_+ & \widetilde{D}^2 & -P_- & 0 & \dots & 0 \\ 0 & -P_+ & \widetilde{D}^3 & \ddots & 0 & \vdots \\ \vdots & 0 & \ddots & \ddots & \ddots & \vdots \\ 0 & \dots & \ddots & -P_+ & \widetilde{D}^{L_s-1} & -P_- \\ mP_- & 0 & \dots & 0 & -P_+ & \widetilde{D}^{L_s} \end{pmatrix}. \tag{C.15}$$

The diagonal parts are generalized to

$$\widetilde{D}^s = (D^s_-)^{-1} D^s_+, \tag{C.16}$$

$$\widetilde{D}^s_+ = 1 + b_s D_{\mathrm{W}}(-M_0), \tag{C.17}$$

$$\widetilde{D}^s_- = 1 - c_s D_{\mathrm{W}}(-M_0), \tag{C.18}$$

with the s-dependent parameters b_s, c_s.

The choice of b_s and c_s determines the asymptotic form to the overlap operator and its kernel. The choice is frequently restricted to

$$b_s + c_s = b\omega_s, \ \ b_s - c_s = c, \tag{C.19}$$

with new parameters b, c and ω_s. Then, one can define the Möbius kernel

$$H_{\mathrm{M}} = \gamma_5 \frac{bD_{\mathrm{W}}}{2 + cD_{\mathrm{W}}}. \tag{C.20}$$

Putting $b = 2$ and $c = 0$, the Shamir kernel is reproduced. While b and c determine the kernel of the asymptotic form, the other parameters ω_s determine the accuracy of the approximation of $D^{(L_s)}_{\mathrm{ov}}$ to that in the infinite L_s. Investigating the dependence of the number of the CG iterations and the residual mass [106] on these parameters, we employ the best choice $b = 2, c = 1$ and ω_s such that $D^{(L_s)}_{\mathrm{ov}}$ has an approximate sign function in the form of $\tanh[H_{\mathrm{M}}]$ as in the usual domain-wall case.

C.4 Stout smearing

Gauge configurations generated as Monte-Carlo samples are not sufficiently smooth and therefore may cause a significant source of discretization effects. One can considerably improve such an artifact by smoothing the gauge links. This smoothing procedure is *so called* smearing.

While there are several types of smearing, we here briefly introduce one of them, the stout smearing [76], which is used in this work. The smearing step is defined by

$$U_\mu(x) \to \mathrm{e}^{\mathrm{i}Q_\mu(x)} U_\mu(x), \tag{C.21}$$

where the tangent vector $Q_\mu(x)$ is given by

$$Q_\mu(x) = \frac{\mathrm{i}}{2}\left(\Omega_\mu(x)^\dagger - \Omega_\mu(x) - \frac{1}{3}\mathrm{tr}\left[\Omega_\mu(x)^\dagger - \Omega_\mu(x)\right]\right), \tag{C.22}$$

$$\Omega_\mu(x) = \sum_{\nu\neq\mu} \rho_{\mu\nu} C_{\mu\nu}(x), \tag{C.23}$$

$$\begin{aligned} C_{\mu\nu}(x) = {} & U_\nu(x) U_\mu(x+a\hat{\nu}) U_\nu(x+a\hat{\mu})^\dagger U_\mu(x)^\dagger \\ & + U_\nu(x-a\hat{\nu})^\dagger U_\mu(x-a\hat{\nu}) U_\nu(x+a\hat{\mu}-a\hat{\nu}) U_\mu(x)^\dagger, \end{aligned} \tag{C.24}$$

where the real weight factors $\rho_{\mu\nu}$ are tunable. In this work, we apply the stout smearing only for the fermion-coupled gauge links, *i.e.* stout smearing is not applied for the gauge action. We iterate this process for three steps when we calculate some fermion parts.

Appendix D

Mean field approximation of correlators of domain-wall fermion

Correlators in the coordinate space are given by

$$\Pi_\Gamma(x) = \left\langle \mathrm{Tr}\left[S_F(x)\Gamma S_F(-x)\Gamma\right]\right\rangle, \tag{D.1}$$

where $S_F(x)$ stands for the propagator of the Dirac field. We give the mean field approximation of the domain-wall propagator and its asymptotic form in the long-distance limit. Since the residual mass in this work is mostly negligible, we consider the domain-wall propagator with the infinite size of the fifth direction $L_s \to \infty$. The four-dimensional representation $\widetilde{S}_F^{\mathrm{DW}}(q, m_q)$ of the mean field domain-wall propagator in the momentum space is [44,107,108]

$$\widetilde{S}_F^{\mathrm{DW}}(q, m_q)/a = \frac{-\mathrm{i}u_0 \sum_\mu \gamma_\mu \sin(aq_\mu) + (1 - W\mathrm{e}^{-\alpha})am_q}{-1 + W\mathrm{e}^{\alpha} + (1 - W\mathrm{e}^{-\alpha})(am_q)^2}, \tag{D.2}$$

where W and α are defined by

$$W(q) = 1 - M_0 + \sum_\mu \left(1 - u_0 \cos(aq_\mu)\right), \tag{D.3}$$

$$\cosh\alpha(q) = \frac{1 + W^2 + u_0^2 \sum_\mu \sin^2(aq_\mu)}{2W}, \tag{D.4}$$

with M_0 and u_0 being the domain-wall mass parameter and the fourth root of the plaquette expectation value, respectively. The free propagator is reproduced by putting $u_0 = 1$.

The propagator in the coordinate space is calculated by a numerical Fourier transform in a finite box L^4,

$$S_F^{\mathrm{DW},L^4}(x, m_q) = \frac{1}{L^4}\sum_q \widetilde{S}_F^{\mathrm{DW}}(q)\mathrm{e}^{\mathrm{i}qx}, \tag{D.5}$$

where the sum over q for the periodic boundary condition runs over

$$q \in \left\{ \frac{2\pi}{L}(k_1, k_2, k_3, k_4) \;\middle|\; k_\mu = -\frac{L}{2a} + 1, -\frac{L}{2a} + 2, \cdots, \frac{L}{2a} \right\}, \tag{D.6}$$

The mean field approximation of the propagator of a light quark in a finite box $(m_q L \lesssim 1)$

involves large finite volume effects because quarks are in the deconfining phase. Since the numerical Fourier transform in sufficient large volumes is expensive, we apply a correction for the domain-wall propagator as we applied for the propagators of bosonic fields in Section 3.4,

$$\begin{aligned} S_F^{\mathrm{DW},\infty}(x,m_q) &= S_F^{\mathrm{DW},L^4}(x,m_q) - \sum_{x_0} S_F^{\mathrm{DW},\infty}(x-x_0,m_q) \\ &\simeq S_F^{\mathrm{DW},L^4}(x,m_q) - \sum_{x_0} S_F^{\mathrm{DW,asym}}(x-x_0,m_q), \end{aligned} \tag{D.7}$$

where the sum over x_0 runs over

$$x_0 \in \{(\pm L,0,0,0),(0,\pm L,0,0),(0,0,\pm L,0),(0,0,0,\pm L),(\pm L,\pm L,0,0),\cdots\}, \tag{D.8}$$

and $S_F^{\mathrm{DW,asym}}(x)$ is the asymptotic form of the domain-wall propagator in the long-distance limit in the infinite volume, which is calculated as follows.

The domain-wall propagator in the low-momentum region is calculated by expanding (D.2) at $aq \simeq 0$,

$$\widetilde{S}_F^{\mathrm{DW}}(q,m_q) \xrightarrow{aq\to 0} (1-\delta^2)\frac{-\mathrm{i}u_0\not{q}+m_q'}{u_0^2q^2+{m_q'}^2} + O(\delta^4), \tag{D.9}$$

with

$$\delta = 1 - M_0 + 4(1-u_0), \tag{D.10}$$

$$m_q' = (1-\delta^2)m_q. \tag{D.11}$$

The Fourier transform of this propagator in the infinite volume gives an asymptotic form in the long-distance limit of the domain-wall propagator,

$$S_F^{\mathrm{DW,asym}}(x,m_q) = \frac{1-\delta^2}{u_0^4} S_F^{\mathrm{cont}}(x/u_0,m_q') + O(\delta^4), \tag{D.12}$$

where the Feynman propagator $S_F^{\mathrm{cont}}(x,m_q)$ of a Dirac field in the continuum coordinate space is given [71,72] by

$$\begin{aligned} S_F^{\mathrm{cont}}(x,m_q) &= \int \frac{\mathrm{d}^4q}{(2\pi)^4}\mathrm{e}^{\mathrm{i}qx}\frac{-\mathrm{i}\not{q}+m_q}{q^2+m_q^2} \\ &= \frac{m_q\not{x}}{4\pi^2|x|^3}K_1(m_q|x|) + \frac{m_q^2\not{x}}{8\pi^2x^2}\left[K_0(m_q|x|)+K_2(m_q|x|)\right] + \frac{m_q^2}{4\pi^2|x|}K_1(m_q|x|), \end{aligned} \tag{D.13}$$

with K_i being the modified Bessel functions.

The subtraction by the second line of (D.7) cannot eliminate discretization effects of wrapping effects, *i.e.* the subtraction leaves the discretization effects

$$\sum_{x_0} \big(S_F^{\mathrm{DW},\infty}(x-x_0,m_q) - S_F^{\mathrm{DW,asym}}(x-x_0,m_q)\big), \tag{D.14}$$

which are suppressed in large volumes. We observe that these discretization effects are sufficiently small when the calculation is done with $m_qL \gtrsim 1$.

Appendix E

Least squared method

The least squared method, which is usually called χ^2 fitting, is very convenient to calculate the best estimate of some parameters in a model from measured data. In this appendix, we review this method.

E.1 Basics

First of all, we consider a data set $\{(x_k, y_k, \sigma_k)|k = 1, 2, \cdots, N_s\}$, where x_k and y_k are a set of measured values labeled by k and we assume the distribution of y_k follows a Gaussian with the width[1] σ_k. A sample (x_k, y_k, σ_k) of the data means that if one measures y at a parameter x_k, then the probability distribution of y is estimated as

$$\mathcal{P}_{x_k}(y) = \frac{1}{\sqrt{2\pi}\sigma_k} \mathrm{e}^{-(y-y_k)^2/2\sigma_k^2}. \tag{E.1}$$

It also means, from another point of view, that if one knows the central value of y and its uncertainty as a function of x such that

$$y = f(x) \pm \sigma(x), \tag{E.2}$$

then the probability of measuring y_k at x_k is given by

$$\mathcal{P}_{x_k}(y_k) = \frac{1}{\sqrt{2\pi}\sigma(x_k)} \mathrm{e}^{-(y_k - f(x_k))^2/2\sigma(x_k)^2}. \tag{E.3}$$

The uncertainty $\sigma(x_k)$ at x_k is usually assumed as the statistical error of y_k, *i.e.* $\sigma(x_k) = \sigma_k$.

Taking the product of eq. (E.3) for all k, we obtain the probability of getting the data set $\{(x_k, y_k)|k = 1, 2, \cdots, N_s\}$ as

$$\mathcal{P}(\{(x_k, y_k)|k = 1, 2, \cdots, N_s\}) = \prod_{k=1}^{N_s} \mathcal{P}_{x_k}(y_k) = \left[\prod_{k=1}^{N_s} \sqrt{\frac{w_k}{2\pi}}\right] \mathrm{e}^{-\chi^2/2}, \tag{E.4}$$

---

[1] We here do not consider the case with the error of x_k.

where we defined χ^2 and weight w_k as

$$\chi^2 = \sum_{k=1}^{N_s} w_k \big(y_k - f(x_k)\big)^2, \tag{E.5}$$

$$w_k = \frac{1}{\sigma_k^2}. \tag{E.6}$$

In more general, the measured data set could have the correlations between (x_k, y_k, σ_k) and $(x_{k'}, y_{k'}, \sigma_{k'})$ for different k, k'. Considering this case, we modify χ^2 in (E.4) as

$$\chi^2 = \sum_{k,k'=1}^{N_s} \big(y_k - f(x_k)\big) w_{kk'} \big(y_{k'} - f(x_{k'})\big), \tag{E.7}$$

where the (inverse) covariance $w_{kk'}$ is defined by

$$(w^{-1})_{kk'} = \frac{1}{N_s - 1}\big(\langle y_k y_{k'}\rangle - \langle y_k\rangle\langle y_{k'}\rangle\big). \tag{E.8}$$

In this work, lattice data are analyzed based on the bootstrap method, which essentially considers the correlation between the data. Since we perform the non-linear fit for the ALEPH data with a consideration of the correlation, we introduce the generalization to such a case.

Let us consider the case in which $f(x)$ is parametrized by finite number of unknown parameters $\vec{a} = (a_1, a_2, \cdots, a_m)$. The least χ^2 fitting is useful to determine these parameters from a data set. If χ^2 takes the minimal value, the probability in (E.4) become the maximal value. The best estimate of parameters $\vec{a} = (a_1, a_2, \cdots, a_m)$ is determined such that the probability $\mathcal{P}(\{(x_k, y_k) | k = 1, 2, \cdots, N_s\})$ takes the maximal value. Consequently, the best choice of $\vec{a}$ minimizes χ^2 and therefore satisfies

$$\frac{\partial \chi^2}{\partial a_j} = 0, \quad j = 1, 2, \cdots, m. \tag{E.9}$$

The uncertainty of an arbitrary function $\bar{f}(a, y)$ of the fit parameters a and the data values y is written as

$$(\delta \bar{f})^2 = \sum_{k=1}^{N_s} \frac{1}{w_k} \left(\frac{\delta \bar{f}}{\delta y_k}\right)^2, \tag{E.10}$$

or more generally,

$$(\delta \bar{f})^2 = \sum_{k,k'=1}^{N_s} (w^{-1})_{kk'} \frac{\delta \bar{f}}{\delta y_k}\frac{\delta \bar{f}}{\delta y_{k'}}, \tag{E.10$'$}$$

where

$$\frac{\delta \bar{f}}{\delta y_k} = \sum_j \frac{\delta a_j}{\delta y_k} \bar{g}_j + \bar{h}_k. \tag{E.11}$$

with

$$\bar{g}_j(\vec{a}, y) = \frac{\partial \bar{f}(\vec{a}, y)}{\partial a_j}, \;\; \bar{h}_k(\vec{a}, y) = \frac{\partial \bar{f}(\vec{a}, y)}{\partial y_k}. \tag{E.12}$$

Putting $\bar{f}(\vec{a}, y) = a_j$, we can obtain the uncertainty of the fit parameter a_j.

In the following, we discuss some examples and a generalization to the global fit.

E.2 Case of linear parameters

As a pedagogical example, we first discuss the case in which the fit function $f(a; x)$ is linear with respect to the parameters $\vec{a} = (a_1, a_2, \cdots, a_m)$, *i.e.* $f(\vec{a}, x)$ can be written as

$$f(\vec{a}; x) = \sum_{j=0}^{m} a_j g_j(x), \tag{E.13}$$

with $g_j(x)$ being independent of a. Then the minimizing condition (E.9) becomes

$$\frac{1}{2}\frac{\partial \chi^2}{\partial a_j} = -\sum_{k=1}^{N_s} w_k (y_k - f(x_k)) g_j(x_k) = 0, \tag{E.14}$$

$$\therefore \sum_{j'=1}^{m} \left[\sum_{k=0}^{N_s} w_k g_j(x_k) g_{j'}(x_k) \right] a_{j'} = \sum_{k=1}^{N_s} w_k y_k g_j(x_k). \tag{E.15}$$

Using the matrix notation, this condition is simply written as

$$\hat{\alpha}\vec{a} = \vec{\beta}, \tag{E.16}$$

where

$$\alpha_{jj'} = \sum_{k=0}^{N_s} w_k g_j(x_k) g_{j'}(x_k), \quad \beta_j = \sum_{k=1}^{N_s} w_k y_k g_j(x_k). \tag{E.17}$$

The best estimate of a is obtained as

$$\vec{a} = \hat{\alpha}^{-1}\vec{\beta}. \tag{E.18}$$

Then, the uncertainty of a function $\bar{f}(\vec{a}, y)$ defined by (E.10) is calculated as

$$(\delta \bar{f})^2 = \sum_{jj'=1}^{m} (\alpha^{-1})_{jj'} \bar{g}_j \bar{g}_{j'} + 2 \sum_{j,j'=1}^{m} \sum_{k=1}^{N_s} (\alpha^{-1})_{jj'} g_{j'}(x_k) \bar{g}_j \bar{h}_k + \sum_{k=1}^{N_s} \frac{1}{w_k} \bar{h}_k^2. \tag{E.19}$$

Putting $\bar{f}(\vec{a}, y) = a_j$, we obtain the uncertainty of the fit parameters as

$$(\delta a_j)^2 = (\alpha^{-1})_{jj}. \tag{E.20}$$

E.3 Case of non-linear parameters

In more general cases in which $f(x)$ is not linear in the parameters $\vec{a}$, such as the fitting of an exponential dumping $f(t) = z_0 \mathrm{e}^{-mt}$, we need to employ another approach based on the gradient method, which is to minimize a function by shifting the free parameters iteratively. There are a lot of algorithms of the gradient method. In this section, we review *the Levenberg-Marquardt method*, which is the most widely used method, after briefly introducing the underlying two gradient methods, *the steepest descent method* and *the Gauss-Newton method*. We here add the further generalizations to the case of correlated data y_k leading to non-vanishing off-diagonal component of $w_{kk'}$ as we mentioned in the beginning of this appendix. This is because we consider in this work the correlated fit for the ALEPH data.

E.3.1 Steepest descent method

In the steepest descent method, the free parameters are updated by the gradient of χ^2 using a positive parameter. Being updated iteratively, the parameters are expected to reach the point to minimize χ^2.

Generalizing $g_j(x)$ in the previous section to

$$g_j(\vec{a};x) = \frac{\partial f(\vec{a};x)}{\partial a_j}, \tag{E.21}$$

the gradient of χ^2 with respect to the free parameters $\vec{a}$ become the same form as (E.14). Applying the recurrence relation

$$\vec{a}_{t+1} = \vec{a}_t + \lambda^{-1} \sum_{k=1}^{N_s} w_k (y_k - f(\vec{a}_t;x_k)) \vec{g}(\vec{a}_t;x_k), \tag{E.22}$$

with a input positive parameter[2] λ and an initial free parameters $\vec{a}_0$, the sequence of parameters $\vec{a}_t$ is expected to converge on the best solution in the limit $t \to \infty$. The generalization of (E.22) to the correlated case is written as

$$\vec{a}_{t+1} = \vec{a}_t + \lambda^{-1} \sum_{k,k'=1}^{N_s} w_{kk'} (y_k - f(\vec{a}_t;x_k)) \vec{g}(\vec{a}_t;x_{k'}). \tag{E.22$'$}$$

E.3.2 Gauss-Newton method

In the Gauss-Newton method, we have an assumption that the initial free parameters $\vec{a}_0$ are sufficiently close to the best solution which minimizes χ^2. The Taylor expansion of $f(\vec{a};x)$ at $\vec{a}_t$ is

$$f(\vec{a};x) = f(\vec{a}_t;x) + \delta\vec{a} \cdot \vec{g}(\vec{a}_t;x) + O(|\delta\vec{a}|^2), \tag{E.23}$$

---

[2] In (E.22), we denote inverse to λ in order to generalize straightforwardly the steepest descent method to the Levenberg-Marquardt method.

where $\vec{\delta a} = \vec{a} - \vec{a}_t$. Neglecting the higher orders $O(|\delta\vec{a}|^2)$, the problem can be treated similarly as the case of linear parameters, *i.e.* we employ the algorithm to update the free parameter,

$$f(\vec{a}_{t+1}; x) = f(\vec{a}_t; x) + \delta\vec{a}_t \cdot \vec{g}(\vec{a}_t; x), \;\; \delta\vec{a}_t = \vec{a}_{t+1} - \vec{a}_t. \tag{E.24}$$

Following the same procedure as in the previous section for $\delta\vec{a}_t$, we obtain the recurrence relation

$$\vec{a}_{t+1} = \vec{a}_t + \hat{\alpha}_t^{-1}\vec{\beta}_t, \tag{E.25}$$

with

$$\hat{\alpha}_t = \sum_{k=1}^{N_s} w_k \vec{g}(\vec{a}_t; x_k)\vec{g}(\vec{a}_t; x_k)^T, \;\; \vec{\beta}_t = \sum_{k=1}^{N_s} w_k(y_k - f(\vec{a}_t; x_k))\vec{g}(\vec{a}_t; x_k), \tag{E.26}$$

or

$$\hat{\alpha}_t = \sum_{k,k'=1}^{N_s} w_{kk'} \vec{g}(\vec{a}_t; x_k)\vec{g}(\vec{a}_t; x_{k'})^T, \;\; \vec{\beta}_t = \sum_{k,k'=1}^{N_s} w_{kk'}(y_k - f(\vec{a}_t; x_k))\vec{g}(\vec{a}_t; x_{k'}), \tag{E.26$'$}$$

in more general.

E.3.3 Levenberg-Marquardt method

The steepest descent method and the Gauss-Newton method have some different characteristics. The essence of the former is to reduce χ^2 in the leading order of $\delta\vec{a}_t$, while the latter requires χ^2 not to change in the leading order of $\delta\vec{a}_t$, *i.e.*

- Steepest descent method: $\chi^2(\vec{a}_{t+1}) - \chi^2(\vec{a}_t) < 0$ at $O(|\delta\vec{a}_t|)$.
- Gauss-Newton method: $\chi^2(\vec{a}_{t+1}) - \chi^2(\vec{a}_t) = O(|\delta\vec{a}_t|^2)$.

The former needs a lot of iterations to reach the stationary point of χ^2 after $\vec{a}_t$ gets close to the best solution, though it is useful to search roughly the best solution to minimize χ^2. On the other hand, the latter can rapidly converge the free parameter if the initial input parameter $\vec{a}_0$ is sufficiently close to the stationary point. This method also has a disadvantage that the stationary point found by this method is not necessarily the best solution because this method does not require χ^2 to decrease. The possible candidates are maximum points, saddle points, and other types of stationary points as well as the minimizing point.

The Levenberg-Marquardt method is a hybrid version of these two methods. In this method, the steepest descent method is dominantly applied if the parameter $\vec{a}_t$ is away from the solution, while it is suppressed as the parameter approaches the solution and the Gauss-Newton method dominates the algorithm.

The Levenberg-Maquardt method unifies and modifies the recurrence relations (E.22) and (E.26) to

$$\vec{a}^*_{t+1} = \vec{a}_t + \hat{\alpha}'^{-1}_t \vec{\beta}_t, \tag{E.27}$$

$$\vec{a}_{t+1} = a^*_{t+1} \qquad \text{if } \chi^2(\vec{a}^*_{t+1}) < \chi^2(\vec{a}_t), \tag{E.28}$$

$$\vec{a}_{t+1} = a_t \qquad \text{if } \chi^2(\vec{a}^*_{t+1}) > \chi^2(\vec{a}_t), \tag{E.29}$$

where $\hat{\alpha}'_t$ is defined by

$$\hat{\alpha}'_t = \hat{\alpha}_t + \lambda_t \mathbb{1}. \tag{E.30}$$

The parameter λ_t is updated simultaneously with $\vec{a}_t$. The update (E.27) with an extremely large λ_t is mostly based on the steepest descent method, while that with very small λ_t is dominated by the Gauss-Newton method.

Algorithmically, the iteration stops if

$$0 \leq 1 - \frac{\chi^2(\vec{a}_{t+1})}{\chi^2(\vec{a}_t)} < \epsilon \tag{E.31}$$

with a small input parameter ϵ. If $\chi^2(\vec{a}_{t+1}) - \chi^2(\vec{a}_t) < 0$ without satisfying the stopping condition, we would better switch the dominance of the algorithm from the steepest descent to the Gauss-Newton method in the next update process. Therefore, the algorithm is programed to decrease λ_t in this case. If $\chi^2(a_{t+1}) - \chi^2(a_t) > 0$, on the other hand, it means λ_t was so small that the contribution of $O(|\delta\vec{a}_t|^2)$ is large and $\vec{a}^*_{t+1}$ is too much away from $\vec{a}_t$. Therefore we would better retry with larger λ_t. Consequently the rule to update λ_t is given as

$$\lambda_{t+1} = \kappa^{2\theta(\chi^2(\vec{a}_t) - \chi^2(\vec{a}^*_{t+1}))-1} \lambda_t, \tag{E.32}$$

with the step function θ and a power factor $\kappa(> 1)$, which is tipically set to ~ 10. In some case, the upper and lower bound of λ_t, $\lambda_{\rm max}$ and $\lambda_{\rm min}$, are introduced to avoid other unexpected situations. These are typically set to $\lambda_{\rm max} \sim \lambda^{-1}_{\rm min} \sim 10^7$.

The summary of the algorithm is as follows.

1. Input the initial parameter $\vec{a}_0$ and λ_0, the stopping condition ϵ, the power factor κ, and optionally the upper and lower bounds of λ_t, $\lambda_{\rm max}$ and $\lambda_{\rm min}$.

2. Calculate $\vec{a}^*_{t+1}$ using (E.27).

3. Evaluate $\chi^2(a^*_{t+1})$. If the stopping condition (E.31) is satisfied, the iteration is finished and output $\vec{a}^*_{t+1}$ as the fit result. Otherwise, the iteration continues as follows.

    - If $\chi^2(\vec{a}_{t+1}) < \chi^2(\vec{a}_t)$, $\vec{a}_t$ and λ_t are updated as

    $$\vec{a}_{t+1} = \vec{a}^*_{t+1}, \quad \lambda_{t+1} = \max\left\{\frac{\lambda_t}{\kappa}, \lambda_{\rm min}\right\}.$$

- If $\chi^2(\vec{a}_{t+1}) < \chi^2(\vec{a}_t)$, $\vec{a}_t$ and λ_t are updated as

$$\vec{a}_{t+1} = \vec{a}_t, \ \ \lambda_{t+1} = \min\left\{\lambda_t \kappa, \lambda_{\max}\right\}.$$

4. Go back to 2. and repeat the processes 2. and 3.

The error estimate is also more complicated than that for the case of linear parameters due to the non-vanishing a-dependence of $\hat{\alpha}$. The starting point of the error estimation is not changed from (E.10), whose differential term $\partial a_j/\partial y_k$ have to be calculated more generally. Around the optimal a, the LHS on the minimizing condition (E.9) can be expanded as

$$\frac{\partial \chi^2}{\partial a_j} = \sum_{j'=1}^{m} \frac{\partial^2 \chi^2}{\partial a_j \partial a_{j'}} \delta a_{j'} + \sum_{k=1}^{N_s} \left[\frac{\partial^2 \chi^2}{\partial a_j \partial y_k} \delta y_k + \frac{\partial^2 \chi^2}{\partial a_j \partial w_k} \delta w_k \right]. \tag{E.33}$$

Here, w_k is independent of y_k. The minimizing condition therefore yields

$$\frac{\delta a_j}{\delta y_k} = \frac{1}{2} \sum_{j'=1}^{m} (D^{-1})_{jj'} \frac{\partial^2 \chi^2}{\partial a_{j'} \partial y_k} = - \sum_{j'=1}^{m} (D^{-1})_{jj'} w_k g_{j'}(x_k), \tag{E.34}$$

or

$$\frac{\delta a_j}{\delta y_k} = - \sum_{j'=1}^{m} (D^{-1})_{jj'} \sum_{k'=1}^{N_s} w_{kk'} g_{j'}(x_{k'}), \tag{E.34$'$}$$

where we defined

$$D_{jj'} = \frac{1}{2} \frac{\partial^2 \chi^2}{\partial a_j \partial a_{j'}}, \tag{E.35}$$

and the second equality is derived from the minimizing condition (E.14). Inserting (E.34) into the relation for the error estimation, (E.10)–(E.12), we obtain

$$(\delta \bar{f})^2 = \vec{g}^{\,T} \hat{D}^{-1} \hat{\alpha} \hat{D}^{-1} \vec{g} + 2 \vec{g}^{\,T} \hat{D}^{-1} \sum_{k=1}^{N_s} \vec{g}(x_k) \bar{h}_k + \sum_{k=1}^{N_s} \frac{1}{w_k} \bar{h}_k^2, \tag{E.36}$$

where $\hat{\alpha}$ is defined as (E.26$^{(\prime)}$) with $a_t = a$, which is the fit result. This expression is realized even for the case of correlated data. The uncertainty of the fit parameter is therefore

$$(\delta a_j)^2 = (\hat{D}^{-1} \hat{\alpha} \hat{D}^{-1})_{jj}. \tag{E.37}$$

E.4 Generalization to global fit and example

The above cases we have discussed always have only one data set $\{(x_k, y_k, w_k) | k = 1, 2, \ldots, N\}$, in which the truth value of y is expected to depends only on x. In these cases, the fit parameters can be determined uniquely. As a generalization of such cases, we can consider the case in which there are two or more data sets such that fit parameters and/or the form of the fit function depend on the data set. If we have several data sets which are theoretically related each other such as the case in which there are several data set with different input quark masses, we would better perform χ^2 fitting simultaneously.

There are $N_0 \times N_1 \times \cdots N_n$ data sets

$$\left\{ \left(x_k^{(s_0,s_1,\cdots,s_n)}, y_k^{(s_0,s_1,\cdots,s_n)}, w_k^{(s_0,s_1,\cdots,s_n)} \right) \middle| k = 1,2,\cdots,N_s^{(s_0,s_1,\cdots,s_n)}, s_i = 1,2,\cdots,N_i \right\}, \tag{E.38}$$

For example, each of s_i stands for the index of the bare coupling β, smearing parameter, input mass, and so on. For simplicity, we denote $(s_0, s_1, \cdots, s_n) = \vec{s}$,

$$\left\{ \left(x_k^{(\vec{s})}, y_k^{(\vec{s})}, w_k^{(\vec{s})} \right) \middle| k = 1,2,\cdots,N_s^{(\vec{s})}, s_i = 1,2,\cdots,N_i \right\}, \tag{E.39}$$

The corresponding fit functions are

$$f_{\vec{s}}(\vec{a}, \vec{b}^{s_1}, \vec{b}^{s_2}, \cdots, \vec{b}^{s_n}; x) = f_{\vec{s}}\Big(a_1, \cdots, a_{m_0}, (b_1^{s_i}, \cdots, b_{m_i}^{s_i})_{i=1}^{n}; x\Big), \tag{E.40}$$

where a is common for each data set and $b^{(s_i)}$ is individual with respect to the data label s_i[3]. Note that the fit parameters do not include the data label s_0 since the difference of data induced by the difference of s_0 is theoretically controlled using some input parameters.

The generalized χ^2 is given by

$$\chi^2 = \sum_{\vec{s}} \sum_{k=1}^{N_s^{(\vec{s})}} w_k^{(\vec{s})} \left(y_k^{(\vec{s})} - f_{\vec{s}}(x_k^{(\vec{s})}) \right)^2, \tag{E.41}$$

or

$$\chi^2 = \sum_{\vec{s},\vec{s}'} \sum_{k=1}^{N_s^{(\vec{s})}} \sum_{k'=1}^{N_s^{(\vec{s}')}} w_{kk'}^{(\vec{s},\vec{s}')} \left(y_k^{(\vec{s})} - f_{\vec{s}}(x_k^{(\vec{s})}) \right) \left(y_{k'}^{(\vec{s}')} - f_{\vec{s}'}(x_{k'}^{(\vec{s}')}) \right), \tag{E.41$'$}$$

in more general. The corresponding minimizing conditions and the error estimation are as follows.

$$\frac{\partial \chi^2}{\partial a_j} = 0, \quad j = 1,2,\cdots,m_0, \tag{E.42}$$

$$\frac{\partial \chi^2}{\partial b_j^{s_i}} = 0, \quad j = 1,2,\cdots,m_i,\ i = 1,2,\cdots,n, \tag{E.43}$$

$$(\delta \bar{f})^2 = \sum_{\vec{s}} \sum_{k=1}^{N_s^{(\vec{s})}} \frac{1}{w_k^{(\vec{s})}} \left(\frac{\delta \bar{f}}{\delta y_k^{(\vec{s})}} \right)^2. \tag{E.44}$$

For the case of correlated data, the errors is estimated as

$$(\delta \bar{f})^2 = \sum_{\vec{s},\vec{s}'} \sum_{k=1}^{N_s^{(\vec{s})}} \sum_{k'=1}^{N_s^{(\vec{s}')}} (w^{-1})_{kk'}^{(\vec{s},\vec{s}')} \frac{\delta \bar{f}}{\delta y_k^{(\vec{s})}} \frac{\delta \bar{f}}{\delta y_{k'}^{(\vec{s}')}}, \tag{E.44$'$}$$

---

[3] In more general, number m_i of $b^{(s_i)}$ could depend on s_i. We do not consider such cases here.

Here, we defined

$$\frac{\delta \bar{f}}{\delta y_k^{(\vec{s})}} = \sum_{j=1}^{m_0} \frac{\delta a_j}{\delta y_k^{(\vec{s})}} \bar{g}_{0,j} + \sum_{i=1}^{n} \sum_{s_i=1}^{N_i} \sum_{j=1}^{m_i} \frac{\delta b_j^{s_i}}{\delta y_k^{(\vec{s})}} \bar{g}_{i,j}^{(s_i)} + \bar{h}_k^{(\vec{s})}. \tag{E.45}$$

with

$$\bar{g}_{0,j}(a,b,y) = \frac{\partial \bar{f}}{\partial a_j}, \;\; \bar{g}_{i,j}^{(s_i)}(a,b,y) = \frac{\partial \bar{f}}{\partial b_j^{(s_i)}}, \;\; \bar{h}_k^{(\vec{s})}(a,b,y) = \frac{\partial \bar{f}}{\partial y_k^{(\vec{s})}}. \tag{E.46}$$

In the rest of this section, we discuss some examples used in this work.

E.4.1 $n = 0$ with linear parameters

At first, we consider the most trivial case with $n = 0$ and linear parameters. In this case, only the common parameters $\vec{a}$ exist. This fit is applied to the extrapolation of the $V + A$ and $V - A$ correlators in Section 5.1. In this case, the fit function and χ^2 are written as

$$f_s(x) = \sum_{j=1}^{m} a_j g_j^{(s)}(x), \tag{E.47}$$

$$\chi^2 = \sum_{s=1}^{N} \sum_{k=1}^{N_s^{(s)}} w_k^{(s)} \left(y_k^{(s)} - f_s(x_k^{(s)}) \right)^2. \tag{E.48}$$

Here, the subscript 0 on $s, m, \vec{g}$, and N is omitted. The minimizing condition (E.42) yields the same result as in non-simultaneous cases, $\vec{a} = \hat{\alpha}^{-1}\vec{\beta}$ and $(\delta \bar{f})^2 = \vec{\bar{g}}^T \hat{\alpha}^{-1} \vec{\bar{g}} + \ldots$, with minor modifications

$$\hat{\alpha} = \sum_{s=1}^{N} \sum_{k=1}^{N_s^{(s)}} w_k^{(s)} \vec{g}^{(s)}(x_k^{(s)}) \vec{g}^{(s)}(x_k^{(s)})^T, \;\; \vec{\beta} = \sum_{s=1}^{N} \sum_{k=1}^{N_s^{(s)}} w_k^{(s)} (y_k^{(s)} - f_s(x_k^{(s)})) \vec{g}^{(s)}(x_k^{(s)}). \tag{E.49}$$

E.4.2 $n = 1$ and $m_0 = 0$ with non-linear parameters and correlated data

Next, we discuss the case of $n = 1$ and $m_0 = 0$, in which there is no common parameter $\vec{a}$ but the fit is done to minimize χ^2 simultaneously for all fit parameters[4] $\vec{b}^s, \; s = 1, 2, \cdots, N$. This case is trivially treated in the same manner as in non-simultaneous cases as long as the correlation among data of different s_1 is absent. However, we perform in Section 5.1 the global fit for the ALEPH data including such a correlation between the vector and axial-vector channels. Since the resonance based model to take account of the duality violation needs a non-linear fit for the ALEPH data, we consider some non-linear parameters.

---

[4] The subscript 1 on s is omitted and that on m, $\vec{g}$ and N will be omitted in this subsection.

Reflecting the policy on the non-linear fit explained in the previous section, the modification is done just as a replacement of (E.26′) with

$$\begin{aligned}\hat{\alpha}_t^{(s,s')} &= \sum_{k=1}^{N_s^{(s)}} \sum_{k'=1}^{N_s^{(s')}} w_{kk'}^{(s,s')} \vec{g}^{(s)}\big(\vec{b}_t^s; x_k^{(s)}\big) \vec{g}^{(s')}\big(\vec{b}_t^{s'}; x_{k'}^{(s')}\big)^T, \\ \vec{\beta}_t^{(s)} &= \sum_{s'=1}^{N} \sum_{k=1}^{N_s^{(s)}} \sum_{k'=1}^{N_s^{(s')}} w_{kk'}^{(s,s')} \left(y_k^{(s)} - f_s\big(\vec{b}_t^s; x_k^{(s)}\big)\right) \vec{g}^{(s')}\big(\vec{b}_t^{s'}; x_{k'}^{(s')}\big),\end{aligned} \tag{E.50}$$

where

$$g_j^{(s)}\big(\vec{b}^s; x\big) = \frac{\partial f_s\big(\vec{b}^s; x\big)}{\partial b_j^s}. \tag{E.51}$$

Here $\hat{\alpha}$ and $\vec{\beta}$ with the superscripts (s, s') and (s) stand for a part of the enhanced matrix and vector, *i.e.* the size of $\hat{\alpha}$ and $\vec{\beta}$ is Nm. The recurrence relation (E.27) is modified to

$$\vec{b}_{t+1}^{*,s} = \vec{b}_t^s + (\hat{\alpha}'^{-1})^{(s,s')} \vec{\beta}_t^{(s')}. \tag{E.52}$$

The error is estimated as follows. The b_j^s-differential $\partial\chi^2/\partial b_j^s = -2\vec{\beta}_{t\to\infty}^{(s)}$ is written as,

$$\frac{\partial \chi^2}{\partial b_j^s} = \sum_{s'=1}^{N} \left[\sum_{j'=1}^{m} \frac{\partial^2 \chi^2}{\partial b_j^s \partial b_{j'}^{s'}} \delta b_{j'}^{s'} + \sum_{k=1}^{N_s^{(s')}} \frac{\partial^2 \chi^2}{\partial b_j^s \partial y_k^{(s')}} \delta y_k^{(s')} + \cdots \right], \tag{E.53}$$

with $m = m_1$. This differential is also written in another form,

$$\frac{\partial \chi^2}{\partial b_j^s} = -2 \sum_{s'=1}^{N} \sum_{k=1}^{N_s^{(s)}} \sum_{k'=1}^{N_s^{(s')}} w_{kk'}^{(s,s')} g_j^{(s)}(x_k^{(s)}) \left(y_{k'}^{(s')} - f_{s'}(x_{k'}^{(s')})\right). \tag{E.54}$$

Therefore the minimizing condition yields

$$\begin{aligned}\frac{\delta b_j^s}{\delta y_k^{s'}} &= \frac{1}{2} \sum_{s''=1}^{N} \sum_{j'}^{m} (D^{-1})_{jj'}^{(s,s'')} \frac{\partial^2 \chi^2}{\partial b_{j'}^{s''} \partial y_k^{(s')}} \\ &= - \sum_{s''=1}^{N} \sum_{j'}^{m} (D^{-1})_{jj'}^{(s,s'')} \sum_{k'=1}^{N_s^{(s'')}} w_{kk'}^{(s',s'')} g_{j'}^{(s'')}\big(\vec{b}^{s''}; x_{k'}^{(s'')}\big),\end{aligned} \tag{E.55}$$

where

$$D_{jj'}^{(s,s')} = \frac{1}{2} \frac{\partial^2 \chi^2}{\partial b_j^s \partial b_{j'}^{s'}} = \alpha_{jj'}^{(s,s')} - \delta_{ss'} \sum_{k,k'=1}^{N_s^{(s)}} w_{kk'}^{(s,s)} \frac{\partial^2 f_s(x_k^{(s)})}{\partial b_j^s \partial b_{j'}^s} \left(y_{k'}^{(s)} - f_s(s_{k'}^{(s)})\right). \tag{E.56}$$

The uncertainty of an arbitrary function $\bar{f}(b, y)$ is

$$
\begin{aligned}
(\delta \bar{f})^2 &= \sum_{s,s'=1}^{N} \sum_{k=1}^{N_s^{(s)}} \sum_{k'=1}^{N_s^{(s')}} (w^{-1})_{kk'}^{(s,s')} \frac{\delta \bar{f}}{\delta y_k^{(s)}} \frac{\delta \bar{f}}{\delta y_{k'}^{(s')}} \\
&= \sum_{s,s',s'',s'''=1}^{N} \vec{g}^{(s),T} (\hat{D}^{-1})^{(s,s')} \hat{\alpha}^{(s',s'')} (\hat{D}^{-1})^{(s'',s''')} \vec{g}^{(s''')} \\
&\quad - 2 \sum_{s,s'=1}^{N} \vec{g}^{(s),T} (\hat{D}^{-1})^{(s,s')} \sum_{k=1}^{N_s^{(s')}} \vec{g}^{(s')}(x_k^{(s')}) \bar{h}_k^{(s')} \\
&\quad + \sum_{s,s'=1}^{N} \sum_{k=1}^{N_s^{(s)}} \sum_{k'=1}^{N_s^{(s')}} \bar{h}_k^{(s)} (w^{-1})_{kk'}^{(s,s')} \bar{h}_{k'}^{(s')},
\end{aligned} \tag{E.57}
$$

and therefore

$$
(\delta b_j^s)^2 = \left[\sum_{s',s'',s'''=1}^{N} (\hat{D}^{-1})^{(s,s')} \hat{\alpha}^{(s',s'')} (\hat{D}^{-1})^{(s'',s)} \right]_{jj} . \tag{E.58}
$$

E.4.3 $n = 2$ with linear parameters

Lastly, let us consider the case of linear parameters with $n = 2$, which is applied in Chapter 4. Here, we do not consider the correlation between data. The fit function is written as

$$
f_{\vec{s}}(x) = \sum_{j=1}^{m_0} a_j g_{0,j}^{(\vec{s})}(x) + \sum_{j=1}^{m_1} b_j^{s_1} g_{1,j}^{(\vec{s})}(x) + \sum_{j=1}^{m_2} b_j^{s_2} g_{2,j}^{(\vec{s})}(x). \tag{E.59}
$$

The first minimizing condition (E.42) is calculated as

$$
\begin{aligned}
&\sum_{j'=1}^{m_0} \left[\sum_{\vec{s}} \sum_{k=1}^{N_s^{(\vec{s})}} w_k^{(\vec{s})} g_{0,j}^{(\vec{s})}(x_k^{(\vec{s})}) g_{0,j'}^{(\vec{s})}(x_k^{(\vec{s})}) \right] a_{j'} \\
&+ \sum_{s_1=1}^{N_1} \sum_{j'=1}^{m_0} \left[\sum_{s_0=1}^{N_0} \sum_{s_2=1}^{N_2} \sum_{k=1}^{N_s^{(\vec{s})}} w_k^{(\vec{s})} g_{0,j}^{(\vec{s})}(x_k^{(\vec{s})}) g_{1,j'}^{(\vec{s})}(x_k^{(\vec{s})}) \right] b_{j'}^{s_1} \\
&+ \sum_{s_2=1}^{N_2} \sum_{j'=1}^{m_0} \left[\sum_{s_0=1}^{N_0} \sum_{s_1=1}^{N_1} \sum_{k=1}^{N_s^{(\vec{s})}} w_k^{(\vec{s})} g_{0,j}^{(\vec{s})}(x_k^{(\vec{s})}) g_{2,j'}^{(\vec{s})}(x_k^{(\vec{s})}) \right] b_{j'}^{s_2} = \sum_{\vec{s}} \sum_{k=1}^{N_s^{(\vec{s})}} w_k^{(\vec{s})} y_k^{(\vec{s})} g_{0,j}^{(\vec{s})}(x_k^{(\vec{s})}).
\end{aligned} \tag{E.60}
$$

The second condition (E.43) is

$$
\begin{aligned}
&\sum_{j'=1}^{m_0} \left[\sum_{s_0=1}^{N_0} \sum_{s_{\bar{i}}=1}^{N_{\bar{i}}} \sum_{k=1}^{N_s^{(\vec{s})}} w_k^{(\vec{s})} g_{i,j}^{(\vec{s})}(x_k^{(\vec{s})}) g_{0,j'}^{(\vec{s})}(x_k^{(\vec{s})}) \right] a_{j'} \\
&+ \sum_{j'=1}^{m_i} \left[\sum_{s_0=1}^{N_0} \sum_{s_{\bar{i}}=1}^{N_{\bar{i}}} \sum_{k=1}^{N_s^{(\vec{s})}} w_k^{(\vec{s})} g_{i,j}^{(\vec{s})}(x_k^{(\vec{s})}) g_{i,j'}^{(\vec{s})}(x_k^{(\vec{s})}) \right] b_{i,j'}^{s_i}
\end{aligned}
$$

$$
\begin{aligned}
&+\sum_{s_{\bar{i}}=1}^{N_{\bar{i}}}\sum_{j'=1}^{m_{\bar{i}}}\left[\sum_{s_0=1}^{N_0}\sum_{k=1}^{N_s^{(\vec{s})}} w_k^{(\vec{s})} g_{i,j}^{(\vec{s})}\big(x_k^{(\vec{s})}\big) g_{\bar{i},j'}^{(\vec{s})}\big(x_k^{(\vec{s})}\big)\right] b_{\bar{i},j'}^{s_{\bar{i}}} \\
&=\sum_{s_{\bar{i}}=1}^{N_{\bar{i}}}\sum_{s_0=1}^{N_0}\sum_{k=1}^{N_s^{(\vec{s})}} w_k^{(\vec{s})} y_k^{(\vec{s})} g_{i,j}^{(\vec{s})}\big(x_k^{(\vec{s})}\big) \quad \text{for } (i,\bar{i})=(1,2),(2,1).
\end{aligned}
\tag{E.61}
$$

Using the matrix notation, these conditions are simply written as

$$
\hat{\xi}_{00}^{(\bullet,\bullet)}\vec{a}+\sum_{s_1}^{N_1}\hat{\xi}_{01}^{(s_1,\bullet)}\vec{b}_1^{s_1}+\sum_{s_2}^{N_2}\hat{\xi}_{02}^{(\bullet,s_2)}\vec{b}_2^{s_2}=\vec{\zeta}_0^{(\bullet,\bullet)}, \tag{E.62}
$$

$$
\hat{\xi}_{10}^{(s_1,\bullet)}\vec{a}+\hat{\xi}_{11}^{(s_1,\bullet)}\vec{b}_1^{s_1}+\sum_{s_2=1}^{N_2}\hat{\xi}_{12}^{(s_1,s_2)}\vec{b}_2^{s_2}=\vec{\zeta}_1^{(s_1,\bullet)} \quad \text{for } s_1=1,2,\cdots,N_1, \tag{E.63}
$$

$$
\hat{\xi}_{20}^{(\bullet,s_2)}\vec{a}+\sum_{s_1=1}^{N_1}\hat{\xi}_{21}^{(s_1,s_2)}\vec{b}_1^{s_1}+\hat{\xi}_{22}^{(\bullet,s_2)}\vec{b}_2^{s_2}=\vec{\zeta}_2^{(\bullet,s_2)} \quad \text{for } s_2=1,2,\cdots,N_2, \tag{E.64}
$$

where

$$
\left(\hat{\xi}_{ii'}^{(s_1,s_2)}\right)_{jj'}=\sum_{s_0=1}^{N_0}\sum_{k=1}^{N_s^{(\vec{s})}} w_k^{(\vec{s})} g_{i,j}^{(\vec{s})}\big(x_k^{(\vec{s})}\big) g_{i',j'}^{(\vec{s})}\big(x_k^{(\vec{s})}\big), \tag{E.65}
$$

$$
\left(\vec{\zeta}_i^{(s_1,s_2)}\right)_j=\sum_{s_0=1}^{N_0}\sum_{k=1}^{N_s^{(\vec{s})}} w_k^{(\vec{s})} y_k^{(\vec{s})} g_{i,j}^{(\vec{s})}\big(x_k^{(\vec{s})}\big), \tag{E.66}
$$

and the bullets • mean the sum of corresponding label s_1 or s_2.

The solution of the linear equation (E.62)–(E.64) is the fit result. In the following, we provide a way to solve this equation, which is applied to the analyses of the renormalization factors.

Inserting a slight modification of (E.63),

$$
\vec{b}_1^{s_1}=\left(\hat{\xi}_{11}^{(s_1,\bullet)}\right)^{-1}\left[\vec{\zeta}_1^{(s_1,\bullet)}-\hat{\xi}_{10}^{(s_1,\bullet)}\vec{a}-\sum_{s_2}^{N_2}\hat{\xi}_{12}^{(s_1,s_2)}\vec{b}_2^{s_2}\right], \tag{E.67}
$$

into (E.64), we obtain

$$
\begin{aligned}
&\sum_{s_2'=1}^{N_2}\left[\hat{\xi}_{22}^{(\bullet,s_2)}\delta^{s_2 s_2'}-\sum_{s_1=1}^{N_1}\hat{\xi}_{21}^{(s_1,s_2)}\left(\hat{\xi}_{11}^{(s_1,\bullet)}\right)^{-1}\hat{\xi}_{12}^{(s_1,s_2')}\right]\vec{b}_2^{s_2'} \\
&=\vec{\zeta}_2^{(\bullet,s_2)}-\sum_{s_1=1}^{N_1}\hat{\xi}_{21}^{(s_1,s_2)}\left(\hat{\xi}_{11}^{(s_1,\bullet)}\right)^{-1}\vec{\zeta}_1^{(s_1,\bullet)}-\left[\hat{\xi}_{20}^{(\bullet,s_2)}-\sum_{s_1=1}^{N_1}\hat{\xi}_{21}^{(s_1,s_2)}\left(\hat{\xi}_{11}^{(s_1,\bullet)}\right)^{-1}\hat{\xi}_{10}^{(s_1,\bullet)}\right]\vec{a}.
\end{aligned}
\tag{E.68}
$$

Next, we enhance the matrix notation involving s_2-space using the symbol '$\times$' such as $\vec{b}_2^{(\times)} = (\vec{b}_2^1, \vec{b}_2^2, \cdots, \vec{b}_2^{N_2})^T$. We denote (E.68) as

$$\begin{aligned}
&\left[\hat{\xi}_{22}^{(\bullet,\times)}\mathbb{1}^{(\times)} - \sum_{s_1=1}^{N_1} \hat{\xi}_{21}^{(s_1,\times)}\left(\hat{\xi}_{11}^{(s_1,\bullet)}\right)^{-1}\hat{\xi}_{12}^{(s_1,\times)}\right]\vec{b}_2^{(\times)} \\
&= \vec{\zeta}_2^{(\bullet,\times)} - \sum_{s_1=1}^{N_1} \hat{\xi}_{21}^{(s_1,\times)}\left(\hat{\xi}_{11}^{(s_1,\bullet)}\right)^{-1}\vec{\zeta}_1^{(s_1,\bullet)} - \left[\hat{\xi}_{20}^{(\bullet,\times)} - \sum_{s_1=1}^{N_1} \hat{\xi}_{21}^{(s_1,\times)}\left(\hat{\xi}_{11}^{(s_1,\bullet)}\right)^{-1}\hat{\xi}_{10}^{(s_1,\bullet)}\right]\vec{a}.
\end{aligned}$$

Consequently,

$$\begin{aligned}
\vec{b}_2^{(\times)} &= \left[\hat{\xi}_{22}^{(\bullet,\times)}\mathbb{1}^{(\times)} - \sum_{s_1=1}^{N_1} \hat{\xi}_{21}^{(s_1,\times)}\left(\hat{\xi}_{11}^{(s_1,\bullet)}\right)^{-1}\hat{\xi}_{12}^{(s_1,\times)}\right]^{-1} \\
&\quad\cdot\left\{\vec{\zeta}_2^{(\bullet,\times)} - \sum_{s_1=1}^{N_1} \hat{\xi}_{21}^{(s_1,\times)}\left(\hat{\xi}_{11}^{(s_1,\bullet)}\right)^{-1}\vec{\zeta}_1^{(s_1,\bullet)} - \left[\hat{\xi}_{20}^{(\bullet,\times)} - \sum_{s_1=1}^{N_1} \hat{\xi}_{21}^{(s_1,\times)}\left(\hat{\xi}_{11}^{(s_1,\bullet)}\right)^{-1}\hat{\xi}_{10}^{(s_1,\bullet)}\right]\vec{a}\right\}.
\end{aligned} \tag{E.69}$$

Inserting (E.67) and (E.69) into (E.62), we obtain the trivial equation of $\vec{a}$,

$$\begin{aligned}
&\left\{\hat{\xi}_{00}^{(\bullet,\bullet)} - \sum_{s_1=1}^{N_1} \hat{\xi}_{01}^{(s_1,\bullet)}\left(\hat{\xi}_{11}^{(s_1,\bullet)}\right)^{-1}\hat{\xi}_{10}^{(s_1,\bullet)}\right. \\
&\quad - \sum_{s_2,s_2'=1}^{N_2}\left[\hat{\xi}_{02}^{(\bullet,s_2)} - \sum_{s_1=1}^{N_1} \hat{\xi}_{01}^{(s_1,\bullet)}\left(\hat{\xi}_{11}^{(s_1,\bullet)}\right)^{-1}\hat{\xi}_{12}^{(s_1,s_2)}\right] \\
&\qquad\cdot\left[\hat{\xi}_{22}^{(\bullet,\times)}\mathbb{1}^{(\times)} - \sum_{s_1=1}^{N_1} \hat{\xi}_{21}^{(s_1,\times)}\left(\hat{\xi}_{11}^{(s_1,\bullet)}\right)^{-1}\hat{\xi}_{12}^{(s_1,\times)}\right]^{-1\,(s_2,s_2')} \\
&\qquad\left.\cdot\left[\hat{\xi}_{20}^{(\bullet,s_2')} - \sum_{s_1=1}^{N_1} \hat{\xi}_{21}^{(s_1,s_2')}\left(\hat{\xi}_{11}^{(s_1,\bullet)}\right)^{-1}\hat{\xi}_{10}^{(s_1,\bullet)}\right]\right\}\vec{a} \\
&= \vec{\zeta}_0^{(\bullet,\bullet)} - \sum_{s_1=1}^{N_1} \hat{\xi}_{01}^{(s_1,\bullet)}\left(\hat{\xi}_{11}^{(s_1,\bullet)}\right)^{-1}\vec{\zeta}_1^{(s_1,\bullet)} \\
&\quad - \sum_{s_2,s_2'=1}^{N_2}\left[\hat{\xi}_{02}^{(\bullet,s_2)} - \sum_{s_1=1}^{N_1} \hat{\xi}_{01}^{(s_1,\bullet)}\left(\hat{\xi}_{11}^{(s_1,\bullet)}\right)^{-1}\hat{\xi}_{12}^{(s_1,s_2)}\right] \\
&\qquad\cdot\left[\hat{\xi}_{22}^{(\bullet,\times)}\mathbb{1}^{(\times)} - \sum_{s_1=1}^{N_1} \hat{\xi}_{21}^{(s_1,\times)}\left(\hat{\xi}_{11}^{(s_1,\bullet)}\right)^{-1}\hat{\xi}_{12}^{(s_1,\times)}\right]^{-1\,(s_2,s_2')} \\
&\qquad\cdot\left[\vec{\zeta}_2^{(\bullet,s_2')} - \sum_{s_1=1}^{N_1} \hat{\xi}_{21}^{(s_1,s_2')}\left(\hat{\xi}_{11}^{(s_1,\bullet)}\right)^{-1}\vec{\zeta}_1^{(s_1,\bullet)}\right],
\end{aligned} \tag{E.70}$$

where the unknown parameters $\vec{b}_i^{s_i}$ are absent. Since the matrix $\{\cdots\}$ on the LHS is calculable, we can obtain the solution $\vec{a}$. Inserting this solution into (E.69), the solution $\vec{b}_2^{s_2}$ is obtained. Lastly, $\vec{b}_1^{s_1}$ is obtained using these solutions and (E.67). The statistical uncertainty is estimated by the bootstrap analysis [109].

Appendix F

Supplementary figures

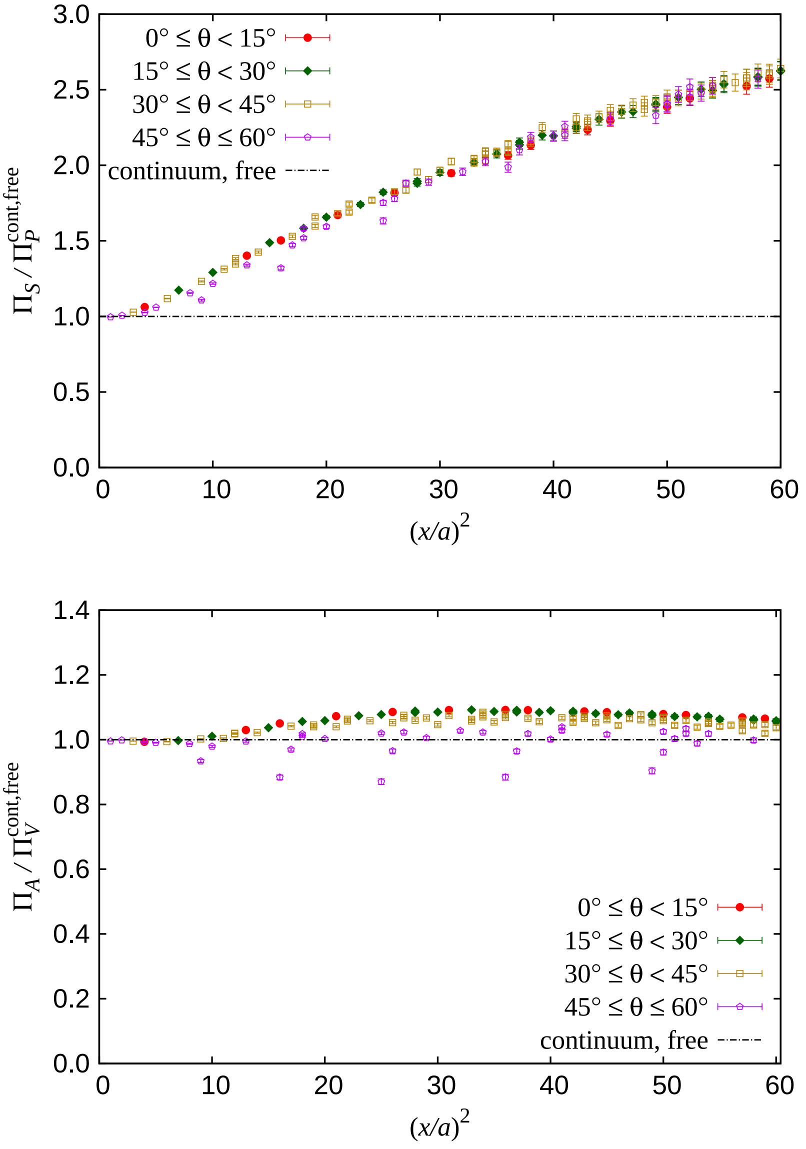

FIGURE F.1: Same as Fig. 3.3 but for the scalar (left) and axial-vector (right) channels.

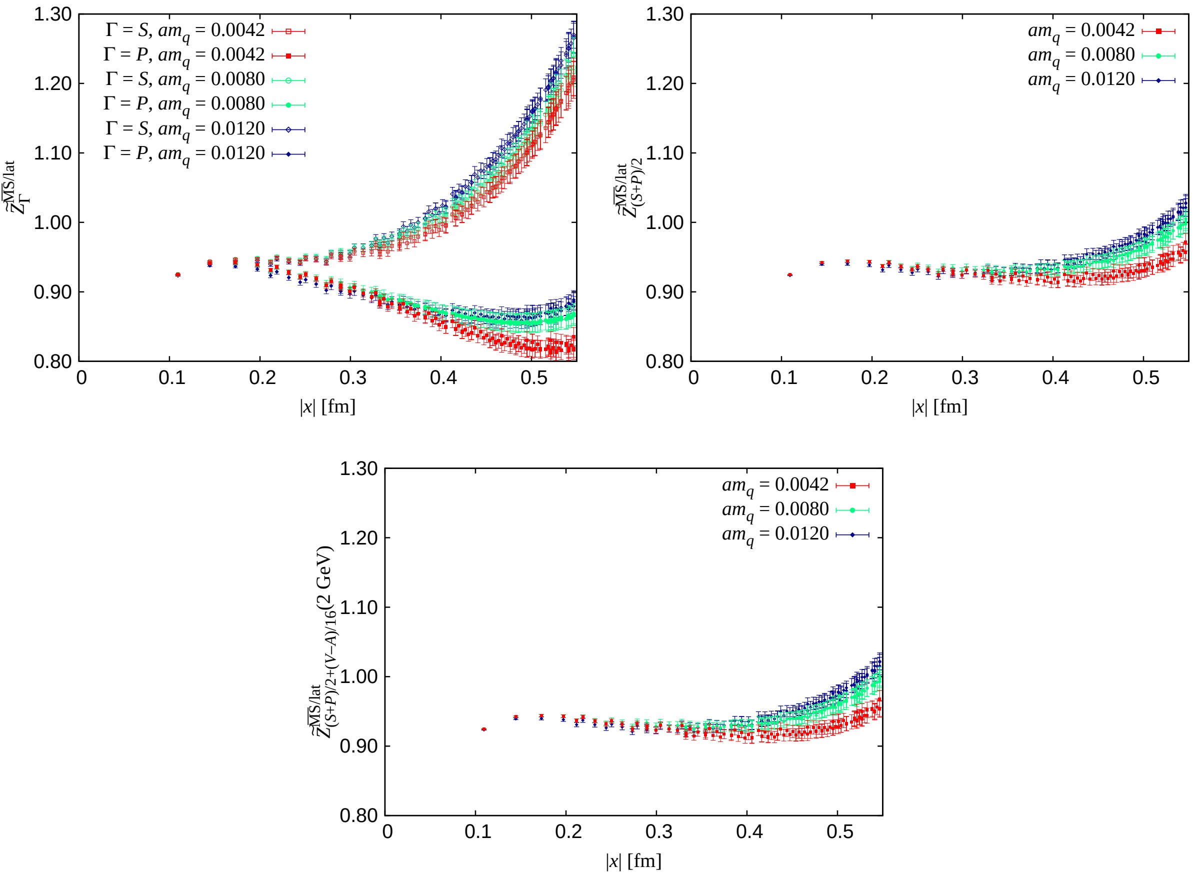

FIGURE F.2: Left: same as Fig. 4.1 but for the scalar (open points) and pseudoscalar (filled points) channels. Right: result of naïve average of the scalar and pseudoscalar correlators. Bottom: result of (4.9)

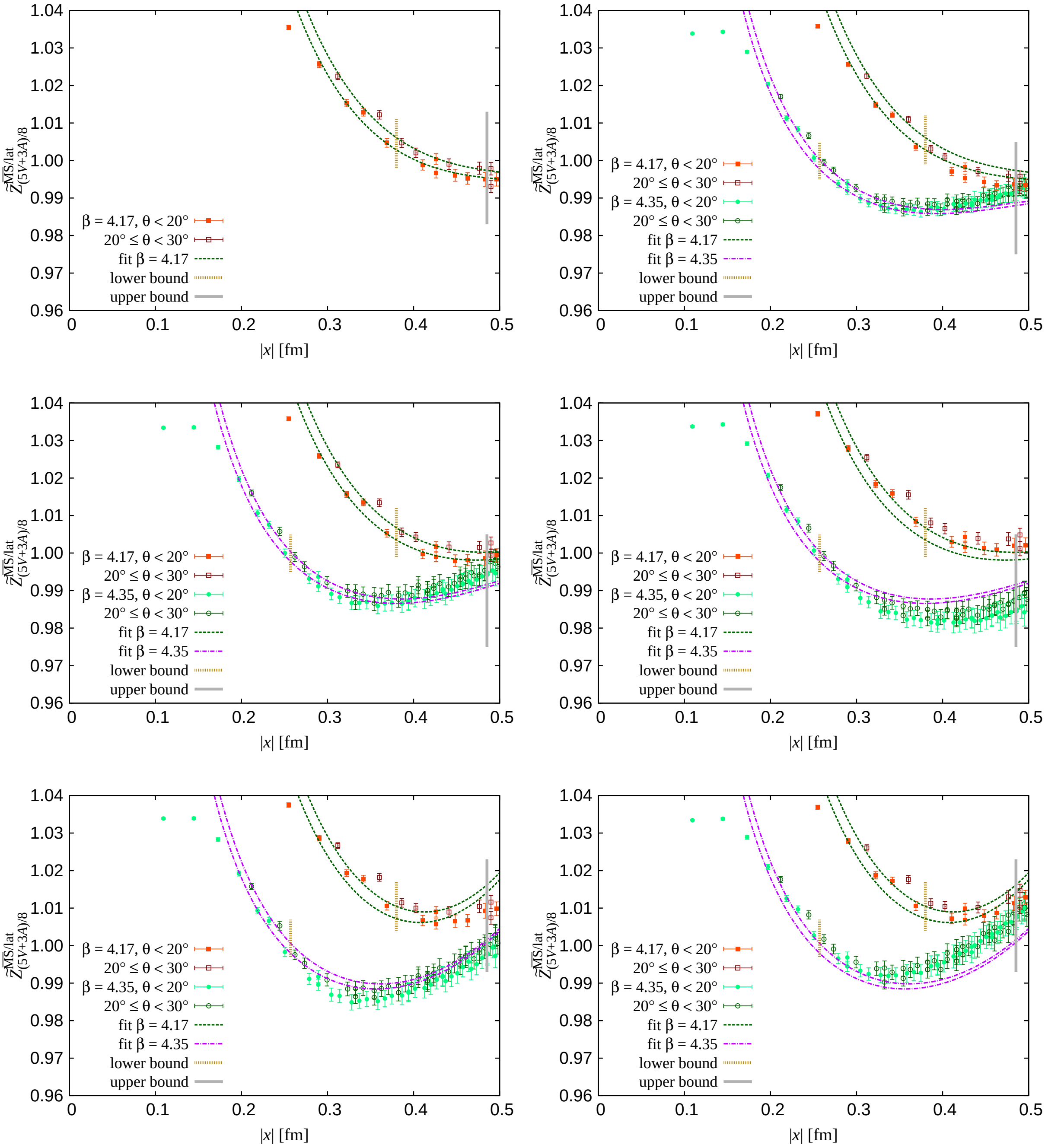

FIGURE F.3: Same as Fig. 4.3 but the results at $(\beta, am_q, am_s) = (4.17, 0.0035, 0.0400)$ (top/left),
$(4.17, 0.0070, 0.0400)$ and $(4.35, 0.0042, 0.0250)$ (top/right),
$(4.17, 0.0120, 0.0300)$ and $(4.35, 0.0080, 0.0180)$ (middle/left),
$(4.17, 0.0120, 0.0400)$ and $(4.35, 0.0080, 0.0250)$ (middle/right),
$(4.17, 0.0190, 0.0300)$ and $(4.35, 0.0120, 0.0180)$ (bottom/left),
$(4.17, 0.0190, 0.0400)$ and $(4.35, 0.0120, 0.0250)$ (bottom/right).

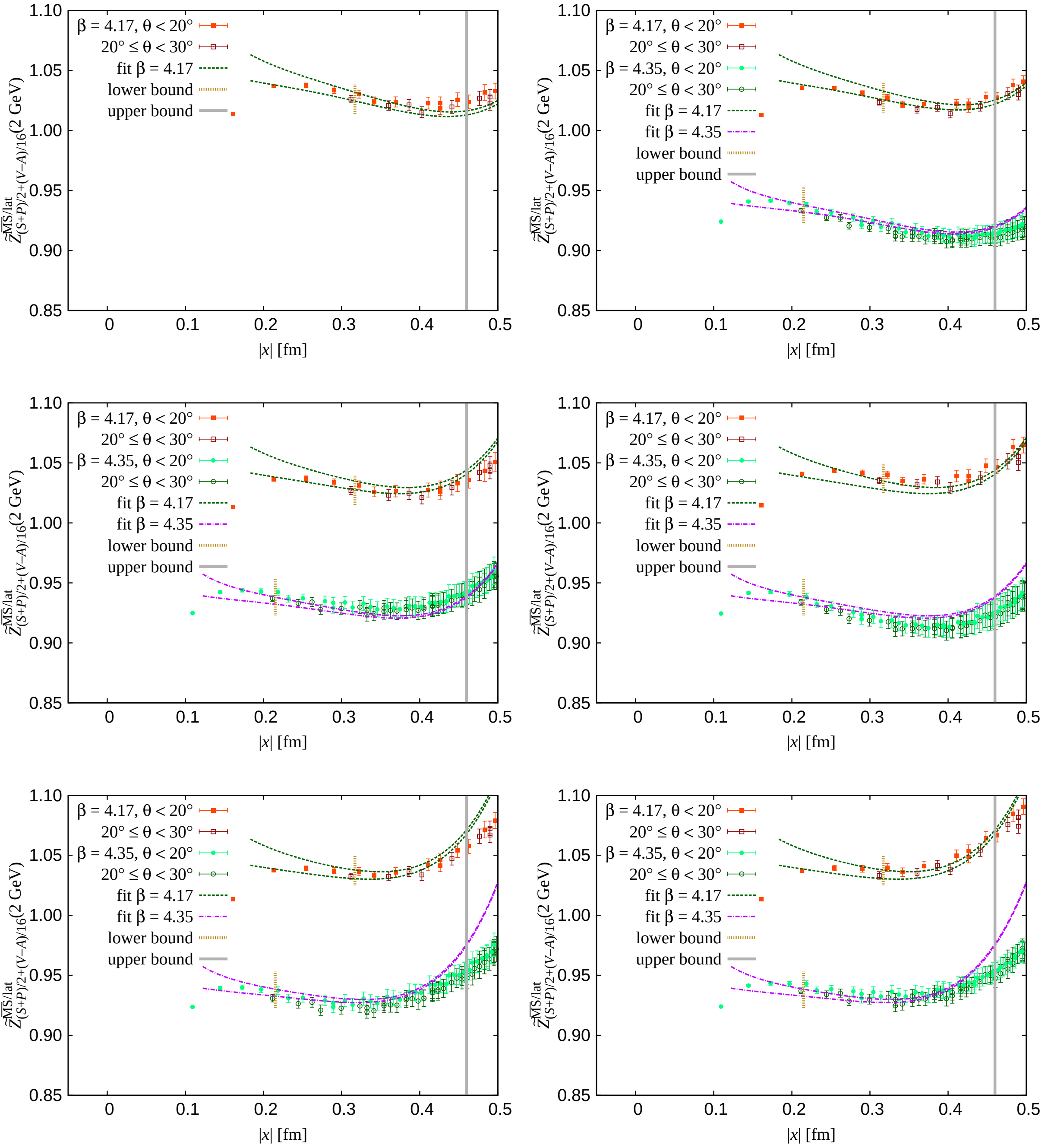

FIGURE F.4: Same as Fig. 4.4 but the results at the ensembles whose (β, am_q, am_s) are
top/left: $(4.17, 0.0035, 0.0400)$,
top/right: $(4.17, 0.0070, 0.0400)$ and $(4.35, 0.0042, 0.0250)$,
middle/left: $(4.17, 0.0120, 0.0300)$ and $(4.35, 0.0080, 0.0180)$,
middle/right: $(4.17, 0.0120, 0.0400)$ and $(4.35, 0.0080, 0.0250)$,
bottom/left: $(4.17, 0.0190, 0.0300)$ and $(4.35, 0.0120, 0.0180)$,
bottom/right: $(4.17, 0.0190, 0.0400)$ and $(4.35, 0.0120, 0.0250)$.

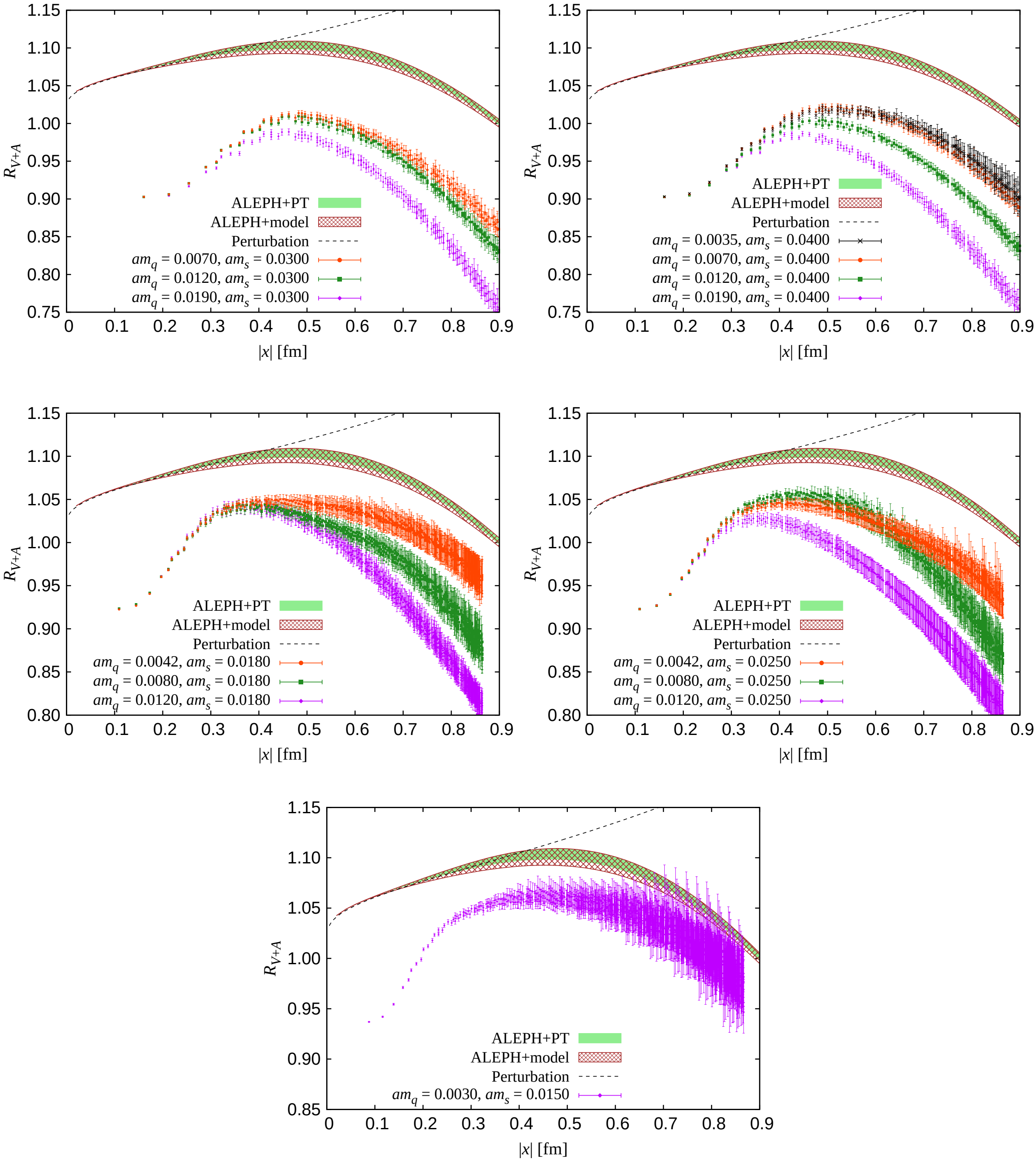

FIGURE F.5: Same as Fig. 5.1 but the results at the ensembles whose (β, am_q, am_s) are
top/left: $(4.17, 0.0070, 0.0300)$, $(4.17, 0.0120, 0.0300)$, $(4.17, 0.0190, 0.0300)$,
top/right: $(4.17, 0.0035, 0.0400)$, $(4.17, 0.0070, 0.0400)$, $(4.17, 0.0120, 0.0400)$, $(4.17, 0.0190, 0.0400)$,
middle/left: $(4.35, 0.0042, 0.0180)$, $(4.35, 0.0080, 0.0180)$, $(4.35, 0.0120, 0.0180)$,
middle/right: $(4.35, 0.0042, 0.0250)$, $(4.35, 0.0080, 0.0250)$, $(4.35, 0.0120, 0.0250)$,
bottom/left: $(4.47, 0.0030, 0.0150)$.

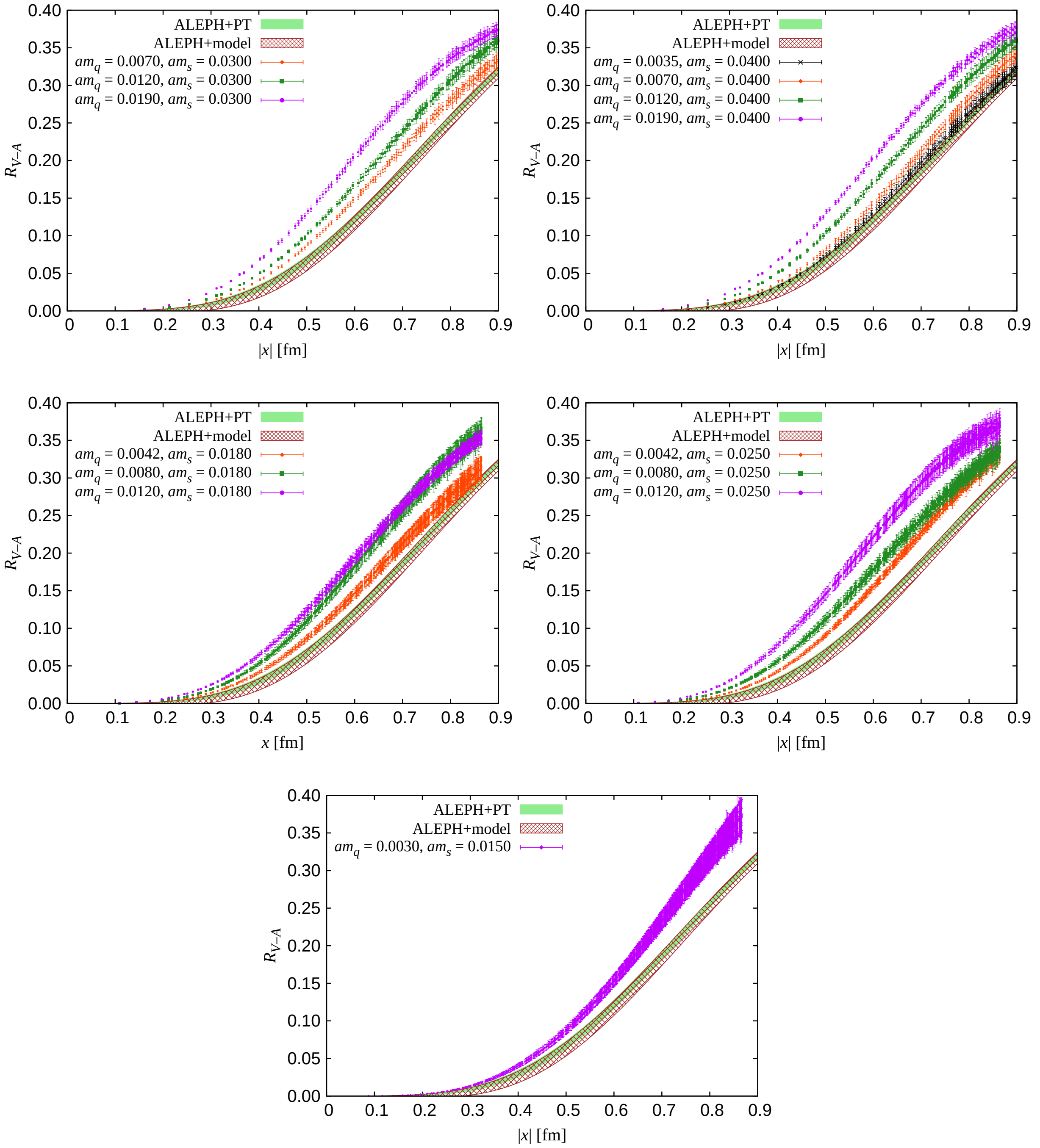

FIGURE F.6: Same as Fig. 5.5 but the results at the ensembles whose (β, am_q, am_s) are
top/left: $(4.17, 0.0070, 0.0300)$, $(4.17, 0.0120, 0.0300)$, $(4.17, 0.0190, 0.0300)$,
top/right: $(4.17, 0.0035, 0.0400)$, $(4.17, 0.0070, 0.0400)$, $(4.17, 0.0120, 0.0400)$, $(4.17, 0.0190, 0.0400)$,
middle/left: $(4.35, 0.0042, 0.0180)$, $(4.35, 0.0080, 0.0180)$, $(4.35, 0.0120, 0.0180)$,
middle/right: $(4.35, 0.0042, 0.0250)$, $(4.35, 0.0080, 0.0250)$, $(4.35, 0.0120, 0.0250)$,
bottom/left: $(4.47, 0.0030, 0.0150)$.

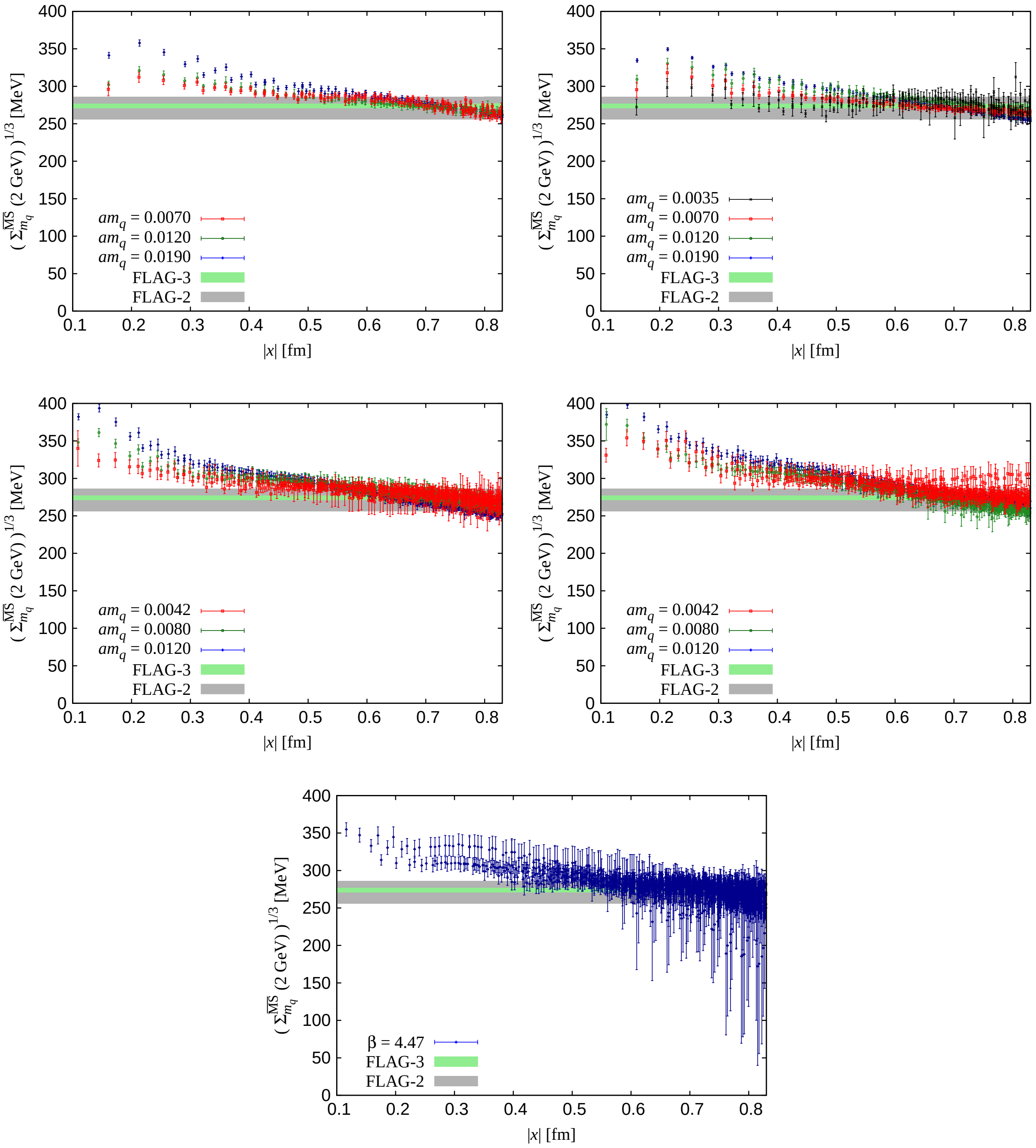

FIGURE F.7: Same as Fig. 5.7 but the results at the ensembles whose (β, am_q, am_s) are
top/left: $(4.17, 0.0070, 0.0300)$, $(4.17, 0.0120, 0.0300)$, $(4.17, 0.0190, 0.0300)$,
top/right: $(4.17, 0.0035, 0.0400)$, $(4.17, 0.0070, 0.0400)$, $(4.17, 0.0120, 0.0400)$, $(4.17, 0.0190, 0.0400)$,
middle/left: $(4.35, 0.0042, 0.0180)$, $(4.35, 0.0080, 0.0180)$, $(4.35, 0.0120, 0.0180)$,
middle/right: $(4.35, 0.0042, 0.0250)$, $(4.35, 0.0080, 0.0250)$, $(4.35, 0.0120, 0.0250)$,
bottom/left: $(4.47, 0.0030, 0.0150)$.

Bibliography

[1] E. V. Shuryak, “Correlation functions in the QCD vacuum,” *Rev. Mod. Phys.* **65** (1993) 1–46.

[2] K. G. Wilson, “Nonlagrangian models of current algebra,” *Phys. Rev.* **179** (1969) 1499–1512.

[3] K. G. Wilson, “The Renormalization Group and Strong Interactions,” *Phys. Rev.* **D3** (1971) 1818.

[4] M. A. Shifman, A. I. Vainshtein, and V. I. Zakharov, “QCD and Resonance Physics. Theoretical Foundations,” *Nucl. Phys.* **B147** (1979) 385–447.

[5] M. A. Shifman, A. I. Vainshtein, and V. I. Zakharov, “QCD and Resonance Physics: Applications,” *Nucl. Phys.* **B147** (1979) 448–518.

[6] M. A. Shifman, A. I. Vainshtein, and V. I. Zakharov, “QCD and Resonance Physics. The rho-omega Mixing,” *Nucl. Phys.* **B147** (1979) 519–534.

[7] V. A. Novikov, M. A. Shifman, A. I. Vainshtein, and V. I. Zakharov, “Are All Hadrons Alike?,” *Nucl. Phys.* **B191** (1981) 301.

[8] T. A. DeGrand, “Short distance current correlators: Comparing lattice simulations to the instanton liquid,” *Phys. Rev.* **D64** (2001) 094508, `arXiv:hep-lat/0106001 [hep-lat]`.

[9] P. Faccioli and T. A. DeGrand, “Evidence for instanton induced dynamics, from lattice QCD,” *Phys. Rev. Lett.* **91** (2003) 182001, `arXiv:hep-ph/0304219 [hep-ph]`.

[10] G. ’t Hooft, “Computation of the Quantum Effects Due to a Four-Dimensional Pseudoparticle,” *Phys. Rev.* **D14** (1976) 3432–3450. [Erratum: Phys. Rev.D18,2199(1978)].

[11] E. V. Shuryak, “The Role of Instantons in Quantum Chromodynamics. 1. Physical Vacuum,” *Nucl. Phys.* **B203** (1982) 93.

[12] K. G. Chetyrkin, S. Narison, and V. I. Zakharov, “Short distance tachyonic gluon mass and 1 / Q**2 corrections,” *Nucl. Phys.* **B550** (1999) 353–374, `arXiv:hep-ph/9811275 [hep-ph]`.

[13] **ALEPH** Collaboration, R. Barate *et al.*, "Measurement of the spectral functions of axial - vector hadronic tau decays and determination of alpha(S)(M**2(tau))," *Eur. Phys. J.* **C4** (1998) 409–431.

[14] T. Schaefer and E. V. Shuryak, "Implications of the ALEPH tau lepton decay data for perturbative and nonperturbative QCD," *Phys. Rev. Lett.* **86** (2001) 3973–3976, `arXiv:hep-ph/0010116 [hep-ph]`.

[15] A. Pich, "QCD predictions for the tau hadronic width: Determination of alpha-s (M(tau)**2)," *Nucl. Phys. Proc. Suppl.* **39BC** (1995) 326, `arXiv:hep-ph/9412273 [hep-ph]`.

[16] M. B. Voloshin, "Precision determination of alpha-s and m(b) from QCD sum rules for b anti-b," *Int. J. Mod. Phys.* **A10** (1995) 2865–2880, `arXiv:hep-ph/9502224 [hep-ph]`.

[17] **ALEPH** Collaboration, D. Buskulic *et al.*, "Measurement of the strong coupling constant using tau decays," *Phys. Lett.* **B307** (1993) 209–220.

[18] **OPAL** Collaboration, K. Ackerstaff *et al.*, "Measurement of the strong coupling constant alpha(s) and the vector and axial vector spectral functions in hadronic tau decays," *Eur. Phys. J.* **C7** (1999) 571–593, `arXiv:hep-ex/9808019 [hep-ex]`.

[19] M. Neubert, "QCD analysis of hadronic tau decays revisited," *Nucl. Phys.* **B463** (1996) 511–546, `arXiv:hep-ph/9509432 [hep-ph]`.

[20] B. V. Geshkenbein, B. L. Ioffe, and K. N. Zyablyuk, "The Check of QCD based on the tau - decay data analysis in the complex q**2 - plane," *Phys. Rev.* **D64** (2001) 093009, `arXiv:hep-ph/0104048 [hep-ph]`.

[21] M. A. Shifman, "Theory of preasymptotic effects in weak inclusive decays," in *Workshop on Continuous Advances in QCD Minneapolis, Minnesota, February 18-20, 1994*. 1994. `arXiv:hep-ph/9405246 [hep-ph]`.

[22] B. Blok, M. A. Shifman, and D.-X. Zhang, "An Illustrative example of how quark hadron duality might work," *Phys. Rev.* **D57** (1998) 2691–2700, `arXiv:hep-ph/9709333 [hep-ph]`. [Erratum: Phys. Rev.D59,019901(1999)].

[23] M. A. Shifman, "Quark hadron duality," in *Proceedings, 8th International Symposium on Heavy Flavor Physics (Heavy Flavors 8)*, p. hf8/013. 2000. `arXiv:hep-ph/0009131 [hep-ph]`. [,hf8/013(2000)].

[24] I. I. Y. Bigi and N. Uraltsev, "A Vademecum on quark hadron duality," *Int. J. Mod. Phys.* **A16** (2001) 5201–5248, `arXiv:hep-ph/0106346 [hep-ph]`.

[25] O. Cata, M. Golterman, and S. Peris, "Possible duality violations in tau decay and their impact on the determination of alpha(s)," *Phys. Rev.* **D79** (2009) 053002, `arXiv:0812.2285 [hep-ph]`.

[26] O. Cata, M. Golterman, and S. Peris, "Unraveling duality violations in hadronic tau decays," *Phys. Rev.* **D77** (2008) 093006, `arXiv:0803.0246 [hep-ph]`.

[27] O. Cata, M. Golterman, and S. Peris, "Duality violations and spectral sum rules," *JHEP* **08** (2005) 076, `arXiv:hep-ph/0506004 [hep-ph]`.

[28] D. Boito, O. Cata, M. Golterman, M. Jamin, K. Maltman, J. Osborne, and S. Peris, "A new determination of α_s from hadronic τ decays," *Phys. Rev.* **D84** (2011) 113006, `arXiv:1110.1127 [hep-ph]`.

[29] D. Boito, M. Golterman, M. Jamin, A. Mahdavi, K. Maltman, J. Osborne, and S. Peris, "An Updated determination of α_s from τ decays," *Phys. Rev.* **D85** (2012) 093015, `arXiv:1203.3146 [hep-ph]`.

[30] D. Boito, M. Golterman, K. Maltman, J. Osborne, and S. Peris, "Strong coupling from the revised ALEPH data for hadronic τ decays," *Phys. Rev.* **D91** no. 3, (2015) 034003, `arXiv:1410.3528 [hep-ph]`.

[31] M. C. Chu, J. M. Grandy, S. Huang, and J. W. Negele, "Correlation functions of hadron currents in the QCD vacuum calculated in lattice QCD," *Phys. Rev.* **D48** (1993) 3340–3353, `arXiv:hep-lat/9306002 [hep-lat]`.

[32] **UKQCD** Collaboration, S. J. Hands, P. W. Stephenson, and A. McKerrell, "Point-to-point hadron correlation functions using the Sheikholeslami-Wohlert action," *Phys. Rev.* **D51** (1995) 6394–6402, `arXiv:hep-lat/9412065 [hep-lat]`.

[33] **TWQCD, JLQCD** Collaboration, E. Shintani, S. Aoki, T. W. Chiu, S. Hashimoto, T. H. Hsieh, T. Kaneko, H. Matsufuru, J. Noaki, T. Onogi, and N. Yamada, "Lattice study of the vacuum polarization function and determination of the strong coupling constant," *Phys. Rev.* **D79** (2009) 074510, `arXiv:0807.0556 [hep-lat]`.

[34] E. Shintani, S. Aoki, H. Fukaya, S. Hashimoto, T. Kaneko, T. Onogi, and N. Yamada, "Strong coupling constant from vacuum polarization functions in three-flavor lattice QCD with dynamical overlap fermions," *Phys. Rev.* **D82** no. 7, (2010) 074505, `arXiv:1002.0371 [hep-lat]`. [Erratum: Phys. Rev.D89,no.9,099903(2014)].

[35] G. Martinelli, G. C. Rossi, C. T. Sachrajda, S. R. Sharpe, M. Talevi, and M. Testa, "Nonperturbative improvement of composite operators with Wilson fermions," *Phys. Lett.* **B411** (1997) 141–151, `arXiv:hep-lat/9705018 [hep-lat]`.

[36] V. Gimenez, L. Giusti, S. Guerriero, V. Lubicz, G. Martinelli, S. Petrarca, J. Reyes, B. Taglienti, and E. Trevigne, "Non-perturbative renormalization of lattice operators in coordinate space," *Phys. Lett.* **B598** (2004) 227–236, `arXiv:hep-lat/0406019 [hep-lat]`.

[37] K. Cichy, K. Jansen, and P. Korcyl, "Non-perturbative renormalization in coordinate space for $N_f = 2$ maximally twisted mass fermions with tree-level Symanzik improved gauge action," *Nucl. Phys.* **B865** (2012) 268–290, `arXiv:1207.0628 [hep-lat]`.

[38] K. G. Chetyrkin and A. Maier, "Massless correlators of vector, scalar and tensor currents in position space at orders α_s^3 and α_s^4: Explicit analytical results," *Nucl. Phys.* **B844** (2011) 266–288, `arXiv:1010.1145 [hep-ph]`.

[39] M. Davier, A. Hocker, B. Malaescu, C.-Z. Yuan, and Z. Zhang, "Update of the ALEPH non-strange spectral functions from hadronic τ decays," *Eur. Phys. J.* **C74** no. 3, (2014) 2803, `arXiv:1312.1501 [hep-ex]`.

[40] R. C. Brower, H. Neff, and K. Orginos, "Mobius fermions: Improved domain wall chiral fermions," *Nucl. Phys. Proc. Suppl.* **140** (2005) 686–688, `arXiv:hep-lat/0409118 [hep-lat]`. [,686(2004)].

[41] R. C. Brower, H. Neff, and K. Orginos, "The Móbius Domain Wall Fermion Algorithm," `arXiv:1206.5214 [hep-lat]`.

[42] **JLQCD** Collaboration, J. Noaki, S. Aoki, G. Cossu, H. Fukaya, S. Hashimoto, and T. Kaneko, "Fine lattice simulations with the Ginsparg-Wilson fermions," *PoS* **LATTICE2014** (2014) 069.

[43] D. B. Kaplan, "A Method for simulating chiral fermions on the lattice," *Phys. Lett.* **B288** (1992) 342–347, `arXiv:hep-lat/9206013 [hep-lat]`.

[44] Y. Shamir, "Chiral fermions from lattice boundaries," *Nucl. Phys.* **B406** (1993) 90–106, `arXiv:hep-lat/9303005 [hep-lat]`.

[45] P. H. Ginsparg and K. G. Wilson, "A Remnant of Chiral Symmetry on the Lattice," *Phys. Rev.* **D25** (1982) 2649.

[46] T. van Ritbergen, J. A. M. Vermaseren, and S. A. Larin, "The Four loop beta function in quantum chromodynamics," *Phys. Lett.* **B400** (1997) 379–384, `hep-ph/9701390`.

[47] S. J. Brodsky, G. P. Lepage, and P. B. Mackenzie, "On the Elimination of Scale Ambiguities in Perturbative Quantum Chromodynamics," *Phys. Rev.* **D28** (1983) 228.

[48] S. J. Brodsky and X.-G. Wu, "Scale Setting Using the Extended Renormalization Group and the Principle of Maximum Conformality: the QCD Coupling Constant at Four

Loops," *Phys. Rev.* **D85** (2012) 034038, `arXiv:1111.6175 [hep-ph]`. [Erratum: Phys. Rev.D86,079903(2012)].

[49] M. Mojaza, S. J. Brodsky, and X.-G. Wu, "Systematic All-Orders Method to Eliminate Renormalization-Scale and Scheme Ambiguities in Perturbative QCD," *Phys. Rev. Lett.* **110** (2013) 192001, `arXiv:1212.0049 [hep-ph]`.

[50] X.-G. Wu, S. J. Brodsky, and M. Mojaza, "The Renormalization Scale-Setting Problem in QCD," *Prog. Part. Nucl. Phys.* **72** (2013) 44–98, `arXiv:1302.0599 [hep-ph]`.

[51] K. G. Chetyrkin, "Quark mass anomalous dimension to O (alpha-s**4)," *Phys. Lett.* **B404** (1997) 161–165, `arXiv:hep-ph/9703278 [hep-ph]`.

[52] J. A. M. Vermaseren, S. A. Larin, and T. van Ritbergen, "The four loop quark mass anomalous dimension and the invariant quark mass," *Phys. Lett.* **B405** (1997) 327–333, `arXiv:hep-ph/9703284 [hep-ph]`.

[53] S. Kluth, "Tests of Quantum Chromo Dynamics at e+ e- Colliders," *Rept. Prog. Phys.* **69** (2006) 1771–1846, `arXiv:hep-ex/0603011 [hep-ex]`.

[54] M. Davier, A. Hocker, and Z. Zhang, "The Physics of hadronic tau decays," *Rev. Mod. Phys.* **78** (2006) 1043–1109, `arXiv:hep-ph/0507078 [hep-ph]`.

[55] A. Pich, "Precision Tau Physics," *Prog. Part. Nucl. Phys.* **75** (2014) 41–85, `arXiv:1310.7922 [hep-ph]`.

[56] **CKMfitter Group** Collaboration, J. Charles, A. Hocker, H. Lacker, S. Laplace, F. R. Le Diberder, J. Malcles, J. Ocariz, M. Pivk, and L. Roos, "CP violation and the CKM matrix: Assessing the impact of the asymmetric B factories," *Eur. Phys. J.* **C41** (2005) 1–131, `arXiv:hep-ph/0406184 [hep-ph]`.

[57] W. J. Marciano and A. Sirlin, "Electroweak Radiative Corrections to tau Decay," *Phys. Rev. Lett.* **61** (1988) 1815–1818.

[58] R. Alemany, M. Davier, and A. Hocker, "Improved determination of the hadronic contribution to the muon (g-2) and to alpha (M(z)) using new data from hadronic tau decays," *Eur. Phys. J.* **C2** (1998) 123–135, `arXiv:hep-ph/9703220 [hep-ph]`.

[59] M. Davier, S. Eidelman, A. Hocker, and Z. Zhang, "Confronting spectral functions from e+ e- annihilation and tau decays: Consequences for the muon magnetic moment," *Eur. Phys. J.* **C27** (2003) 497–521, `arXiv:hep-ph/0208177 [hep-ph]`.

[60] **Particle Data Group** Collaboration, K. A. Olive *et al.*, "Review of Particle Physics," *Chin. Phys.* **C38** (2014) 090001.

[61] **ALEPH** Collaboration, R. Barate *et al.*, "Measurement of the spectral functions of vector current hadronic tau decays," *Z. Phys.* **C76** (1997) 15–33.

[62] **ALEPH** Collaboration, S. Schael *et al.*, "Branching ratios and spectral functions of tau decays: Final ALEPH measurements and physics implications," *Phys. Rept.* **421** (2005) 191–284, `arXiv:hep-ex/0506072 [hep-ex]`.

[63] M. Davier, S. Descotes-Genon, A. Hocker, B. Malaescu, and Z. Zhang, "The Determination of alpha(s) from Tau Decays Revisited," *Eur. Phys. J.* **C56** (2008) 305–322, `arXiv:0803.0979 [hep-ph]`.

[64] Z. Zhang, M. Davier, A. Hoecker, B. Malaescu, and C. Yuan, "Invariant mass squared distributions from ALEPH," 2014. `http://aleph.web.lal.in2p3.fr/tau/specfun13.html`.

[65] P. A. Baikov, K. G. Chetyrkin, and J. H. Kuhn, "Order alpha**4(s) QCD Corrections to Z and tau Decays," *Phys. Rev. Lett.* **101** (2008) 012002, `arXiv:0801.1821 [hep-ph]`.

[66] P. A. Baikov, K. G. Chetyrkin, and J. H. Kuhn, "R(s) and hadronic tau-Decays in Order alpha**4(s): Technical aspects," *Nucl. Phys. Proc. Suppl.* **189** (2009) 49–53, `arXiv:0906.2987 [hep-ph]`.

[67] D. J. Broadhurst and S. C. Generalis, "DIMENSION EIGHT CONTRIBUTIONS TO LIGHT QUARK QCD SUM RULES," *Phys. Lett.* **B165** (1985) 175–180.

[68] M. Jamin and M. Munz, "Current correlators to all orders in the quark masses," *Z. Phys.* **C60** (1993) 569–578, `arXiv:hep-ph/9208201 [hep-ph]`.

[69] S. Narison and V. I. Zakharov, "Hints on the power corrections from current correlators in x space," *Phys. Lett.* **B522** (2001) 266–272, `arXiv:hep-ph/0110141 [hep-ph]`.

[70] C. Becchi, S. Narison, E. de Rafael, and F. J. Yndurain, "Light Quark Masses in Quantum Chromodynamics and Chiral Symmetry Breaking," *Z. Phys.* **C8** (1981) 335.

[71] V. Shevchenko and Yu. Simonov, "Operator product expansion and confinement," *Phys. Rev.* **D65** (2002) 074029, `arXiv:hep-ph/0109051 [hep-ph]`.

[72] H.-H. Zhang, K.-X. Feng, S.-W. Qiu, A. Zhao, and X.-S. Li, "On analytic formulas of Feynman propagators in position space," *Chin. Phys.* **C34** (2010) 1576–1582, `arXiv:0811.1261 [math-ph]`.

[73] L. S. Brown, R. D. Carlitz, D. B. Creamer, and C.-k. Lee, "Propagation Functions in Pseudoparticle Fields," *Phys. Rev.* **D17** (1978) 1583.

[74] G. 't Hooft, "A Two-Dimensional Model for Mesons," *Nucl. Phys.* **B75** (1974) 461–470.

[75] P. D. B. Collins, *An Introduction to Regge Theory and High-Energy Physics*. Cambridge Monographs on Mathematical Physics. Cambridge Univ. Press, Cambridge, UK, 2009.

[76] C. Morningstar and M. J. Peardon, "Analytic smearing of SU(3) link variables in lattice QCD," *Phys. Rev.* **D69** (2004) 054501, `arXiv:hep-lat/0311018 [hep-lat]`.

[77] K. Symanzik, "Continuum Limit and Improved Action in Lattice Theories. 1. Principles and phi**4 Theory," *Nucl. Phys.* **B226** (1983) 187–204.

[78] M. Luscher and P. Weisz, "On-Shell Improved Lattice Gauge Theories," *Commun. Math. Phys.* **97** (1985) 59. [Erratum: Commun. Math. Phys.98,433(1985)].

[79] M. Luscher, "Properties and uses of the Wilson flow in lattice QCD," *JHEP* **08** (2010) 071, `arXiv:1006.4518 [hep-lat]`. [Erratum: JHEP03,092(2014)].

[80] J. Gasser and H. Leutwyler, "Light Quarks at Low Temperatures," *Phys. Lett.* **B184** (1987) 83.

[81] G. Cossu, J. Noaki, S. Hashimoto, T. Kaneko, H. Fukaya, P. A. Boyle, and J. Doi, "JLQCD IroIro++ lattice code on BG/Q," in *Proceedings, 31st International Symposium on Lattice Field Theory (Lattice 2013)*. 2013. `arXiv:1311.0084 [hep-lat]`.

[82] G. P. Lepage and P. B. Mackenzie, "On the viability of lattice perturbation theory," *Phys. Rev.* **D48** (1993) 2250–2264, `arXiv:hep-lat/9209022 [hep-lat]`.

[83] R. Sommer, "Nonperturbative renormalization of QCD," *Lect. Notes Phys.* **512** (1998) 65–113, `arXiv:hep-ph/9711243 [hep-ph]`.

[84] S. Capitani, "Lattice perturbation theory," *Phys. Rept.* **382** (2003) 113–302, `arXiv:hep-lat/0211036 [hep-lat]`.

[85] M. Bochicchio, L. Maiani, G. Martinelli, G. C. Rossi, and M. Testa, "Chiral Symmetry on the Lattice with Wilson Fermions," *Nucl. Phys.* **B262** (1985) 331.

[86] A. Vladikas, "Three Topics in Renormalization and Improvement," in *Modern perspectives in lattice QCD: Quantum field theory and high performance computing. Proceedings, International School, 93rd Session, Les Houches, France, August 3-28, 2009*, pp. 161–222. 2011. `arXiv:1103.1323 [hep-lat]`.

[87] M. Luscher, R. Narayanan, P. Weisz, and U. Wolff, "The Schrodinger functional: A Renormalizable probe for nonAbelian gauge theories," *Nucl. Phys.* **B384** (1992) 168–228, `arXiv:hep-lat/9207009 [hep-lat]`.

[88] S. Sint, "On the Schrodinger functional in QCD," *Nucl. Phys.* **B421** (1994) 135–158, `arXiv:hep-lat/9312079 [hep-lat]`.

[89] K. Jansen, C. Liu, M. Luscher, H. Simma, S. Sint, R. Sommer, P. Weisz, and U. Wolff, "Nonperturbative renormalization of lattice QCD at all scales," *Phys. Lett.* **B372** (1996) 275–282, `arXiv:hep-lat/9512009 [hep-lat]`.

[90] M. Luscher, P. Weisz, and U. Wolff, "A Numerical method to compute the running coupling in asymptotically free theories," *Nucl. Phys.* **B359** (1991) 221–243.

[91] Y. Murakami and K.-I. Ishikawa, "A construction of the Schrödinger Functional for Möbius Domain Wall Fermions," *PoS* **LATTICE2014** (2014) 331, `arXiv:1410.8335 [hep-lat]`.

[92] S. Takeda, "Formulation of domain-wall fermions in the Schrödinger functional," *Phys. Rev.* **D87** no. 11, (2013) 114506, `arXiv:1010.3504 [hep-lat]`.

[93] R. Sommer, "Non-perturbative QCD: Renormalization, O(a)-improvement and matching to Heavy Quark Effective Theory," in *Workshop on Perspectives in Lattice QCD Nara, Japan, October 31-November 11, 2005*. 2006. `arXiv:hep-lat/0611020 [hep-lat]`.

[94] G. Martinelli, C. Pittori, C. T. Sachrajda, M. Testa, and A. Vladikas, "A General method for nonperturbative renormalization of lattice operators," *Nucl. Phys.* **B445** (1995) 81–108, `arXiv:hep-lat/9411010 [hep-lat]`.

[95] **JLQCD** Collaboration, M. Tomii, G. Cossu, B. Fahy, H. Fukaya, S. Hashimoto, T. Kaneko, and J. Noaki, "Renormalization of domain-wall bilinear operators with short-distance current correlators," `arXiv:1604.08702 [hep-lat]`.

[96] S. Aoki *et al.*, "Review of lattice results concerning low-energy particle physics," `arXiv:1607.00299 [hep-lat]`.

[97] S. Aoki *et al.*, "Review of lattice results concerning low-energy particle physics," *Eur. Phys. J.* **C74** (2014) 2890, `arXiv:1310.8555 [hep-lat]`.

[98] G. Cossu, H. Fukaya, S. Hashimoto, T. Kaneko, and J.-I. Noaki, "Stochastic calculation of the Dirac spectrum on the lattice and a determination of chiral condensate in 2+1-flavor QCD," `arXiv:1607.01099 [hep-lat]`.

[99] P. A. Baikov, K. G. Chetyrkin, and J. H. Kuhn, "Quark Mass and Field Anomalous Dimensions to $\mathcal{O}(\alpha_s^5)$," *JHEP* **10** (2014) 76, `arXiv:1402.6611 [hep-ph]`.

[100] H. B. Nielsen and M. Ninomiya, "No Go Theorem for Regularizing Chiral Fermions," *Phys. Lett.* **B105** (1981) 219–223.

[101] H. B. Nielsen and M. Ninomiya, "Absence of Neutrinos on a Lattice. 1. Proof by Homotopy Theory," *Nucl. Phys.* **B185** (1981) 20. [,533(1980)].

[102] H. B. Nielsen and M. Ninomiya, "Absence of Neutrinos on a Lattice. 2. Intuitive Topological Proof," *Nucl. Phys.* **B193** (1981) 173–194.

[103] M. Luscher, "Exact chiral symmetry on the lattice and the Ginsparg-Wilson relation," *Phys. Lett.* **B428** (1998) 342–345, `arXiv:hep-lat/9802011 [hep-lat]`.

[104] H. Neuberger, "More about exactly massless quarks on the lattice," *Phys. Lett.* **B427** (1998) 353–355, `arXiv:hep-lat/9801031 [hep-lat]`.

[105] H. Neuberger, "Vector - like gauge theories with almost massless fermions on the lattice," *Phys. Rev.* **D57** (1998) 5417–5433, `arXiv:hep-lat/9710089 [hep-lat]`.

[106] R. G. Edwards, B. Joo, A. D. Kennedy, K. Orginos, and U. Wenger, "Comparison of chiral fermion methods," *PoS* **LAT2005** (2006) 146, `arXiv:hep-lat/0510086 [hep-lat]`.

[107] R. Narayanan and H. Neuberger, "Infinitely many regulator fields for chiral fermions," *Phys. Lett.* **B302** (1993) 62–69, `arXiv:hep-lat/9212019 [hep-lat]`.

[108] S. Aoki and Y. Taniguchi, "One loop calculation in lattice QCD with domain wall quarks," *Phys. Rev.* **D59** (1999) 054510, `arXiv:hep-lat/9711004 [hep-lat]`.

[109] B. Efron, "Bootstrap Methods: Another Look at the Jackknife," *Ann. Statist.* **7** (1979) 1–26.

title=References]main